Spectral Element Method Simulation of Linear and Nonlinear Electromagnetic Field in Semiconductor Nanostructures

by

Ma Luo

Department of Electrical and Computer Engineering
Duke University

Date:_____

Approved:

_____
Qing Huo Liu, Supervisor

_____
William T. Joines

_____
Jungsang Kim

_____
Yaroslav A. Urzhumov

_____
Pei Zhong

Dissertation submitted in partial fulfillment of
the requirements for the degree of Doctor
of Philosophy in the Department of
Electrical and Computer Engineering in the Graduate School
of Duke University

2013

ABSTRACT

Spectral Element Method Simulation of Linear and Nonlinear Electromagnetic Field in Semiconductor Nanostructures

by

Ma Luo

Department of Electrical and Computer Engineering
Duke University

Date:_____

Approved:

_____
Qing Huo Liu, Supervisor

_____
William T. Joines

_____
Jungsang Kim

_____
Yaroslav A. Urzhumov

_____
Pei Zhong

An abstract of a dissertation submitted in partial
fulfillment of the requirements for the degree
of Doctor of Philosophy in the Department of
Electrical and Computer Engineering in the Graduate School of
Duke University
2013

Abstract

In this dissertation, the spectral element method is developed to simulate electromagnetic field in nano-structure consisting of dielectric, metal or semiconductor. The spectral element method is a special kind of high order finite element method, which has spectral accuracy. When the order of the basis function increases, the accuracy increases exponentially. The goal of this dissertation is to implement the spectral element method to calculate the electromagnetic properties of various semiconductor nano-structures, including photonic crystal, photonic crystal slab, finite size photonic crystal block, nano dielectric sphere. The linear electromagnetic characteristics, such as band structure and scattering properties, can be calculated by this method with high accuracy. In addition, I have explored the application of the spectral element method in nonlinear and quantum optics. The effort will focus on second harmonic generation and quantum dot nonlinear dynamics.

The electromagnetic field can be simulated in both frequency domain and time domain. Each method has different application for research and engineering. In this dissertation, the first half of the dissertation discusses the frequency domain solver, and the second half of the dissertation discusses the time domain solver.

For frequency domain simulation, the basic equation is the second order vector Helmholtz equation of the electric field. This method is implemented to calculate the

band structure of photonic crystals consisting of dielectric material as well as metallic materials. Because the photonic crystal is periodic, only one unit cell need to be simulated in the computational domain, and a periodic boundary condition is applied. The spectral accuracy is inspected. Adding the radiation boundary condition at top and bottom of the computational region, the scattering properties of photonic crystal slab can be calculated. For multiple layers photonic crystal slab, the block-Thomas algorithm is used to increase the efficiency of the calculation. When the simulated photonic crystals are finite size, unlike an infinitely periodic system, the periodic boundary condition does not apply. In order to increase the efficiency of the simulation, the domain decomposition method is implemented.

The second harmonic generation, which is a kind of nonlinear optical effect, is simulated by the spectral element method. The vector Helmholtz equations of multiple frequencies are solved in parallel and the consistence solution with nonlinear effect is obtained by iterative solver. The sensitivity of the second harmonic generation to the thickness of each layer can be calculated by taking the analytical differential of the equation to the thickness of each element.

The quantum dot dynamics in semiconductor are described by the Maxwell-Bloch equations. The frequency domain Maxwell-Bloch equations are deduced. The spectral element method is used to solve these equations to inspect the steady state quantum dot dynamic behaviors under the continuous wave electromagnetic excitation.

For time domain simulation, the first order curl equations in Maxwell equations are the basic equations. A spectral element method based on brick element is implemented to simulate a nano-structure consisting of woodpile photonic crystal. The resonance of a micro-cavity consisting of a point defect in the woodpile photonic crystal block is simulated. In addition, the time domain Maxwell-Bloch equations are implemented in the solver. The spontaneous emission process of quantum dot in the micro-cavity is inspected.

Another effort is to implement the Maxwell-Bloch equations in a previously implemented domain decomposition spectral element/finite element time domain solver. The solver can handle unstructured mesh, which can simulate complicated structure. The time dependent dynamics of a quantum dot in the middle of a nano-sphere are investigated by this implementation. The population inversion under continuous and pulse excitation is investigated.

In conclusion, the spectral element method is implemented for frequency domain and time domain solvers. High efficient and accurate solutions for multiple layers nano-structures are obtained. The solvers can be applied to design nano-structures, such as photonic crystal slab resonators, and nano-scale semiconductor lasers.

Dedication

To my parents.

Contents

List of Tables

List of Figures

Acknowledgements

I would like to say thank to my advisor, professor Liu, for the support.

Chapter One. Overview of Electromagnetic Simulation for Semiconductor Nano-Structure

Engineering researches and developments strongly rely on numerical simulation of the investigated system. The numerical simulation for electromagnetic field inspects the mechanic of physical phenomenon and gives a guideline for the system designs. Many semiconductor nano-structures and nano-devices involve electromagnetic field as well as matter wave of carriers[1-9]. A simulation helps the researchers to visualize the field distribution and evolution, and to optimize the figure of merit without repeating the expansive experiments. The simulation tools with high efficiency and accuracy for linear scattering of electromagnetic field in semiconductor nano-structure are implemented. Varying algorithms are developed to increase the efficiency of the simulation for periodic and (or) multiple layer structure.

In addition to the linear scattering of electromagnetic field, the semiconductor material exhibit nonlinear optical effects. The two nonlinear optical effects that are investigated in this thesis are second harmonic generation and exciton dynamic in quantum dot. Most of current simulation methods apply varying kinds of approximations to simplify the modeling of the electromagnetic wave, which have been providing powerful simulated tool for the researches. However, in nano-scale semiconductor structures and devices, an efficient and accurate simulation requires full wave modeling of the electromagnetic field. The sizes of many nano-structures and

nano-devices have the same length scale of the wavelength, so that many approximations fail to capture the physics of the system.

This dissertation develops the spectral element method numerical simulation tools that base on the full wave modeling of electromagnetic field. This simulation tool can simulate linear scattering of electromagnetic field, as well as some nonlinear optical effects. The modeling includes coupling of the electromagnetic field equations with one of the most important nonlinear optical effects, which is the second harmonic generation. In addition, the modeling also includes the quantum optical effect of carrier in semiconductor, which is the interaction between the exciton and electromagnetic field. This chapter reviews the modeling of the electromagnetic field and the popular used simulation tool, as well as the physics of the photonic crystals and semiconductor nano-structures. And then the current simulation tools for second harmonic generation and exciton dynamic in quantum dot are reviewed and discussed. The advantages of full wave simulation are briefly discussed. The rest of the dissertation introduces the implementation of the spectral element method for the simulation of electromagnetic field involving semiconductor nonlinear and quantum optical effect.

1.1 Maxwell's Equation and Wave Equation

The classical theory of electromagnetic field is described by the Maxwell's equations, which are

$$\nabla \times \mathbf{E} = -\mu_0 \mu_r \frac{\partial}{\partial t} \mathbf{H} \tag{1.1.1}$$

$$\nabla \times \mathbf{H} = \varepsilon_0 \varepsilon_r \frac{\partial}{\partial t} \mathbf{E} + \mathbf{J} \tag{1.1.2}$$

$$\nabla \cdot (\varepsilon_0 \varepsilon_r \mathbf{E}) = \rho \tag{1.1.3}$$

$$\nabla \cdot (\mu_0 \mu_r \mathbf{H}) = 0 \tag{1.1.4}$$

$\mathbf{E}$ is electric field, $\mathbf{H}$ is magnetic field, ε_0 and ε_r are permittivity in vacuum and relative permittivity, μ_0 and μ_r are permeability in vacuum and relative permeability, $\mathbf{J}$ is current density field, ρ is electrical charge density field. In most of the investigated systems, the pure electrical charge density is zero, so that both $\mathbf{E}$ and $\mathbf{H}$ are transverse field. The time domain simulation bases on the Maxwell's curl equations (1.1.1) and (1.1.2). By taking time derivation of equation (1.1.2), and inserting equation (1.1.1) into (1.1.2), the wave equation of the electric field is obtained as

$$-\nabla \times (\mu_0 \mu_r)^{-1} \nabla \times \mathbf{E} = \varepsilon_0 \varepsilon_r \frac{\partial^2}{\partial t^2} \mathbf{E} + \frac{\partial}{\partial t} \mathbf{J} \tag{1.1.5}$$

Assuming that the electric field as well as the current density field are harmonic field with a fix frequency, ω, the complex electric field can be written as $\mathbf{E}e^{j\omega t}$ and the complex current density field can be written as $\mathbf{J}e^{j\omega t}$. Inserting these expressions of the electric field and current density field into equation (1.1.5), we obtain the time harmonic wave equation as

$$-\nabla \times (\mu_0 \mu_r)^{-1} \nabla \times \mathbf{E} = -\varepsilon_0 \varepsilon_r \omega^2 \mathbf{E} + j\omega \mathbf{J} \tag{1.1.6}$$

This wave equation is also call vector Helmholtz equation of the electric field. The frequency domain simulation of the time harmonic field bases on the wave equation (1.1.6).

1.2 Widely Used Numerical Methods

One of the most popular simulation tools is finite difference time domain (FDTD) method[10], which discretizes the Maxwell's curl equation (1.1.1) and (1.1.2) by finite difference scheme. Central difference formula is used to approximate time and space derivatives. The electric field is sampled at integral time step, $(0, \Delta t, 2\Delta t, 3\Delta t, \cdots)$, and the magnetic field is sampled at half integral time step, $(\Delta t/2, \Delta t + \Delta t/2, 2\Delta t + \Delta t/2, 3\Delta t + \Delta t/2, \cdots)$. When equation (1.1.2) is solved, the time derivative of electric field is defined at integral time step and the magnetic field at the half integral time step is known, so that the only unknown is the electric field at the new time step, which can be explicitly solved. The same situation applies for solution of equation (1.1.1) for the magnetic field at the new time step. The spatial discretization of the electric and magnetic field is defined at the Yee grid. The sampling grid point of the electric field (magnetic field) at certain direction locates in the middle of the two sampling grid points of the magnetic field (electric field) at perpendicular directions, so that the spatial derivative can be explicitly calculated too. FDTD is efficient solver for electromagnetic field in simple system. When the system contain curve surface, a volume average is required, which reduce the efficiency and accuracy. The same

discretization scheme can be used for finite difference frequency domain (FDFD) method[11].

Another numerical simulation tool is plane wave expansion[12,13], which expand the solution by plane wave. This method was separately developed for calculation of band structure of periodic system and transmission rate of periodic photonic crystal slab[14]. The plane wave expansion for photonic crystal band structure was implemented in the software package MPB, which is a reliable tool. However, the efficiency of the solver is not high. The convergent behavior of the method is second order. The plane wave expansion for transmission rate of photonic crystal slab also suffers from low efficiency. The improvement of this method using coordinate transformation raise the efficiency, but this improvement is only applicable for rectangular structure.

One of the other most popular simulation tools is finite element method in time domain[15] and frequency domain[16-18]. Finite element method discretizes the system by a mesh that is conformal to the structure of the system. The mesh can bases on either hexahedral elements or tetrahedron elements. The simulated field is interpolated on the mesh by the basis functions, which are defined in each element. In order to ensure certain kind of continuity in the solution of the field, the basis functions in adjacent elements that share the same edge or face are bounded to be the same basis function in the whole system. For electromagnetic field, the tangential component of electric field and magnetic field is continue, so that the basis functions that share an edge or a face by

the tangential component are bounded. All of the basis functions form a Hilbert space, which is expected to well approximate the solution space of the electromagnetic field. An interpolation gives a point in this Hilbert space. After the interpolation, the Galerkin method is used to discretize the field. A weak form of the wave equations is obtained by testing the interpolation of the field by a set of test functions. If the test functions forms a Hilbert space that is the dual space of the basis functions' Hilbert space, the solution of the weak form gives the best approximation of the real solution. As a result, the choices of basis functions and test functions are important for finite element method. The mixed order vector basis functions were shown to efficiently model the electromagnetic field. The finite element method with this type of basis functions can suppress the spurious modes[18], which are the numerical fake modes.

Finite element method (FEM) for frequency domain simulation and finite element time domain (FETD) for time domain simulation have been developed and widely used in many applications. Although they are powerful tool to simulate complicated structure, the accuracy and efficiency of these methods still have room to be improved. The convergent behavior of the finite element method is second order as the size of the maximum element decrease. In order to obtain high accuracy simulation for engineering application, such as 0.1%, a high density mesh is needed.

1.3 Spectral Element Method and Spectral Element Time Domain

In order to improve the finite element method, spectral element method was introduced[20-25]. The spectral element method bases on the same principle as the finite element method, which is the Galerkin method. This method is similar to the pseudospectral frequency domain[25] and pseudospectral time domain[26] method, but with different choice of the vector basis functions. The spectral element method chooses different basis functions that highly improve the accuracy and efficiency. The key to improve the accuracy is to improve the interpolation of the electromagnetic field by the basis function. In finite element method, the field is interpolated by the low order polynomials, which only has second order accuracy. In spectral element method, higher order polynomials are used. Specifically, the Gauss-Lobatto-Legendre (GLL) polynomials are used to construct the basis functions. The interpolation error of the N order GLL polynomials exponentially decay as the order N increase, so that the accuracy of the interpolation is high. In addition, the overlap integrals in the spectral element method are calculated by the Gaussian integral method with GLL quadrature. An M order GLL quadrature gives exact integral of (2M-1) order polynomials, so that this method evaluates the integral with high accuracy. As a result, the spectral element method can obtain higher accuracy than the finite element method. The details of the spectral element method will be introduced in the next chapter.

1.4 Overview of Photonic Crystals

Photonic crystals are dielectric object with periodic structure[27]. For example, an alternating multilayer thin films with two materials with different permittivity and (or) permeability is a one-dimensional photonic crystal. This structure is called distributed Bragg reflector (DBR), which is shown in Figure 1 with N layers DBR in the background of vacuum. When the electromagnetic field is propagating at z direction, the electromagnetic field is partly reflected at each interface. The interfering between the multiple reflected fields changes the traveling property of the field. When the thickness of each layer equate to a quarter wavelength, the reflected waves are constructive interfering, and the reflectivity is maximum. When the thickness of each layer is $d_1 = \lambda\sqrt{\varepsilon_0\mu_0}/(4\sqrt{\varepsilon_1\mu_1})$ and $d_2 = \lambda\sqrt{\varepsilon_0\mu_0}/(4\sqrt{\varepsilon_2\mu_2})$, with λ being the wavelength in vacuum, the reflectivity is

$$R_N = \left[\frac{1-\left(\sqrt{\varepsilon_2\mu_2}/\sqrt{\varepsilon_1\mu_1}\right)^{2N}}{1+\left(\sqrt{\varepsilon_2\mu_2}/\sqrt{\varepsilon_1\mu_1}\right)^{2N}}\right]^2 \tag{1.4.1}$$

where N is the number of periods. When the number of periods increases, the reflectivity approaches one exponentially. When the incident wavelength deviates from the central wavelength, the reflectivity is still close to one, and decrease slowly. The reflective rate and transmission rate versus the incident wavelength for a typical DBR is plotted in Figure 2. The reflectivity remains close to 1 for a wide region around the

central wavelength 1550 nm. The width of this region is the bandwidth of the DBR, and this region in frequency domain is called the band gap.

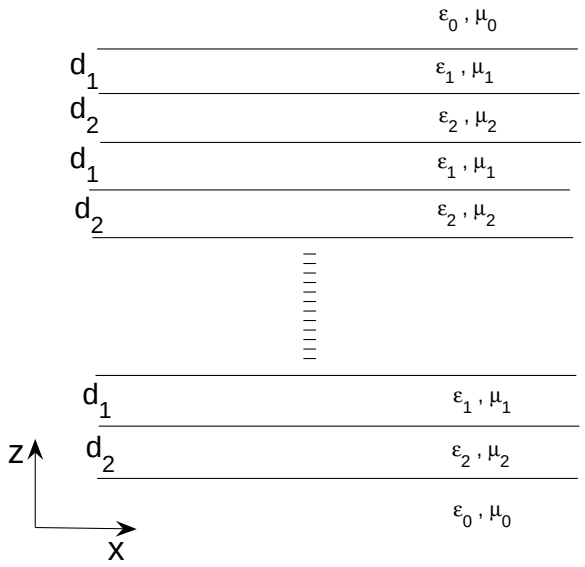

Figure 1. The structure of distributed Bragg reflector (DBR).

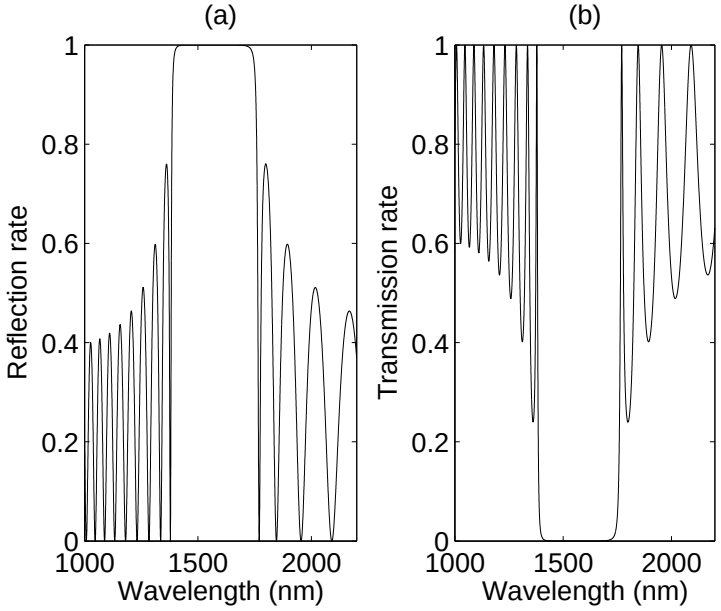

Figure 2. The Reflectivity versus the wavelength in the typical DBR. The parameters are $\varepsilon_1 = 3$, $\varepsilon_2 = 6$.

Similarly, two dimensional and three dimensional photonic crystals have multiple scattering of the electromagnetic field and result in a band gap[28,29]. Because the real system is always three dimensional, the effort of this project focuses on simulation of the three dimensional photonic crystals. For semiconductor devices, two kinds of photonic crystals are commonly used. The structures of these two kinds of photonic crystal are shown in Figure 3. Figure 3 (a) is two dimensional photonic crystal slabs[30], which is a dielectric slab with periodic structure, such as periodic holes or cylinders of different material. The photonic crystal slab is only periodic at the parallel directions (for example, the x and y directions), and has finite size at the vertical directions (such as z direction). A homogeneous dielectric slab support waveguide mode at the parallel direction, and provide confinement at the vertical direction by total internal reflection. The periodic holes scatter the electromagnetic field and modify the dispersion curve of the parallel waveguide mode. The band structure of the parallel traveling mode can be engineered by changing the structure and the periodicity of the periodic holes. The holes in Figure 3 (a) are in square lattice. This structure does not open up a big band gap, so that it is difficult to construct a waveguide or cavity with this photonic crystal slab. However, the resonant mode given by the band structure can have enhancement effect to nonlinear and quantum optics. Thus, the square lattice photonic crystal slab is vastly investigated in this thesis. In order to increase the resonant strength of the mode, a

multiple layer photonic crystal slab is designed and simulated. The structure is shown in Figure 4.

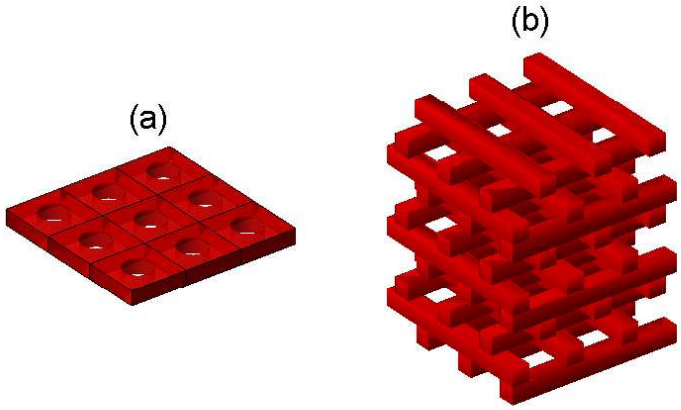

Figure 3. (a) The spatial structure of a photonic crystal slab with square lattice are holes. A 3×3 periods of the structure is shown. (b) The spatial structure of a woodpile photonic crystal. A $3\times3\times3$ periods of the structure is shown. In both figures, the red block is dielectric or semiconductor, and the background is air.

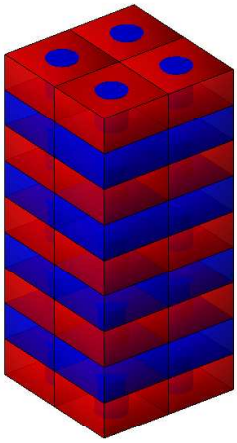

Figure 4. Spatial structure of a typical multiple layers photonic crystal slab. The red and blue volume is two different dielectric or semiconductor materials.

When the air holes of the photonic crystal slab are in triangular lattice, the band structures of the parallel mode are different, and a big band gap can be opened up.

Thus, a confined mode with frequency in the middle of the band gap can be constructed by introducing defect[31].

Another type of photonic crystal is periodic in all three directions. Figure 3 (b) is a woodpile photonic crystal that is periodic at all three directions[32,33]. The periodicity of this structure is face-central cubic, but it is more convenient to put this photonic crystal into a square lattice with larger unit cell. A $3\times3\times3$ periods of the square lattice is shown in Figure 3 (b). The band structure of this photonic crystal is shown in Figure 5. This photonic crystal has large complete band gap, so that it is an idea structure to confine and guide light. Because of the square lattice structure, it is also easy to construct optical interconnect system with multiple devices. A line defect, such as making one of the blocks wider, adding an extra block or subtracting a block, produces a waveguide mode. The cutoff frequency of the waveguide mode depends on the length of the period along the waveguide. By modulating the period of the waveguide, the cutoff frequency in the middle of the waveguide is lower than the cutoff frequency in the rest of the waveguide. An optical field with frequency between the two cutoff frequencies will be trapped in the middle of the waveguide. Thus, this period modulated point defect waveguide produces a micro-cavity[34,35].

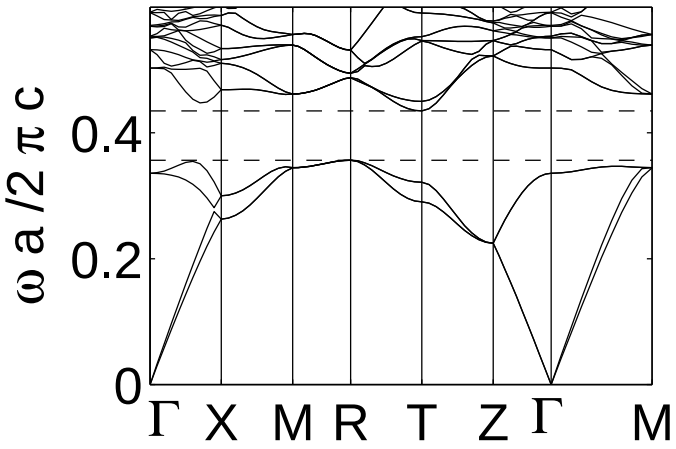

Figure 5. Band structure of the woodpile photonic crystal, with the height of the block being 200 nm, the width of the block being 180 nm and the parallel distance between two blocks in the same layer being 650 nm. The dielectric material has refractive index equal to 3.4.

1.5 Overview of Semiconductor Nano-Structure (Quantum Well, Quantum Dot)

There are many kinds of semiconductor nano-structures and devices. In this project, we only focus on two kinds of nano-scale semiconductor structure, quantum well and quantum dot[36], which are usually used as the gain medium of the nano-scale semiconductor lasers. Quantum well and quantum dot are both built on the substrate of a semiconductor. The purpose of building quantum well and quantum dot is to spatially confine carriers (electron and hole) in a small region of the semiconductor.

Figure 6 shows a band structure of a typical bulk semiconductor. For a cold semiconductor that has no electric current, all electrons are in the valence bands, and all valence bands are fully filled; all conductive bands are empty. In order to reduce confusion, the electron, which is the natural element with one negative unit of charge, is

called charge particle in the rest of this article. When a current is injected into the semiconductor, some charge particles are injected into the conductive band and some other charge particles in the valence bands are pulled out of the semiconductor bulk. The charge particles in the conductive band are called electron; the empty spot in the valence band is call hole, which is equivalent to a charge particle with one positive unit of charge. Electron and hole are called carriers because they carry charge. Another way to excite carriers is to input an incident photon. If the energy of the incident photon is larger than the band gap of the semiconductor, the charge particle from the valence band absorbs the energy and transit to the higher energy level in the conductive band. Thus, a pair of electron and hole is simultaneously generated.

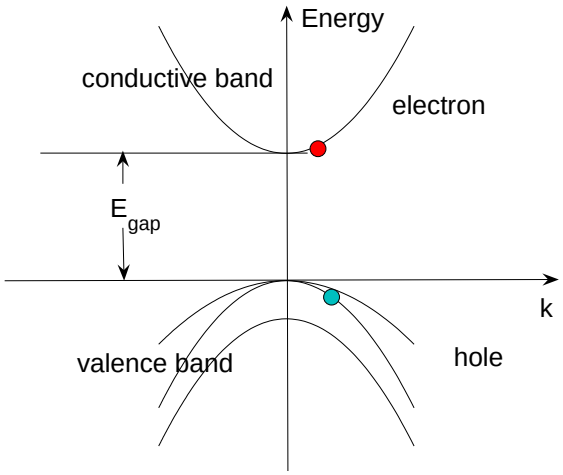

Figure 6. Band structure of the charge particle of a typical semiconductor.

Quantum well is a thin film of semiconductor, called the well, clad by another semiconductor, called the barriers. The structure of a quantum well is shown in Figure 7.

The semiconductor in the well has smaller band gap and the semiconductor in the barriers has larger band gap. If the energy of the electron is smaller than the band edge of the conductive band edge in the barrier, the electron cannot propagate in the barrier area; but the electron can propagate in the well area. When the electron travels to the interface between the well and the barrier, it will be reflected and travel backward into the well. The propagation of the electron is described by the Schrodinger equation, which is a wave equation. Thus, the electron is a propagating wave in nano-scale. Because of the interfering between the reflected waves from the two interfaces, the electron in the well has discrete energy eigen level, which is shown as blue line in Figure 7. These discrete energy levels are the confined mode of quantum well. Similarly, the hole has discrete energy levels, which are also the confined mode of quantum well. Because in x and y directions (parallel directions) the quantum well is homogeneous, the electron and hole can freely propagate in x and y directions. Thus, each confined mode is expanded into confined band of two dimensional free particles. The ground state of a quantum well is that all charge particles are in the valence band, so that there is no electron or hole. The first excited state has one electron in the first discrete electron energy level and one hole in the first discrete hole energy level. The energy of the first excited state is the energy difference between the electron and hole. Because of the Coulomb interaction between the electron and hole, they are bound to become an exciton, which has smaller energy level than the energy difference between the electron

and hole. Thus, the exciton is the real first excited state of the quantum well. An incident photon with frequency resonant to the energy level of the exciton can excite the quantum well from the ground state to the first excited state, and then generate an exciton. There are two different reverse processes. The quantum transition from the first excited state to the ground state emits a photon with the same energy as the exciton. This emission could be spontaneous emission or stimulated emission, which is used as varying type of light source in the semiconductor devices. Another reverse process is the recombination of the electron and hole, which loss the energy to the damping phonon. In this process, the energy is transform into heat, which will raise the temperature of the semiconductor devices. This effect is undesired for the application of quantum well, because the heat might burn down the system. Varying methods have been investigated to reduce the probability of recombination, thus reduce the loss of energy to heat. One method is to spatially separate electron and hole in a double wells system.

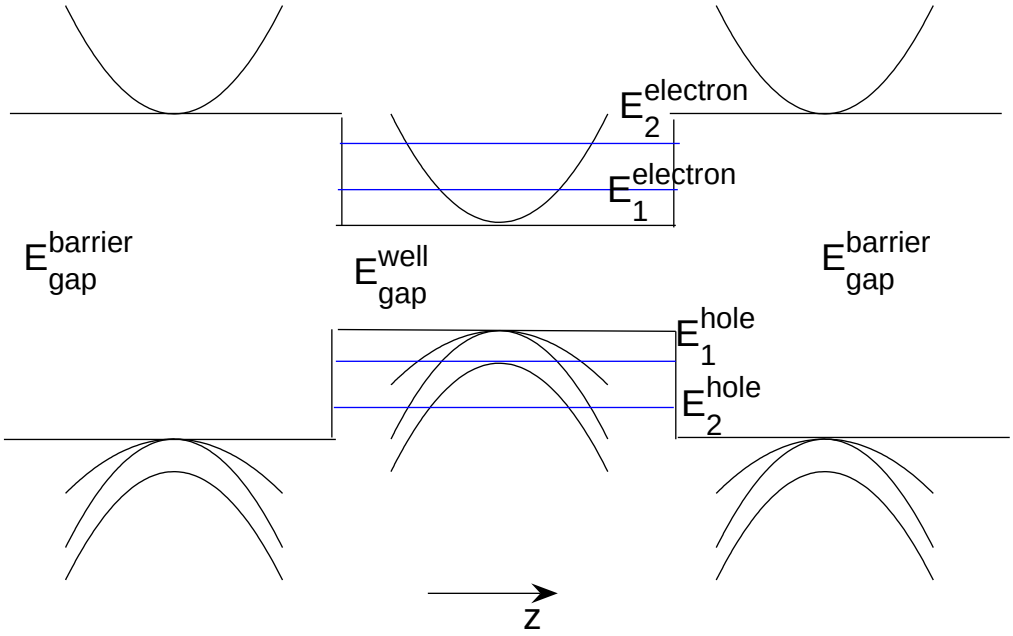

Figure 7. Exhibition of the structure of a quantum well.

Quantum dot has the same principle as quantum well, except that quantum dot is finite size in all three dimensional. The well region could be a cube, and the surrounding region is the barrier that is semiconductor with larger band gap. The confinement of electron and hole in quantum dot is in all three dimensions. As a result, the energy level of quantum dot is completely discrete. As comparison, the electron and hole in the quantum well have discrete energy level in the vertical direction, but continue energy level in the parallel direction. Comparing to quantum well, the electron and hole in the quantum dot are more confined, so that the quantum effect of the quantum dot is usually stronger.

The shape of the quantum dot depends on the lattice structure of the semiconductor and the synthesis method. The shape of the quantum dot consisting of

GaAs is pyramid (or truncated pyramid)[37]. Because the size of the quantum dot is much smaller than the wavelength of the optical field, the detail of the shape of the quantum dot hardly influence the interaction between the quantum dot and the optical field. Thus, the quantum dot is usually approximated as a point dipole source. Another approximation for uniform distribution of many quantum dots in one volume is a volume current source. The energy level of the ground state and excited state of the quantum dot also depend on the shape of the quantum dot. In this research, the shape of the quantum dot is assumed to be a cube as an approximation. In a cube quantum dot, there are three degenerate excited states with the same energy level. The transition from the ground state to these three excited state has polarization at x, y and z direction. As a result, the quantum dot is modeled as three dipole source at the three directions. In the research of this thesis, the amplitudes of these three dipole sources are modeled by the corresponding Bloch equations.

1.6 Modeling for Second Harmonic Generation

Second harmonic generation is one of the most important nonlinear optical effects[38]. Many theoretical model and numerical investigation have been used to analyze the second harmonic generation from optical material. The typical approximation in the theoretical model is the mode expansion method. The optical mode is firstly calculated from the linear Maxwell equation. The overall electromagnetic field is a superposition of all modes with corresponding coefficients, which are spatial

and time dependent. The expansion of the total field is inserted into the vector Helmholtz equation, and the second order differential equations of the expansion coefficients are obtained. Because the nonlinear optical effect is week, the amplitude of each mode is assumed to be small, so that the slow varying approximation is used. This approximation neglects the second order differential of the expansion coefficients. Thus, the first order differential equations of the expansion coefficients are obtained. The analytical and numerical solutions of the second harmonic generation field are based on these first order differential equations. The optical mode for bulk optical material is plane wave, and the optical mode for waveguide is the guided mode.

The slow varying approximation is a good approximation for large scale nonlinear optical device. However, for nano-structure of semiconductor, the varying of the amplitude is large. In addition, the nonlinear effect could change the spatial structure of the optical mode itself. As a result, a full wave simulation is developed in this thesis. The simulation based on the vector Helmholtz equation of the electric field. The electric field is directly modeled by the spectral element method. The second order nonlinear optical effect is modeled by the nonlinear polarization field, which is determined by the electric field and the second order susceptibility. The whole modeling is based on the classical optical theory of nonlinear optics. The only approximation in the simulation is the numerical descritization of the electric field by the spectral element method. In this method, the optical mode and the amplitude of the mode are all

included in the numerical descritization of the electric field. The simulation tool can naturally capture the effect that the optical mode is distorted by the nonlinear effect. The detail of the simulation method is given the Chapter three. The research will be applicable for high frequency light source, and highly monochromatic light source.

1.7 Modeling for Quantum Dot Dynamic

In this project, we mainly consider the nonlinear effect of the quantum dot[39,40], which exhibit strong exciton excitation phenomenon, and serve as gain medium in laser. A quantum dot can be simplified as a two-level system[41]. The exciton in the quantum dot can be either in the ground state and the first excited state. The difference of the eigenvalue of the energy between these two levels defines the resonant frequency of the quantum dot. The exciton can has probability of being at the ground state and the excited state. The time evolution of the probability of each level is determined by the Bloch equations. The Bloch equations include two sets of equations. The first set of equations describes the time evolution of the population of each energy level, which is the probability of the exciton being at the corresponding energy level. The difference between the population in the excited state and the ground state is called the population inversion. The second set of equations describes the time evolution of the transition between the two energy levels. When the quantum dot is in the electromagnetic environment, the interaction between the exciton and electromagnetic field modified the time evolution of the exciton. When the exciton transit from excited state to ground

state, it will radiate electromagnetic field, and vice versa. As a result, the Maxwell equation for electromagnetic field is modified too. The coupling between the electromagnetic field and the exciton is described by the Maxwell-Bloch equations

In the widely used method[41], the linear Maxwell equation without the coupling to the exciton is solved to obtain the optical modes of the system. These optical modes include the cavity modes, waveguide modes and radiation modes. After these modes are obtain, the total electromagnetic field is described as an expansion by the superposition of these modes. Inserting the expansion into the Maxwell equation and making the slow varying approximation, the first order differential equations to describe the time evolution of the expansion coefficients are obtain. Thus, the Maxwell-Bloch equations are a set of ordinary differential equation including the Bloch equation and the time evolution equation for the expansion coefficients.

In this thesis, the investigation of the quantum dot-electromagnetic field interaction based on the Maxwell-Bloch equations[42-45] of the electromagnetic field and the polarization field of the quantum dot. The Maxwell equation is directly solved by the spectral element method. The only approximation is the spatial descritization. The slow varying approximation is not used. In this way, the coupling between all types of optical modes is naturally included into the simulation. In addition, this method can naturally model the change of the shape of the confined optical modes, when the coupling between the exciton and the electromagnetic field is strong. In this thesis, the dynamic of

the population inversion of the quantum dot will be investigated by frequency domain and time domain solver. The frequency domain solver intend to reveal the steady state dynamic of the population inversion under continue excitation of the external electromagnetic field. The time domain solver has two intensions. One is to simulation the spontaneous emission of the quantum dot, where there is no external electromagnetic field. The other is to analyze the dynamic of the population inversion under pulse excitation, and engineer the correct pulse width to obtain positive population inversion. This research will be useful for design of pulse laser.

Chapter Two. Frequency Domain Spectral Element Method for Linear Optics

The harmonic electromagnetic field can be simulated by frequency domain solver, which assume the solution have the form $\mathbf{E}(\mathbf{r})e^{j\omega t}$. The applications of the frequency domain solver split into two types. The first type application calculates the resonant frequency of the system by calculating the eigenvalue system. This type includes close and open cavity problem, and band structure of periodic system. The effort of this article firstly focuses on solving the band structure of photonic crystal. The band structure is critical property for optical system design. Two main characters of the band structure are particular interesting. The band gap creates a frequency range that the optical field cannot propagate through the photonic crystal. This effect is the foundation of constructing high quality nano-scale waveguide and micro-cavity at optical frequency. The other character is the group velocity from the slope of the band structure. By engineering the periodic structure, the dispersive surface can be engineered. Photonic crystals with slow light and (or) negative group velocity have been investigated. The design of band structure is important to harness the light in nano-scale.

The second type application calculates the scattering field of the incident field from outside of the system, or the radiation field from the current source inside of the system. The effort of this article solves both kinds of scattering, with plane wave

incidence and dipole source radiation. For a thin film under plane wave incidence, the transmission rate, reflection rate and absorption rate reveal the resonant property of the thin film, such as plasmonic excitation.

2.1 Wave Equation and Spectral Element Method

In order to simulate the harmonic electromagnetic field, the wave equation (1.1.6) is discretized by the SEM[21]. The discretization process is shown in Figure 8. The simulated system is split by the mesh into many curve hexahedral elements, which are conformal to the shape of any object in the system. Each element is mapped to the reference element, which is a cube defined as $(\xi,\eta,\zeta)\in[-1,1]$. The mixed order vector basis functions are defined in the reference domain as

$$\tilde{\mathbf{\Phi}}_{rst}^{\xi}=\hat{\xi}\phi_r^{(N-1)}(\xi)\phi_s^{(N)}(\eta)\phi_t^{(N)}(\zeta) \tag{2.1.1}$$

$$\tilde{\mathbf{\Phi}}_{rst}^{\eta}=\hat{\eta}\phi_r^{(N)}(\xi)\phi_s^{(N-1)}(\eta)\phi_t^{(N)}(\zeta) \tag{2.1.2}$$

$$\tilde{\mathbf{\Phi}}_{rst}^{\zeta}=\hat{\zeta}\phi_r^{(N)}(\xi)\phi_s^{(N)}(\eta)\phi_t^{(N-1)}(\zeta) \tag{2.1.3}$$

where $\phi_j^{(N)}(\xi)$ is the N-th order GLL polynomial. The GLL polynomial is defined as

$$\phi_j^{(N)}(\xi)=\frac{-1}{N(N+1)L_N(\xi_j^{(N)})}\frac{(1-\xi^2)L_N^{'}(\xi)}{(\xi-\xi_j^{(N)})} \tag{2.1.4}$$

where $L_N(\xi)$ is the N-th order Legendre polynomial, $L_N^{'}(\xi)$ is the derivative of the Legendre polynomial and $\xi_j^{(N)}$ is the j-th zero point of the polynomial $(1-\xi^2)L_N^{'}(\xi)$. The nodal point of the $\hat{\xi}$ component basis functions is $(\xi_r^{(N-1)},\xi_s^{(N)},\xi_t^{(N)})$, where the

basis function (2.1.1) equates to one at the corresponding nodal point and zero at the other nodal points. The nodal points of the basis functions of the other two components are similarly defined. After defining the basis functions in the reference domain, they are mapped into the real space elements. The mapping of the coordinate between the reference domain and the real space is $x(\xi,\eta,\zeta)$, $y(\xi,\eta,\zeta)$, and $z(\xi,\eta,\zeta)$. The Jacobian matrix of the mapping is defined as

$$\mathbf{J} = \begin{bmatrix} \frac{\partial x}{\partial \xi} & \frac{\partial y}{\partial \xi} & \frac{\partial z}{\partial \xi} \\ \frac{\partial x}{\partial \eta} & \frac{\partial y}{\partial \eta} & \frac{\partial z}{\partial \eta} \\ \frac{\partial x}{\partial \zeta} & \frac{\partial y}{\partial \zeta} & \frac{\partial z}{\partial \zeta} \end{bmatrix} \tag{2.1.5}$$

In order to keep the tangential component of the electric field continue, the vector basis functions in the real space are given by the covariant mapping from the basis functions in the reference domain.

$$\mathbf{\Phi}^{u}_{rst}(x,y,z) = \mathbf{J}^{-1}\tilde{\mathbf{\Phi}}^{u}_{rst}(\xi,\eta,\zeta) \tag{2.1.6}$$

$$\nabla \times \mathbf{\Phi}^{u}_{rst}(x,y,z) = \frac{1}{\det(\mathbf{J})}\mathbf{J}^{T}\tilde{\nabla} \times \tilde{\mathbf{\Phi}}^{u}_{rst}(\xi,\eta,\zeta) \tag{2.1.7}$$

In equation (2.1.6) and (2.1.7), $u \in (\hat{\xi},\hat{\eta},\hat{\zeta})$ stands for the three unit components of the field. In real space, the three components are not necessary orthogonal to each other, but they are a complete set of direction in three-dimensional space. The nodal points in the reference domain are mapped into real space too. Note that these nodal points are all vector nodal points with the definition of their directions. Each basis function in the

whole mesh is given a global index. The basis functions from adjacent elements that shape the same nodal point at the interface have the same global index. Thus, the electric field can be interpolated by giving the complex field coefficient at each nodal point,

$$\mathbf{E} = \sum_{n} E_n \mathbf{\Phi}_n \tag{2.1.8}$$

where the summation go through all of the nodal points, and n is the combined index of the element index $n^{(e)}$ and (u, r, s, t).

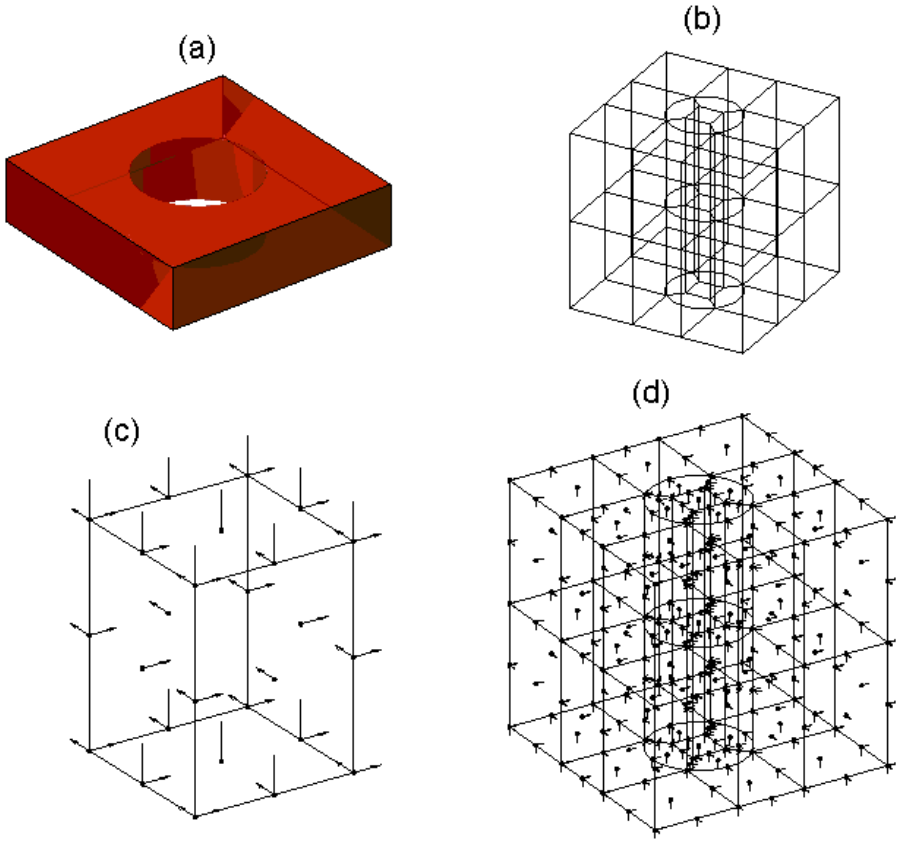

Figure 8 Discretization process of the SEM. (a) is the simulated object, (b) is the mesh with hexahedral elements, (c) is the vector basis functions in the reference, and (d) is the basis functions in the real space mesh.

The weak form of the wave equation can be obtained by using the Galerkin method. Inserting equation (2.1.8) into the wave equation (1.1.6), and then testing the wave equation by one of the basis function, we have

$$\int_{\Omega} dV[(\nabla\times\mathbf{\Phi}_m)\cdot\mu_r^{-1}\cdot(\nabla\times\mathbf{E})-k_0^2\mathbf{\Phi}_m\cdot\varepsilon_r\cdot\mathbf{E}]-jk_0\oint_{\partial\Omega}dS[\mathbf{\Phi}_m\cdot(\hat{n}\times\overline{\mathbf{H}})]=0 \tag{2.1.9}$$

where Ω is the volume of the simulated system, $\partial\Omega$ is the surface of the volume, $\hat{n}$ is the normal unit vector at the surface, and $\overline{\mathbf{H}}=Z_0\mathbf{H}$ is the normalized magnetic field with Z_0 being the impendence in vacuum. $\mathbf{\Phi}_m$ is the m-th testing function, which is the same kind of function as the basis function $\mathbf{\Phi}_n$. The boundary condition determine the surface integral terms. For the calculation of the band structure of a periodic system, this term equates to zero because the integral from the opposite face cancel each other. As a result, the weak form can be written in matrix form as

$$\mathbf{SE}=k_0^2\mathbf{ME} \tag{2.1.10}$$

where $\mathbf{S}$ is the stiffness matrix, $\mathbf{M}$ is the mass matrix, and $\mathbf{E}$ is the column vector of the electric field unknowns. The matrix element of the stiffness matrix and mass matrix are

$$S_{m,n}=\int_{\Omega} dV[(\nabla\times\mathbf{\Phi}_m)\cdot\mu_r^{-1}\cdot(\nabla\times\mathbf{\Phi}_n)] \tag{2.1.11}$$

$$M_{m,n}=\int_{\Omega} dV\mathbf{\Phi}_m\cdot\varepsilon_r\cdot\mathbf{\Phi}_n \tag{2.1.12}$$

The band structure can be obtained by solving the general eigenvalue equation (2.1.10)[46-49]. Some numerical results of the method are given in the follow two subsections.

2.1.1 Two-Dimensional Photonic Crystal

For two-dimensional photonic crystal, the structure and the electromagnetic field are invariant to the $\hat{z}$ axis. Thus, the wave equation and the weak form can be simplified. The structure and mesh of a two-dimensional photonic crystal are shown in Figure 9. The band structure of the TM mode and TE mode are shown in Figure 10[46]. The TM mode has a band gap. The convergence behavior of the relative error is plotted in Figure 11 as the relative error versus the number of unknowns or the order of the SEM. The relative error is defined as

$$error_N = \frac{\left| k_0^{(13)} - k_0^{(N)} \right|}{k_0^{(13)}} \tag{2.1.13}$$

where N is the order of the SEM, $k_0^{(13)}$ is the eigenvalue given by the 13th order SEM, which is the highest order used in the calculated, and $k_0^{(N)}$ is the eigenvalue given by the N order SEM. The straight line in Figure 11 (b) shows that the SEM has exponential convergence behavior. Specifically, the fourth order SEM has relative error less than 0.1%. In this case, the minimum points-per-wavelength (PPW), which is at the thick line in Figure 9, is equal to 4. Thus, the SEM obtains high accuracy result with points-per-wavelength as small as 4 for two-dimensional photonic crystal.

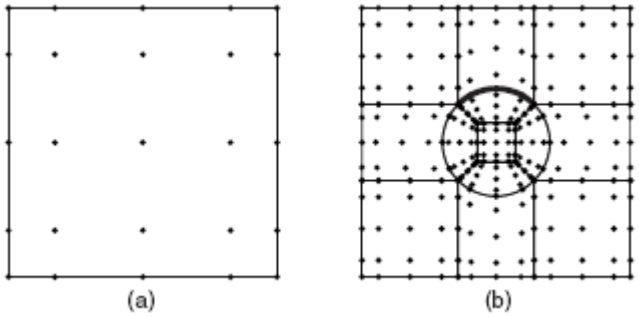

Figure 9. (a) The two-dimensional reference domain element with nodal points. (b) The unit cell of a square lattice two-dimensional photonic crystal with mesh and nodal points. The material inside the cylinder is alumina with permittivity equal to 8.9, and the radius of the cylinder is 0.2a with 'a' being the lattice constant. The background medium is air.

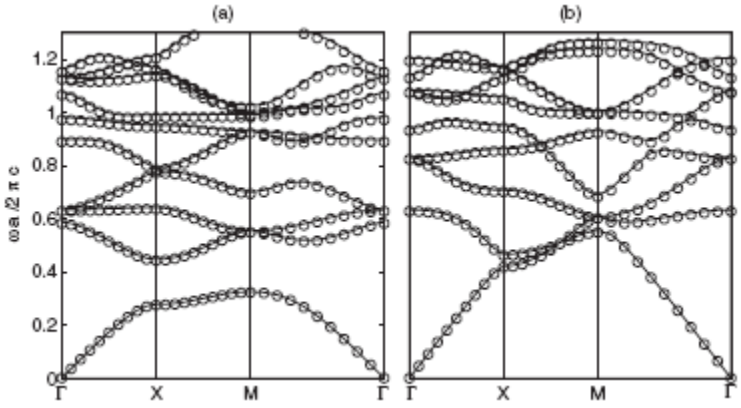

Figure 10. The band structure of the (a) TM mode and (b) TE mode of the two-dimensional photonic crystal shown in Figure 9.

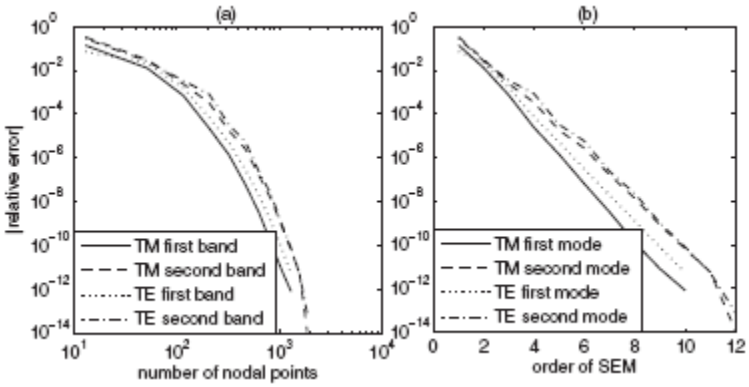

Figure 11. The relative error versus, (a) the number of nodal points, and (b) order of the SEM, for the eigenvalue at the X point of the first Brillouin zone of the first and second band in Figure 10.

2.1.2 Three-Dimensional Photonic Crystal

For three-dimensional photonic crystal, the convergence behavior of the SEM is also inspected and compared with the plane wave expansion method[48]. An infinite stack of two dimensional photonic crystal slabs shown in Figure 8(a) form a three dimensional photonic crystal, whose band structure is plotted in Figure 12. The band structure of the same photonic crystal is plotted in the same figure, which is calculated by plane wave expansion in software MPB. The results from the two methods match with each other, which validate the SEM result. The convergence behavior of the SEM is shown in Figure 12 (b). The straight line of the average relative error of the lowest 20 bands shows that the SEM has exponential convergence.

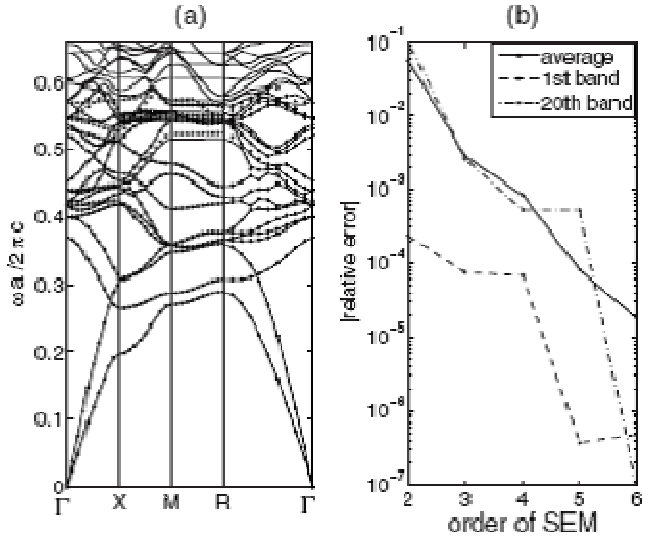

Figure 12. (a) The band structure of a three dimensional photonic crystal. The dielectric structure in a unit cell is shown in Figure 8 (a). The solid lines are given by the SEM, and the dot lines are given by the plane wave expansion. The radius of the air hole is 0.3a, the thickness of the slab is 0.5a, with 'a' being the lattice constant of the square lattice. The permittivity of the dielectric medium is 12, and the background medium is air. (b) The relative error versus the order of the SEM of the first band, the 20th band, and the average value of the lowest 20 bands, at the M point of the first Brillouin zone.

The next numerical example is a more complicated structure shown in Figure 13. The band structure of this photonic crystal is shown in Figure 14. Although there is not a band gap, the two lowest bands are completely separated from the rest of the higher bands. A complete band gap can be open up by increasing the permittivity of the dielectric medium. The average relative error of the lowest 20 band is plotted in Figure 15 (a), together with the relative error of the plane wave expansion method in Figure 15 (b). The figures show that the convergence behavior of the SEM is better than the plane wave expansion method. The fourth order SEM has relative error being less that 0.1%,

while the plane wave expansion method needs 72 grid resolution (72 points along each direction in the three-dimensional grid) to obtain the same accuracy. The CPU time and number of unknowns for calculating the whole band structure with this accuracy are listed in the Table 2.1. The SEM is almost 18 times faster than the plane wave expansion method, with 17 times less unknowns.

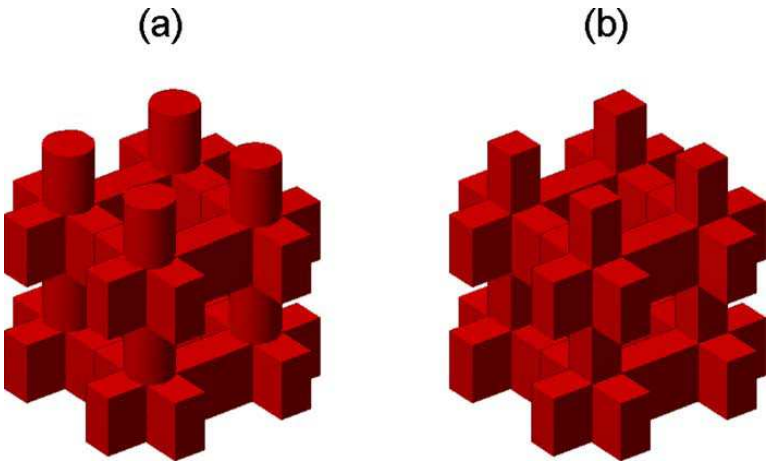

Figure 13. The dielectric structure of the $2\times2\times2$ unit cells of a photonic crystal. The permittivity of the dielectric medium is 12, and the background medium is air.

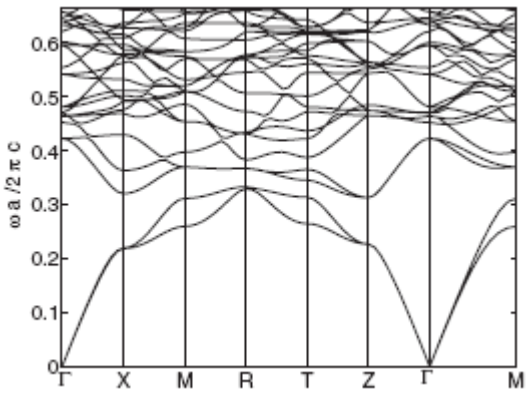

Figure 14. The band structure of the photonic crystal in Figure 13.

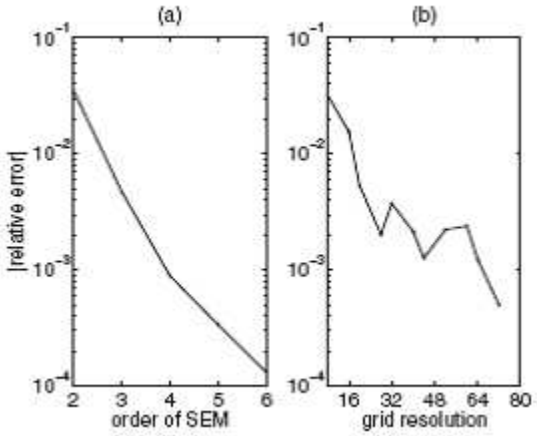

Figure 15. (a) The relative error versus the order of the SEM. (b) The relative error versus the grid resolution in the implementation of the plane wave expansion method by the software MPB.

Table 1. CPU time for calculating the band structure of the photonic crystal in Figure 13 with 20 bands and 70 sampling point in the first Brillouin zone, and the number of unknowns for the fourth order SEM and the plane wave expansion method with 72 grid points.

	CPU time (s)	Number of unknowns
SEM	4684	4992
Plane wave expansion method	373248	84000

In conclusion, the SEM calculates the band structure with high accuracy and high efficiency. In most of the simulated photonic crystal, a points-per-wavelength smaller than 5 is enough to obtain high accuracy with relative error being less than 0.1%.

2.1.3 Three-Dimensional Photonic Crystal Consisting of Dispersive Material

When the material in the photonic crystal is dispersive, the relative permittivity is a function of the frequency, which is proportional to the eigenvalue, $\omega = k_0 c$. As a

result, the eigenvalue problem to determine the band structure is nonlinear. If the dispersive material can be model by Drude model and (or) Lorentz model, the permittivity is a rational-polynomial function of the eigenvalue. In this case, a linear transformation can be used to transfer the nonlinear eigenvalue problem into a linear eigenvalue problem with auxiliary variables. We have calculated the band structure of a semi-woodpile photonic crystal, whose spatial structure is shown in Figure 16. The block is gold, which is described by Drude-Lorentz model, and the background is air. This size of the unit cell is 400 nm. The band structure is shown in Figure 17. A high cutoff frequency is found in this photonic crystal. The first two bands is found to be completely separated from the higher bands.

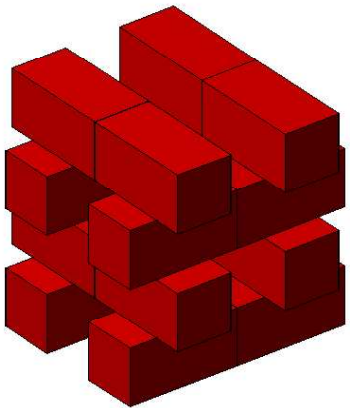

Figure 16. Spatial structure of 2×2 unit cells of a semi-woodpile photonic crystal.

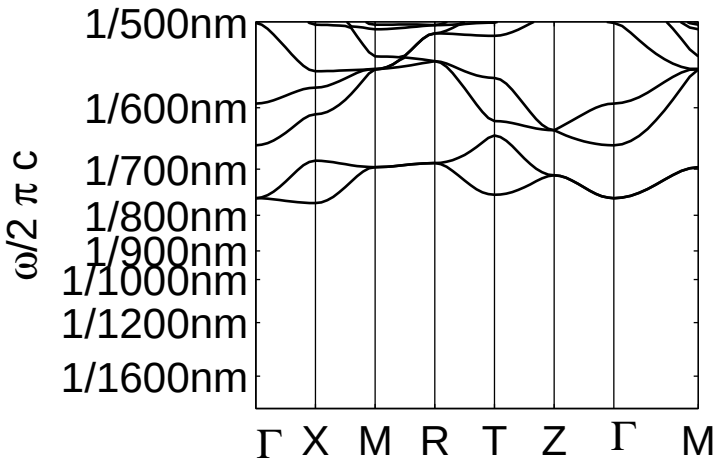

Figure 17. Band structure of the semi-woodpile photonic crystal with gold as the block material, and air as background material. The size of the unit cell is 400.

2.2 Method of Moments Radiation Boundary Condition

When the simulated system is finite size at $\hat{z}$ direction and infinite periodic at $\hat{x}$ and $\hat{y}$ directions, the periodic boundary condition is only applicable to the vertical surfaces that are parallel to the $\hat{z}$ axis. On the top and bottom horizontal surfaces that are perpendicular to the $\hat{z}$ axis, the radiation boundary condition is needed. The method of moments (MOM) exactly describes the field propagation through the background medium. Thus, the MOM is used for the radiation boundary condition[50]. The MOM gives two integral equations about the electric and magnetic fields on the surface of a system. The electric field integral equation (EFIE) is given as[51,52]

$$\hat{n}\times[\frac{1}{2}\mathbf{E}+\mu_{r(0)}L(\bar{\mathbf{J}}_s)-\tilde{K}(\mathbf{M}_s)]=n\times\mathbf{E}^{Inc} \tag{2.2.1}$$

and the magnetic field integral equation (MFIE) is given as

$$\hat{n}\times[\frac{1}{2}\overline{\mathbf{H}}+\varepsilon_{r(0)}L(\mathbf{M}_s)+\tilde{K}(\overline{\mathbf{J}}_s)]=n\times\overline{\mathbf{H}}^{Inc} \tag{2.2.2}$$

where $\varepsilon_{r(0)}$ and $\mu_{r(0)}$ are the permittivity and permeability of the background medium, $\mathbf{M}_s=-\hat{n}\times\mathbf{E}$ is the equivalent surface magnetic current, $\overline{\mathbf{J}}_s=\hat{n}\times\overline{\mathbf{H}}$ is the equivalent surface electric current, and $\mathbf{E}^{Inc}$ and $\overline{\mathbf{H}}^{Inc}$ are the incident field from the background. The integral operators L and M are defined as

$$L(\mathbf{X})=jk_0\oint_{\partial\Omega}[\mathbf{X}(\mathbf{r}')G_0(\mathbf{r},\mathbf{r}')+\frac{1}{k^2}\nabla'\cdot\mathbf{X}(\mathbf{r}')\nabla G_0(\mathbf{r},\mathbf{r}')]dS' \tag{2.2.3}$$

$$K(\mathbf{X})=\oint_{\partial\Omega}\mathbf{X}(\mathbf{r}')\times\nabla G_0(\mathbf{r},\mathbf{r}')dS' \tag{2.2.4}$$

where $k=k_0\sqrt{\varepsilon_{r(0)}\mu_{r(0)}}$ is the wave number in the background medium. The green's function in the background medium is defined as

$$G_0(\mathbf{r},\mathbf{r}')=\frac{e^{-jk|\mathbf{r}-\mathbf{r}'|}}{4\pi|\mathbf{r}-\mathbf{r}'|} \tag{2.2.5}$$

The integral of equation (2.2.4) has a singularity that can be extracted as $\hat{n}\times K(\mathbf{X})=\hat{n}\times\tilde{K}(\mathbf{X})-(1/2)\mathbf{X}$, with $\tilde{K}(\mathbf{X})$ being the main value of the integral.

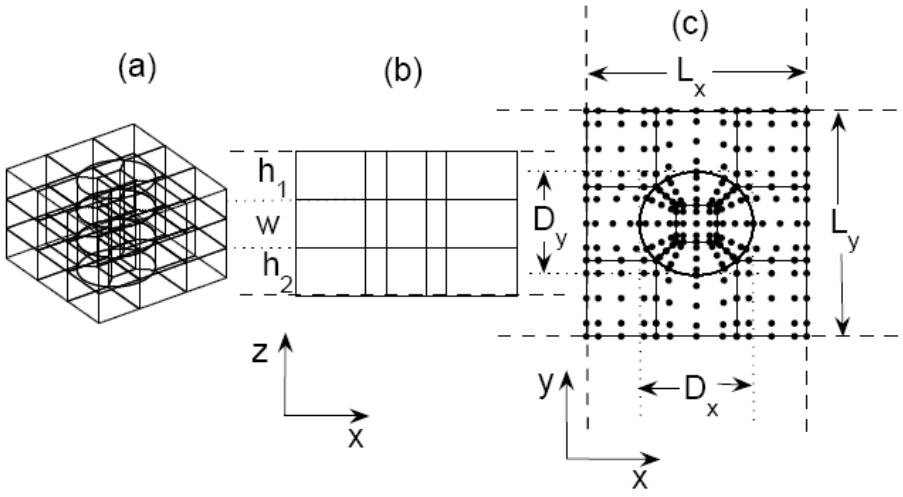

Figure 18. The configuration and mesh of the infinite periodic thin film. (a) is the three dimensional view. (b) is the side view. (c) is the top view. The thickness at $\hat{z}$ direction is finite, and the numbers of periods at $\hat{x}$ and $\hat{y}$ are infinite with periods L_x and L_y.

For the scattering problem of infinite periodic thin film, the configuration of the simulated structure is defined in Figure 18. The incident plane wave comes from the top or bottom background with oblique angle to the $\hat{z}$ axis θ. The system is periodic at $\hat{x}$ and $\hat{y}$ directions, so that only one unit cell is used for the simulation domain and the periodic boundary conditions at the vertical surfaces are used. The radiation boundary condition is used for the top and bottom horizontal surfaces to simulate the incident and outgoing wave. In this case, there are two background mediums, including the top and bottom mediums. Each background is homogeneous with relative permittivity $\varepsilon_{r(p)}$ and permeability $\mu_{r(p)}$, where $p=1$ stands for the top medium and $p=2$ stands for the

bottom medium. The top and bottom surfaces of the simulated system are described by the corresponding integral equations and the green's function. Thus, the EFIE is

$$\hat{n}\times[\frac{1}{2}\mathbf{E}+\mu_{r(p)}L_p(\bar{\mathbf{J}}_s)-\tilde{K}_p(\mathbf{M}_s)]=n\times\mathbf{E}_p^{Inc} \tag{2.2.6}$$

and the magnetic field integral equation (MFIE) is given as

$$\hat{n}\times[\frac{1}{2}\overline{\mathbf{H}}+\varepsilon_{r(p)}L_p(\mathbf{M}_s)+\tilde{K}_p(\bar{\mathbf{J}}_s)]=n\times\overline{\mathbf{H}}_p^{Inc} \tag{2.2.7}$$

The integral operators are

$$L_p(\mathbf{X})=jk_0\oint_{\partial\Omega_p}[\mathbf{X}(\mathbf{r}')G_p(\mathbf{r},\mathbf{r}')+\frac{1}{k_p{}^2}\nabla'\cdot\mathbf{X}(\mathbf{r}')\nabla G_p(\mathbf{r},\mathbf{r}')]dS' \tag{2.2.8}$$

$$K_p(\mathbf{X})=\oint_{\partial\Omega_p}\mathbf{X}(\mathbf{r}')\times\nabla G_p(\mathbf{r},\mathbf{r}')dS' \tag{2.2.9}$$

where $k_p=k_0\sqrt{\varepsilon_{r(p)}\mu_{r(p)}}$ is the wave number in the top and bottom background medium. Because the system is periodic at $\hat{x}$ and $\hat{y}$ direction, the periodic green's function is defined as

$$G_p(\mathbf{r},\mathbf{r}')=\sum_{\mathbf{K}}\frac{e^{-jk_p|\mathbf{r}-\mathbf{r}'-\mathbf{K}|}}{4\pi|\mathbf{r}-\mathbf{r}'-\mathbf{K}|} \tag{2.2.10}$$

where $\mathbf{K}$ is the real space lattice vector of the periodic structure.

Note that on the top and bottom surfaces, the z coordinate is constant, so that the main value of the integral (2.2.9) is zero. In the integral (2.2.8), the integration cover the singular point of the green's function when $|\mathbf{r}-\mathbf{r}'-\mathbf{K}|=0$. In order to improve the efficiency and accuracy of the integral (2.2.8), the real space periodic green's function

(2.2.10) is transformed into wave number domain green's function. At first, the integral form of the green's function in homogeneous medium is given as

$$G_0(\mathbf{r},\mathbf{r}') = \int d\mathbf{q} \frac{e^{-j\mathbf{q}\cdot(\mathbf{r}-\mathbf{r}')}}{(2\pi)^3(|\mathbf{q}|^2 - k_p^2)} \tag{2.2.11}$$

where $\mathbf{q}$ is the wave number space variant. The periodic green's function is equivalent to the green's function with a periodic source, $-\sum_m \sum_n e^{-jk_x mL_x} e^{-jk_y nL_y} \delta(\mathbf{r}-\mathbf{r}'-mL_x\hat{x}-nL_y\hat{y})$, with $k_x = k_p\cos(\theta)$ and $k_y = k_p\sin(\theta)$ being the wave number of the incident plane wave at $\hat{x}$ and $\hat{y}$ direction. Thus, the integral form of the periodic green's function in the top and bottom background is given as

$$\begin{aligned} G_p(\mathbf{r},\mathbf{r}') &= \sum_m \sum_n e^{-jk_x mL_x} e^{-jk_y nL_y} \int d\mathbf{q} \frac{e^{-j\mathbf{q}\cdot(\mathbf{r}-\mathbf{r}'-mL_x\hat{x}-nL_y\hat{y})}}{(2\pi)^3(|\mathbf{q}|^2 - k_p^2)} \\ &= \int \left[d\mathbf{q} \sum_m \sum_n e^{-jk_x mL_x + jq_x mL_x} e^{-jk_y nL_y + jq_y nL_y} \frac{e^{-j\mathbf{q}\cdot(\mathbf{r}-\mathbf{r}')}}{(2\pi)^3(|\mathbf{q}|^2 - k_p^2)} \right] \end{aligned} \tag{2.2.12}$$

Making use of the Dirac comb function formula, $\sum_m \sum_n e^{-j(k_x-q_x)mL_x} e^{-j(k_y-q_y)nL_y} = \frac{2\pi}{L_x}\frac{2\pi}{L_y}\sum_m \sum_n \delta(k_x - q_x - 2\pi m/L_x)\delta(k_y - q_y - 2\pi m/L_y)$, and taking the integral of q_x and q_y, the equation (2.2.12) is transformed into

$$G_p(\mathbf{r},\mathbf{r}') = \sum_{m=-\infty}^{+\infty} \sum_{n=-\infty}^{+\infty} e^{-jq_x^m(x-x')} e^{0\, jq_y^n(y-y')} I_{m,n}(k_x, k_y, k_p) \tag{2.2.13}$$

where $q_x^m = k_x - 2\pi m/L_x$, $q_y^n = k_y - 2\pi m/L_y$; and

$$I_{m,n}(k_x,k_y,k_p)=\int dq_z \left.\frac{e^{-jq_z(z-z')}}{(2\pi)^3[(q_x^m)^2+(q_y^n)^2+(q_z)^2-k_p^2]}\right|_{z=z'}=\frac{2\pi}{L_x}\frac{2\pi}{L_y}\frac{1}{4\pi j\sqrt{k_p^2-(q_x^m)^2-(q_y^n)^2}} \tag{2.2.14}$$

The $G_p(\mathbf{r},\mathbf{r}')$ in equation (2.2.13) is the wave number domain green's function. Inserting equation (2.2.13) into equation (2.2.8), the integral functions are smooth without singular point, so that the integrals can be calculated efficiently and accurately.

There are two ways to combine the SEM weak form (2.1.9) and the MOM integral equations. One way is to produce a matrix equation directly from (2.1.9), and produce another matrix equation by testing the combine field integral equation (CFIE). The CFIE is a summation of the EFIE and MFIE, as

$$\hat{n}\times[\frac{1}{2}\mathbf{E}+\mu_{r(p)}L_p(\bar{\mathbf{J}}_s)-\tilde{K}_p(\mathbf{M}_s)]+\hat{n}\times[\frac{1}{2}\overline{\mathbf{H}}+\varepsilon_{r(p)}L_p(\mathbf{M}_s)+\tilde{K}_p(\bar{\mathbf{J}}_s)]=n\times\mathbf{E}_p^{Inc}+n\times\overline{\mathbf{H}}_p^{Inc} \tag{2.2.15}$$

This scheme gives a matrix equation that is non symmetric. In order to improve the efficiency of the simulation, we use another scheme that gives a symmetric matrix. This scheme processes as following. Inserting the MFIE (2.2.7) into the weak form of the wave equation (2.1.9), we obtain a weak form with the radiation boundary condition as

$$\begin{aligned}&\int_\Omega dV[(\nabla\times\mathbf{\Phi}_m)\cdot\mu_r^{-1}\cdot(\nabla\times\mathbf{E})-k_0^2\mathbf{\Phi}_m\cdot\varepsilon_r\cdot\mathbf{E}]\\&-jk_0\oint_{\partial\Omega}dS(\hat{n}\times\mathbf{\Phi}_m)\cdot[-\frac{1}{2}\overline{\mathbf{H}}+\varepsilon_{r(p)}L_p(\mathbf{M}_s)+\tilde{K}_p(\bar{\mathbf{J}}_s)]=jk_0\oint_{\partial\Omega}dS(\hat{n}\times\mathbf{\Phi}_m)\cdot\overline{\mathbf{H}}_p^{Inc}\end{aligned} \tag{2.2.16}$$

In addition, by testing the EFIE (2.2.6), another weak form is obtained as

$$-jk_0\oint_{\partial\Omega} dS(\hat{n}\times\boldsymbol{\Phi}_m)\cdot[\frac{1}{2}\mathbf{E}+\mu_{r(p)}L_p(\bar{\mathbf{J}}_s)-\tilde{K}_p(\mathbf{M}_s)]=jk_0\oint_{\partial\Omega} dS(\hat{n}\times\boldsymbol{\Phi}_m)\cdot\mathbf{E}_p^{Inc} \qquad (2.2.17)$$

The two weak forms (2.2.16) and (2.2.17) give a matrix equation with the unknowns being the electric field in the volume and the magnetic field on the top and bottom surface. The matrix equation can be solved by direct solver or iterative solver. The system matrix is symmetric, so that the direct solver or the iterative solver is easier to converge. The scattered field can be calculated from the solution vector.

The Poynting vector is defined as $\mathbf{P}=(1/2)\mathrm{Re}[\mathbf{E}\times\mathbf{H}^*]$. Given the Poynting vector of the incident field $\mathbf{P}_0$, the reflection rate is given as

$$R=\frac{\oint_{\partial\Omega} dS\mathbf{P}(z|_{top})\cdot\hat{z}}{\oint_{\partial\Omega} dS\mathbf{P}_0\cdot(-\hat{z})} \qquad (2.2.18)$$

and the transmission rate is given as

$$T=\frac{\oint_{\partial\Omega} dS\mathbf{P}_0\cdot(-\hat{z})-\oint_{\partial\Omega} dS\mathbf{P}(z|_{bottom})\cdot(-\hat{z})}{\oint_{\partial\Omega} dS\mathbf{P}_0\cdot(-\hat{z})} \qquad (2.2.19)$$

The absorption rate is given as

$$A=1-T-R \qquad (2.2.20)$$

Because the Poynting vector of the incident plane wave is constant, it can be integral on either top or bottom surface.

The combination of the equation (2.2.16) and (2.2.17) can calculate the local eigenstate of a photonic crystal slab as well. An eigenstate is a non-trivial solution when

k_0 is equal to the eigenvalue and the incident field is zero. From equation (2.2.16) and (2.2.17), k_0 appear in front of the mass matrix $\mathbf{\Phi}_m \cdot \varepsilon_r \cdot \mathbf{E}$, MFIE and EFIE, as well as inside of the MFIE, EFIE and the Green's function. Because the Green's function is a nonlinear, non-polynomial function of k_0, the matrix equation gives a nonlinear eigenvalue problem. If the material in the photonic crystal slab is dispersive, then ε_r is a nonlinear function of k_0 too. Thus, the nonlinear eigenvalue problem cannot be transform into a linear eigenvalue problem. This nonlinear eigenvalue problem can be solved by self consistence search of k_0 around the possible range of the solution. When the equation (2.2.16) and (2.2.17) are used to solve the scattering problem the wave number k_0 is a real number. However, when these two equation are used to solved the eigenstate, the eigenvalue k_0 is in general a complex number $k_0 = (\omega_0^{'} + j\omega_0^{''})/c$, with the real part being the oscillation frequency, and the imaginary part being the decay rate. We can argue that for eigenvalue solver, the k_0 in front of the mass matrix is a complex number, and the k_0 at the other place in equation (2.2.16) and (2.2.17) are real part of the eigenvalue.

At first, the resonant mode has Lorentzian distribution of energy in frequency domain, $W(\omega) = (\omega_0^{''})^2 / [(\omega - \omega_0^{'})^2 + (\omega_0^{''})^2]$, with center frequency $\omega_0^{'}$ and line width $\omega_0^{''}$. Thus, the eigenvalue problem becomes a series of eigenvalue problems, with frequency scaling through the whole frequency domain. In each of these eigenvalue

problems, the parameter $k_0 = \omega / c$ is a real number at any place of the equation (2.2.16) and (2.2.17). Because the line width is much smaller than the center frequency, we only need to solve the eigenvalue problem at the center frequency. As an approximation, the k_0 in front of the mass matrix is the complex eigenvalue with real part equal to the center frequency, and imaginary part equal to the line width, so as to model the Lorentzian distribution of energy in frequency domain. The loss is due to the material absorption loss and mirror loss. The material absorption loss is modeled by the imaginary part of the permittivity, and the MOM models the mirror loss. In order to include the loss effect from all frequency, the permittivity and the integral equations need to have a convolution with the Lorentzian distribution function. Because the loss is small, the Lorentzian distribution function can be approximated as a delta function in these convolution, so that the k_0 in the permittivity and the integral equations are real numbers. As a result, only the k_0 in front of the mass matrix is a complex number.

We can reorganize the equation (2.2.16) and (2.2.17) as

$$\begin{bmatrix} \mathbf{S}_{II} & \mathbf{S}_{IS} \\ \mathbf{S}_{SI} & \mathbf{S}_{SS} + U^M(\mathrm{Re}[k_0]) - V^M(\mathrm{Re}[k_0])[U^E(\mathrm{Re}[k_0])]^{-1} V^E(\mathrm{Re}[k_0]) \end{bmatrix} \begin{bmatrix} \mathbf{E}_I \\ \mathbf{E}_S \end{bmatrix} = k_0^2 \begin{bmatrix} \mathbf{M}_{II} & \mathbf{M}_{IS} \\ \mathbf{M}_{SI} & \mathbf{M}_{SS} \end{bmatrix} \begin{bmatrix} \mathbf{E}_I \\ \mathbf{E}_S \end{bmatrix} \tag{2.2.21}$$

where the subscript I refer to the basis functions inside the simulated volume, and the subscript S refer to the basis functions on the top and bottom surfaces. $\mathbf{S}$ and $\mathbf{M}$ are the stiffness and mass matrixes with matrix elements

$$S_{m,n} = \int_{\Omega} dV(\nabla \times \mathbf{\Phi}_m) \cdot \mu_r^{-1} \cdot (\nabla \times \mathbf{\Phi}_n) \tag{2.2.22}$$

$$M_{m,n} = \int_{\Omega} dV \mathbf{\Phi}_m \cdot \varepsilon_r \cdot \mathbf{\Phi}_n \tag{2.2.23}$$

The matrixes U and V are from the integral equations, defined as

$$U_{m,n}^{M} = -j \,\mathrm{Re}[k_0] \oint_{\partial\Omega} dS(\hat{n} \times \mathbf{\Phi}_m) \cdot L(-\hat{n} \times \mathbf{\Phi}_n) \tag{2.2.24}$$

$$V_{m,n}^{M} = -j \,\mathrm{Re}[k_0] \oint_{\partial\Omega} dS(\hat{n} \times \mathbf{\Phi}_m) \cdot [-\frac{1}{2}\mathbf{\Phi}_n + \tilde{K}(\hat{n} \times \mathbf{\Phi}_n)] \tag{2.2.25}$$

$$U_{m,n}^{E} = -j \,\mathrm{Re}[k_0] \oint_{\partial\Omega} dS(\hat{n} \times \mathbf{\Phi}_m) \cdot L(\hat{n} \times \mathbf{\Phi}_n) \tag{2.2.26}$$

$$V_{m,n}^{E} = -j \,\mathrm{Re}[k_0] \oint_{\partial\Omega} dS(\hat{n} \times \mathbf{\Phi}_m) \cdot [\frac{1}{2}\mathbf{\Phi}_n + \tilde{K}(\hat{n} \times \mathbf{\Phi}_n)] \tag{2.2.27}$$

where $\hat{n}$ is the normal unit vector of the surface. The eigenvalue problem (2.2.21) is solved by the self consistence solver. We can define a function $W(k_{00}) = k_{00} - \mathrm{Re}[k_0]$, where k_{00} is a real number. At each evaluation of the function $W(k_{00})$, the k_{00} is inserted into the left hand side of equation (2.2.21), and the eigenvalue matrix equation is solved to obtain the complex eigenvalue k_0. The real part of k_0 is put into the function $W(k_{00})$. When $W(k_{00})$ equal to zero, the corresponding k_0 is the eigenvalue. Thus, the eigenvalue problem (2.2.21) can be solved by searching the zero point of the function $W(k_{00})$. Because the system matrix at the left hand side of the equation (2.2.21) is a sparse matrix, an iterative solver can use k_{00} as initial gauss to calculate only one

eigenvalue that is the closest to the input number k_{00}, instead of calculating all of the eigenvalues.

2.2.1 Finite Thickness Infinite Periodic slits

The same formula can be simplified to calculate two-dimensional system, which is uniform in $\hat{y}$ direction. This system is the finite thickness infinite periodic slits shown in Figure 19[53]. The thickness of the gold slit is d, the period of the strip is L_x, and the filling factor is $f = s/L_x$. The refractive indexes of the top and bottom background medium are $n_1 = 1.723$ and $n_2 = 1.333$. The permittivity of gold is dispersive, which is given by reference [54].

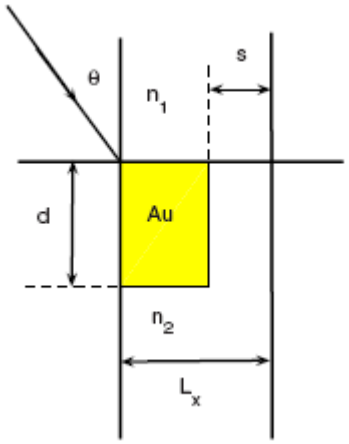

Figure 19. The dielectric structure of the finite thickness infinite periodic slits. The slit is periodic in x direction with period L_x, and is homogeneous in y direction. The thickness in z direction is finite. The refractive indexes in the top and bottom background medium are n_1 and n_2. The thin film is made of gold.

The transmission and absorption rate of a specific system are plotted in Figure 20. From the transmission rate, a resonance is observed at the wavelength near 1000 nm.

The high absorption under the wavelength 600 nm is due to the high material absorption of the metal. At wavelength near 700 nm and incident angle larger than the critical angle of total reflection, a small band of high absorption is observed. This absorption is due to the excitation of the surface plasmon polariton mode, which is highly attenuated.

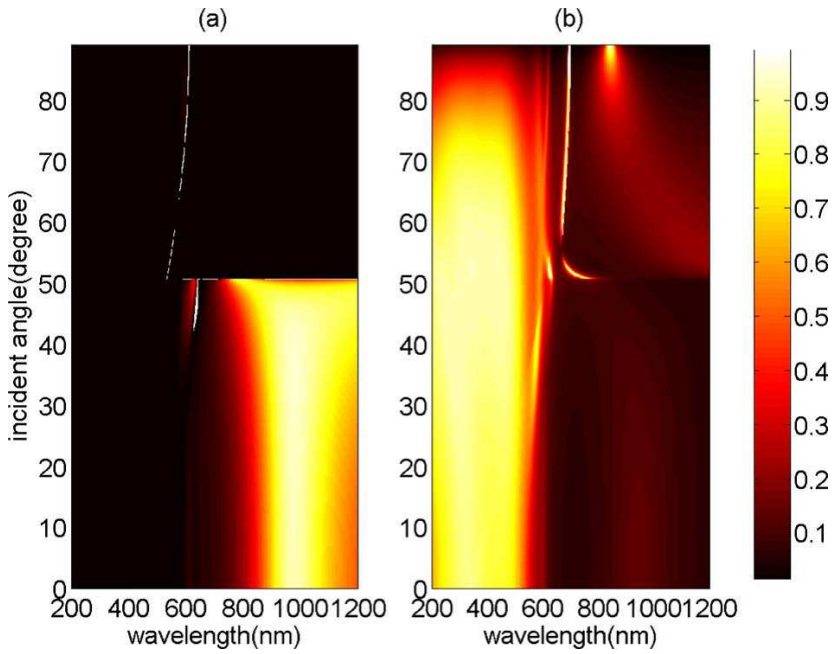

Figure 20. (a) Transmission rate and (b) absorption rate of a gold slits with $L_x = 200$ nm, $d = 200$ nm, and filling factor $f = 0.2$.

2.2.2 Finite Thickness Infinite Periodic Photonic Crystal Slab

The SEM is used to calculate the transmission rate of the finite thickness periodic structure in three dimensional space. The periodicity is two dimensional along x and y direction, and the thickness at z direction is finite. We first apply the method to simulate a thin silver film with square air holes and compare the result with reference[55] to

inspect the accuracy and efficiency of the SEM. The arrangement of the air holes is in a square lattice. The structure and the mesh of the system are plotted in Figure 21. The permittivity of the slab is $(0.1-8.94j)^2$; the background medium above the slab and in the hole is air; the background medium beneath the slab is glass with permittivity 1.512^2. The parameters for the structure are: h=200 nm, $a_x = a_y = 900$ nm, $w_x = w_y = 250$ nm. The transmission rate under normal incidence versus the number of unknown in the simulation is plotted in Figure 22 (a). The reference result is plotted in the same figure as dash line. With number of unknown being twenty thousand, the SEM result is close to the reference result. The relative error versus the order of SEM is plotted in Figure 22 (b). The straight line in the log scale plotting shows that the convergent behavior is exponential. For the fifth order SEM, the minimum points-per-wavelength (PPW) throughout the system are 6.2. Thus, the SEM can obtain accuracy as high as 0.1% with points-per-wavelength as small as 6.2 for dispersive surface plasmon system.

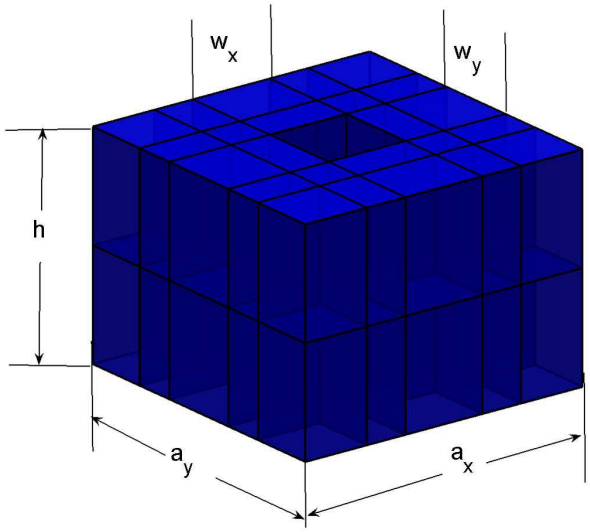

Figure 21. The dielectric structure and the mesh of the metallic slab with periodic square air holes. The air holes are in square lattice with period a_x and a_y at x and y directions. The widths of the square air holes are w_x and w_y. The thickness of the film is h.

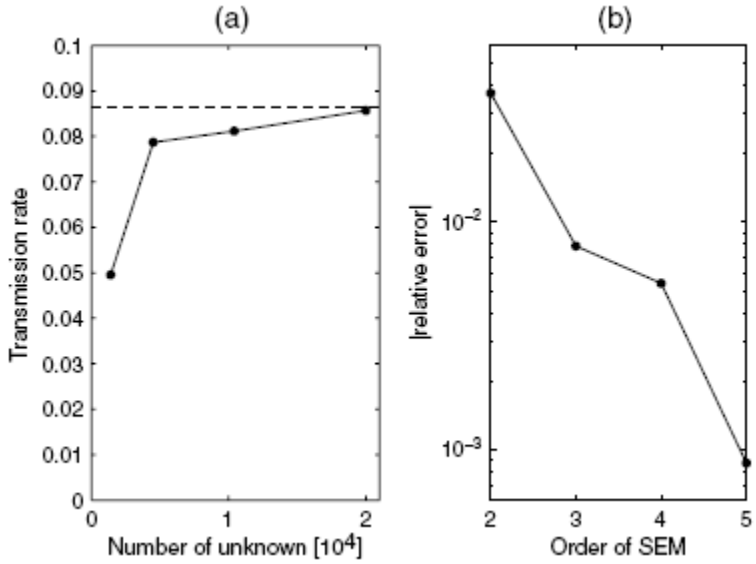

Figure 22. (a) The transmission rate versus number of the unknown in the SEM simulation. The dash line is the reference result. (b) The relative error of the SEM results versus the order of SEM.

The second numerical example is a metallic thin film with periodic air holes on the substrate of glass, as shown in Figure 23 (a)[50]. The air holes are in rectangular lattice with periods $L_x = 460$ nm and $L_y = 470$ nm. The diameters of the elliptical air holes are $D_x = 238$ nm and $D_y = 216$ nm. The thickness of the thin film is 35 nm. The thin film consists of silver with dispersive permittivity given by reference [54]. The permittivity of the glass is 1.512^2. The transmission rate versus the wavelength of the incidence wave is plotted in Figure 24. The incident angle ranges from 0 to 80 degrees with 10 degrees interval. For each rising of the incident angle, the transmission rate is shifted upward for 1, so that the figure can clearly shows the evolution of the position of the peaks under different incident angle. Three resonant bands, marks as I, II and III are identified. Band I and II are dispersive, whose wavelength changes as the incident angle increase. Band III is non-dispersive with a fix wavelength. In order to further identify the physical origination of these three bands, the field pattern of electric field magnitude in the middle plane of the thin film is plotted in Figure 25. The field patterns show that there are three type of mode being excited, which is surface plasmon polariton (SPP), local surface plasmon (LSP) and local resonance of the air hole. The mode (a) includes all three modes. When the incident angle increases, the mode (b) only include surface plasmon polariton, because the field pattern shows a plane wave like pattern. Thus, the band I is mainly due to the excitation of the surface plasmon polariton. The mode (c) has field pattern spread out inside of the air hole, so that the band II is due to the excitation

of the local resonance of the air hole. The mode (d) has field pattern concentrate at the edge of the air hole, which is the feature of the local surface plasmon mode. Thus, the band III is due to the excitation of the local surface plasmon mode. The local surface plasmon is the most localized mode. The local surface plasmon at one hole has little interaction with the local surface plasmon at the adjacent hole, so that the mode is small dispersive or non-dispersive. The surface plasmon polariton has plane wave mode at parallel direction, so that it is highly dispersive. The local resonance at the air hole has electric field leaking to the adjacent holes, so that the interaction between the modes at adjacent holes is large. Thus, the local resonance at the air hole is dispersive mode.

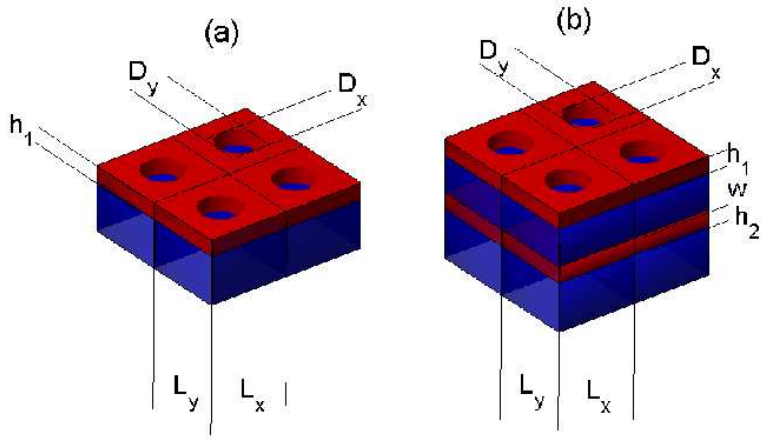

Figure 23. (a) The spatial structure of a single thin film system with periodic air hole on the substrate of glass. (b) The spatial structure of a double thin films system. The thin film on the top has periodic air hole. The dielectric between the two thin film is SiO_2 , and the substrate is glass.

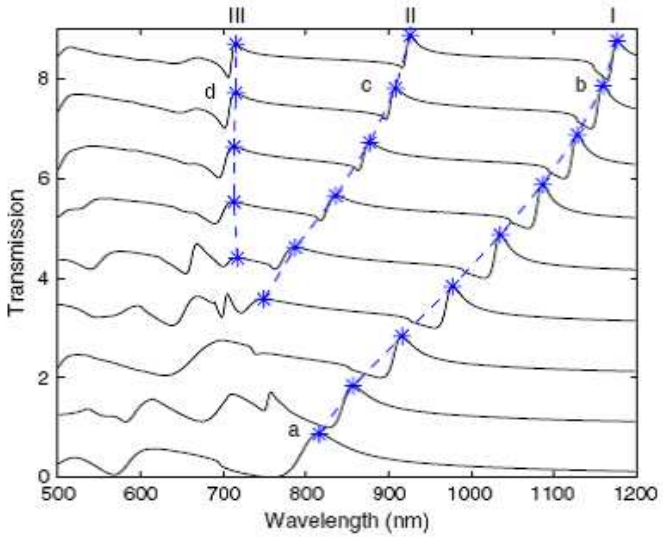

Figure 24. The transmission rate of the system in Figure 23 (a). From bottom to top, the incident angles are from 0 to 80 degrees with 10 degrees interval, and each transmission rate is shifted upward for 1 in the plotting. The peaks of the transmission rate are marked with star and connected. Three resonant bands are observed. Four transmission peaks marks as 'a' to 'd' will be further investigated.

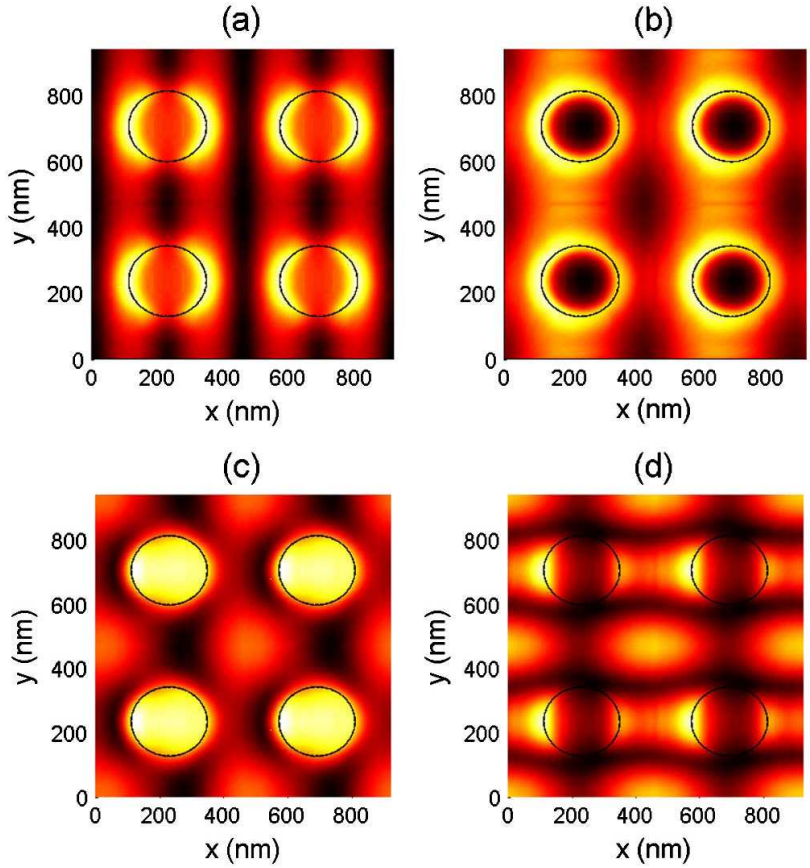

Figure 25. The field patterns of the electric field magnitude at the middle plane of the thin film in Figure 23 (a). The incident wavelength and angle is for each field pattern are given in the corresponding peaks marked by 'a' to 'd' in Figure 24.

The third numerical example is the double metallic thin film system shown in Figure 23 (b). Both two thin films consist of silver. The top thin film has thickness $h_1 = 35$ nm, with rectangular lattice air holes. The periods of the air holes are $L_x = 460$ nm and $L_y = 470$ nm. The diameters of the elliptical air holes are $D_x = 238$ nm and $D_y = 216$ nm. The bottom thin film is homogeneous with thickness $h_2 = 33$ nm. The dielectric material between the two thin films is SiO_2 with permittivity being 1.454^2 and thickness being 195 nm. The substrate is glass, and the background medium above

is air. The simulated transmission rate under normal incidence to this system is plotted in Figure 26 (a), together with the experimental result from reference [56]. The resonant peaks of the numerical result given by the SEM are close to that given by the experimental result. At wavelength 559 nm, the numerical result shows a peak of transmission rate. The experimental result at the same wavelength only has small signal that is hardly identified as a peak. Thus, the relative error at this wavelength versus the order of SEM is plotted in Figure 26 (b). It is shown that the numerical result convergent at this wavelength. We argue that the difference comes from the experimental error. When the half wavelength is close to the diameter of the air hole, the incident wave excited the local resonance of the air hole. The shape of the air hole in experiment is not perfectly elliptical shape, so that the resonant modes at different air holes have different frequencies. The resonant modes at different air holes do not form a strong global resonant mode in the experiment, so that the signal is weak. As a summary, when wavelength larger than 600 nm, the numerical result given by the SEM matches well with the experimental result.

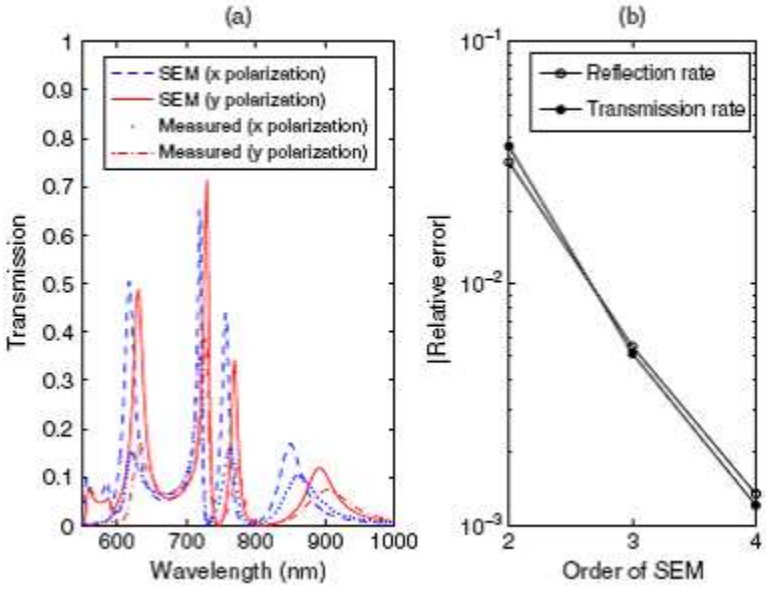

Figure 26. (a) The transmission rate versus the incident wavelength for the system in Figure 23 (b). The incident field is normal incidence. (b) The relative error of the SEM results versus the order of SEM at wavelength 559 nm.

In conclusion, the SEM efficiently solves the transmission problem through thin film with periodic structure. When metallic material presents in the system, the skin depth is small, which raise challenge to the numerical simulation. However, the SEM gives accurate result with relative error smaller than 0.1%, even when the points-per-wavelength is as small as 6.2. The SEM is applied to thin film system with periodic air holes, and the field pattern is used to identify the excited mode.

2.3 Block-Thomas Algorithm for Multiple Layer System

The simulated systems in Figure 23 have only one or a few layers, so that the total number of unknown is not large. When the simulated systems have more layers, the total number of unknown is large. It will be too difficult to solve the linear equation

given by Eq. (2.2.16) and (2.2.17). However, we can exploit the property of the multiple layer structure to develop more efficient algorithm to solve this linear equation. The basis functions with nodal point located inside of one layer do not overlay with the other basis functions with nodal point located inside of the other layers. As a result, the non-diagonal matrix elements across these two groups of basis functions are zero. We can rearrange the sequence of the basis function, so that the basis functions inside of one layer are grouped together. In addition, the basis functions with nodal point on the same interface between two adjacent layers are grouped together. As a result, the stiffness and mass matrix is a block tri-diagonal as shown in Figure 27. Instead of directly solving the linear equation of a block tri-diagonal matrix by LU decomposition, we can use the block Thomas algorithm[57] to solve this equation. For a linear equation with a two-by-two block matrix

$$\begin{bmatrix} A & B \\ C & D \end{bmatrix} \begin{bmatrix} x \\ y \end{bmatrix} = \begin{bmatrix} u \\ v \end{bmatrix} \tag{2.3.1}$$

The solution is

$$\begin{cases} x = -A^{-1}By + A^{-1}u \\ y = (D - CA^{-1}B)^{-1}(v - CA^{-1}u) \end{cases} \tag{2.3.2}$$

If we put the first diagonal block in the matrix in Figure 27 as the block matrix A, and the rest of the diagonal block as the block matrix D, we only need to calculate the LU decomposition of A to reduce the size of the system. Because A only contain the basis functions in one layer, the number of unknown is relatively small. We can recursively

use this formula to each diagonal block matrix of each layer, and solve the whole linear equation layer by layer. If the number of layer increase, the computational cost increase linearly, because we only need to increase the times of LU decomposition of a diagonal block matrix.

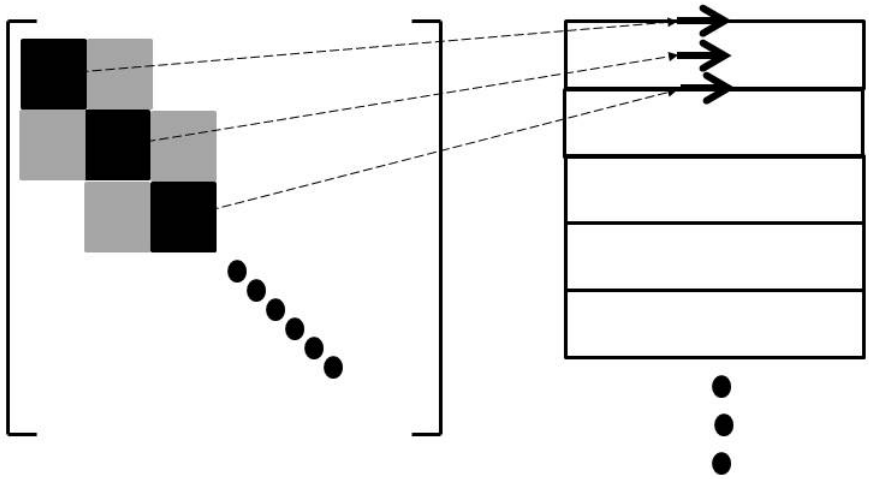

Figure 27. The structure of stiffness and(or) mass matrix of a multiple layer system. The dash arrows link the sub-matrix with the group of basis functions inside of one layer or on the interface of two adjacent layers. The block diagonal matrixes are black, and the block tri-diagonal matrixes are gray. The other off diagonal matrixes are zero.

We have implemented this method to calculate scattering of multiple layer photonic crystal slab. The spatial structure of the system is shown in Figure 28. The red layers consist of GaAs, and the blue layers consist of AlAs. The periodic AlAs cylinder going through all layers makes a two dimensional photonic crystal slab structure. A two-by-two periods is plotted in Figure 28. We have calculated the transmission rate under normal incident plane wave at varying wavelength. As comparison, we use the

commercial software HFSS to calculate the same system. The results are plotted in Figure 29. The figure shows that out SEM result match with the result given by HFSS.

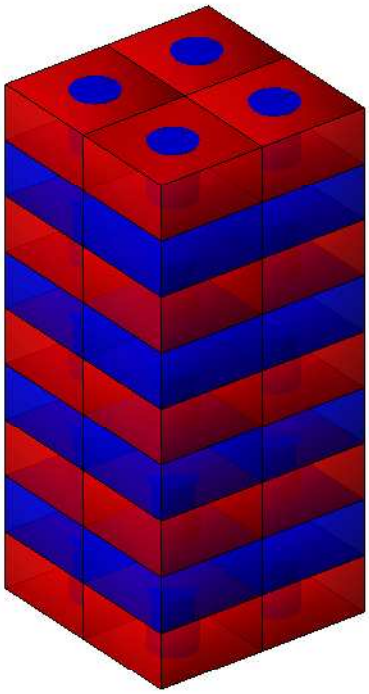

Figure 28. Spatial structure of a five layer GaAs/AlAs DBR with periodic AlAs cylinder. A two-by-two periods is plotted in this figure.

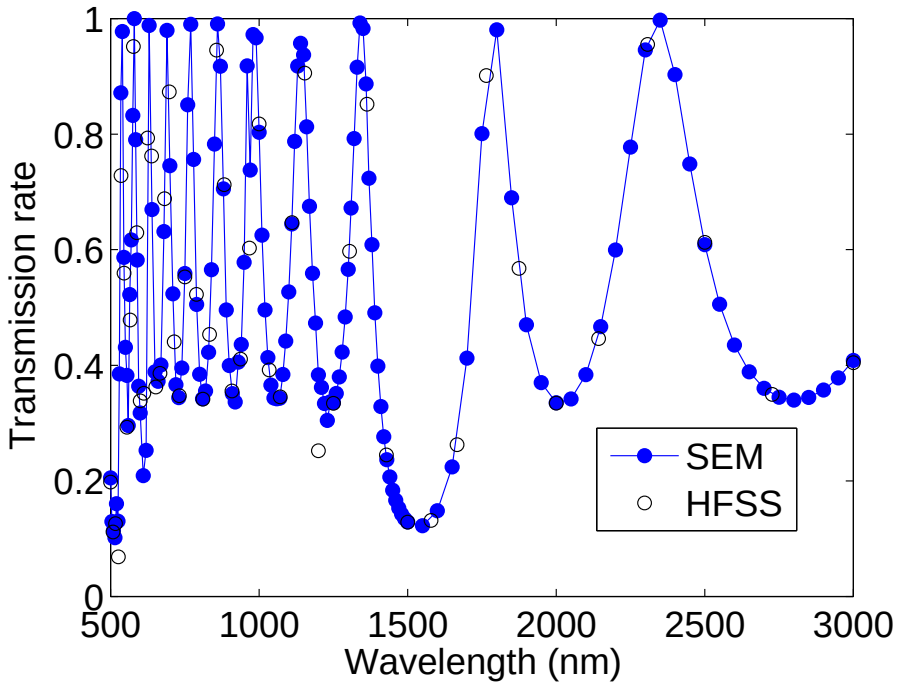

Figure 29. Transmission rate of normal incident plane wave versus the wavelength. The result of SEM with block-Thomas algorithm and the result from HFSS is compared.

2.4 Domain Decomposition Method and Spectral Integral Method

The pervious section introduced the simulation for the scattered field from an infinite periodic system. For these problems, the size of the system is usually not large, because only one period is simulated with periodic boundary condition. If the system is not infinite periodic, which is the reality for a real system, the periodic boundary condition cannot be applied. Thus, the whole system needs to be discretized and solved by the SEM. In this section, we consider a finite periodic structure in all three dimensions, which is located in homogeneous medium background[58]. The system can be meshed and solved by the SEM combined with the MOM, which are described by the

equations (2.1.9), (2.2.1) and (2.2.2). Inserting the MFIE (2.2.2) into the weak form of the wave equation (2.1.9), we obtain a weak form with the radiation boundary condition as

$$\int_{\Omega} dV[(\nabla\times\mathbf{\Phi}_m)\cdot\mu_r^{-1}\cdot(\nabla\times\mathbf{E})-k_0^2\mathbf{\Phi}_m\cdot\varepsilon_r\cdot\mathbf{E}]$$
$$-jk_0\oint_{\partial\Omega} dS(\hat{n}\times\mathbf{\Phi}_m)\cdot[-\frac{1}{2}\overline{\mathbf{H}}+\varepsilon_{r(0)}L(\mathbf{M}_s)+\widetilde{K}(\overline{\mathbf{J}}_s)]=jk_0\oint_{\partial\Omega} dS(\hat{n}\times\mathbf{\Phi}_m)\cdot\overline{\mathbf{H}}^{Inc} \tag{2.4.1}$$

In addition, by testing the EFIE (2.2.1), another weak form is obtained as

$$-jk_0\oint_{\partial\Omega} dS(\hat{n}\times\mathbf{\Phi}_m)\cdot[\frac{1}{2}\mathbf{E}+\mu_{r(0)}L(\overline{\mathbf{J}}_s)-\widetilde{K}(\mathbf{M}_s)]=jk_0\oint_{\partial\Omega} dS(\hat{n}\times\mathbf{\Phi}_m)\cdot\mathbf{E}^{Inc} \tag{2.4.2}$$

where $\varepsilon_{r(0)}$ and $\mu_{r(0)}$ are the permittivity and permeability of the background medium.

When the size of the system is much larger than the wavelength, the number of unknowns becomes larger. This will result in the larger size of the stiffness matrix and mass matrix in equation (2.4.1). In addition, the weak form of the MFIE and EFIE give full matrixes, which are becoming larger too. With this large number of unknowns, the computer consumes more memory to store the matrixes. In addition, the condition of the system matrix is poor, so the iterative solver takes a long time to reach the convergent condition or does not converge. One of the solutions to this bottleneck is to introduce domain decomposition method (DDM)[59-62]. The idea of the DDM is to split the whole system into a few smaller subdomains. Each of the small subdomains can be solved by direct solver. The solution of the whole system is iteratively obtained by counting the influence between adjacent subdomains. At the interface between the adjacent

subdomains, the influence between them is modeled by a transmission condition. In addition to model the physics of scattering field at the interface, the transmission condition need to be able to guarantee the convergence of the iteration. The Robin type transmission was implemented[59,61], which exhibited fast convergence behavior. In order to improve the convergence speed, the other transmission condition is implemented, called the Riemann solver transmission condition[63-65]. The Riemann solver model the scattering at the interface by impedance matching condition, so the transmission of the field from one subdomain to the adjacent subdomain is more efficient. Thus, the convergence speed is improved.

The configuration of the simulated system is a square lattice finite periodic object with $N^{(D)} = N_x \times N_y \times N_z$ periods, with N_x, N_y and N_z being the number of periods at x, y and z direction. Each period is defined as one SEM subdomain, which is modeled by the spectral element method. The homogeneous background is defined as the $(N^{(D)}+1)$ th subdomain, which is modeled by the method of moments (MOM). Because the method of moments is efficiently solved by the spectral integral method (SIM)[66,67], this domain is denoted as the SIM subdomain. The Riemann solver between two adjacent SEM subdomains, e.g. the subdomain (i) and the subdomain (j), is defined as

$$\left(\hat{n}\times\mathbf{E}\right)\left(Y^{(i)}+Y^{(j)}\right)=\hat{n}\times\left(Y^{(i)}\mathbf{E}^{(i)}-\hat{n}\times\overline{\mathbf{H}}^{(i)}\frac{1}{Z_0}+Y^{(j)}\mathbf{E}^{(j)}-\hat{n}\times\overline{\mathbf{H}}^{(j)}\frac{1}{Z_0}\right) \tag{2.4.3}$$

$$\left(\hat{n}\times\overline{\mathbf{H}}\right)\left(Z^{(i)}+Z^{(j)}\right)=\hat{n}\times\left(Z^{(i)}\overline{\mathbf{H}}^{(i)}+\hat{n}\times\mathbf{E}^{(i)}Z_0+Z^{(j)}\overline{\mathbf{H}}^{(j)}-\hat{n}\times\mathbf{E}^{(j)}Z_0\right) \tag{2.4.4}$$

where $\hat{n}$ is the normal unit vector pointing from the subdomain (i) to the subdomain (j); $Z^{(i)}$, $Y^{(i)}=1/Z^{(i)}$, $\mathbf{E}^{(i)}$ and $\overline{\mathbf{H}}^{(i)}$ are the impedance distribution, the inductance distribution, the electric field and the magnetic field at the surface of the subdomain (i); $\mathbf{E}$ and $\overline{\mathbf{H}}$ are the electric field and magnetic field on the interface.

Inserting the Riemann solver (2.4.4) into the weak form of the SEM subdomain (i), the weak form becomes

$$\begin{aligned}&\int_{\Omega^{(i)}} dV[(\nabla\times\mathbf{\Phi}_m)\cdot\mu_r^{-1}\cdot(\nabla\times\mathbf{E}^{(i)})-k_0^2\mathbf{\Phi}_m\cdot\varepsilon_r\cdot\mathbf{E}^{(i)}]\\&-jk_0\oint_{\partial\Omega^{(i)}} dS\frac{\mathbf{\Phi}_m}{Z^{(i)}+Z^{(j)}}\cdot\hat{n}\times(Z^{(i)}\overline{\mathbf{H}}^{(i)}+\hat{n}\times\mathbf{E}^{(i)}Z_0+Z^{(j)}\overline{\mathbf{H}}^{(j)}-\hat{n}\times\mathbf{E}^{(j)}Z_0)=0\end{aligned} \tag{2.4.5}$$

where the electric field in the volume and on the surface of the subdomain (i) is interpolated as

$$\mathbf{E}^{(i)}=\sum_{n\in\Omega^{(i)}}^{n\notin\partial\Omega^{(i)}}E_n^{(i)}\mathbf{\Phi}_n+\sum_{n\in\partial\Omega^{(i)}}E_n^{(i)}\mathbf{\Phi}_n \tag{2.4.6}$$

and the magnetic field on the surface of the subdomain (j) is interpolated by the same set of basis functions, as

$$\overline{\mathbf{H}}^{(i)}=\sum_{n\in\partial\Omega^{(i)}}Z_0H_n^{(i)}\mathbf{\Phi}_n \tag{2.4.7}$$

The same interpolation of the electromagnetic field applies to the others SEM subdomain. Inserting the interpolation (2.4.6) and (2.4.7) into the weak form (2.4.5), we obtained an $N^{(SEM)}\times(N^{(SEM)}+N_S^{(SEM)})$ matrix equation, with $N^{(SEM)}=N_I^{(SEM)}+N_S^{(SEM)}$, $N_I^{(SEM)}$ being the number of basis functions inside the SEM subdomain, $N_S^{(SEM)}$ being

the number of basis functions on the surface of the SEM subdomain. Because all of the SEM subdomains have the same mesh, the subdomain index is omitted for the number of the basis function. In order to solve the system equation, the other $N_S^{(SEM)}$ equations are needed to form a square matrix equation. These equations are given by testing the Riemann solver (2.4.3), as

$$\oint_{\partial\Omega^{(i)}} dS \frac{\mathbf{\Phi}_m}{Y^{(i)}+Y^{(j)}} \cdot \hat{n} \times (Y^{(j)}\mathbf{E}^{(i)} - \hat{n} \times \overline{\mathbf{H}}^{(i)} \frac{1}{Z_0} + Y^{(j)}\mathbf{E}^{(j)} - \hat{n} \times \overline{\mathbf{H}}^{(j)} \frac{1}{Z_0}) = 0 \qquad (2.4.8)$$

and inserting the interpolation of the electric and magnetic fields into this equation. As a result, we have an $(N^{(SEM)} + N_S^{(SEM)}) \times (N^{(SEM)} + N_S^{(SEM)})$ matrix equation of the subdomain (i), and the electric and magnetic field from the adjacent subdomain (j) is the source term for this matrix equation. Because there is more than one adjacent subdomain of each subdomain, the weak form (2.4.5) and (2.4.8) imply a summation through all of the adjacent subdomains (j).

On the interface between the SEM subdomains and the SIM subdomain, the Riemann solvers (2.4.3) and (2.4.4) are also used to model the transmission from the object to the background. Because the background medium is homogeneous, the MOM only require unknown on the surface. The surface is meshed by uniform grid. And the basis functions are constructed as linear tangential/constant normal (LT/CN) type basis function at the edge. The number of edge is $N^{(S)}$, which is also the number of basis functions. The basis functions for electric and magnetic fields are the same type of

function with different notation, $\mathbf{e}_n$ and $\mathbf{h}_n$. Thus, the electric and magnetic fields are interpolated as

$$\mathbf{E}^{(SIM)} = \sum_{n=1}^{N^{(S)}} E_n^{(S)} \mathbf{e}_n \tag{2.4.9}$$

$$\overline{\mathbf{H}}^{(SIM)} = \sum_{n=1}^{N^{(S)}} Z_0 H_n^{(S)} \mathbf{h}_n \tag{2.4.10}$$

where $E_n^{(S)}$ and $H_n^{(S)}$ is the electric and magnetic field at the edge of the basis function. The interpolated electric and magnetic field (2.4.9) and (2.4.10) are inserted into the EFIE to obtain the weak from of the EFIE, which is a $N^{(S)} \times 2N^{(S)}$ matrix equation. In order to obtain a square matrix equation, the electric field Riemann solver (2.4.3) is tested by the SIM basis function too. Thus, another weak form that gives a $N^{(S)} \times 2N^{(S)}$ matrix equation is obtained as

$$\oint_{\partial\Omega} dS \frac{\mathbf{e}_m}{Y^{(SIM)} + Y^{(SEM)}} \cdot \hat{n} \times (Y^{(SEM)} \mathbf{E}^{(SIM)} - \hat{n} \times \overline{\mathbf{H}}^{(SIM)} \frac{1}{Z_0} + Y^{(SEM)} \mathbf{E}^{(SEM)} - \hat{n} \times \overline{\mathbf{H}}^{(SEM)} \frac{1}{Z_0}) = 0 \tag{2.4.11}$$

where $\mathbf{E}^{(SEM)}$ and $\overline{\mathbf{H}}^{(SEM)}$ are the electric and magnetic fields at the surface of the SEM domain, $Y^{(SIM)}$ and $Y^{(SEM)}$ is the admittance distribution of the SIM domain and the SEM domains.

The over all matrix equations of the domain decomposition method are given as follow. For the $N^{(D)}$ SEM domains, the matrix equations are

$$\mathbf{P}^{(i)}\mathbf{F}^{(i)} = \mathbf{J}^{(i)} + \sum_{j\neq i}^{j\in neighbor(i)} \mathbf{Q}^{(i,j)}\mathbf{F}^{(j)} + \mathbf{Q}^{(i,SIM)}\mathbf{F}^{(SIM)} \tag{2.4.12}$$

where

$$\mathbf{P}^{(i)} = \begin{bmatrix} \mathbf{S}_{II}^{(i)} - k_0^2\mathbf{M}_{II}^{(i)} & \mathbf{S}_{IS}^{(i)} - k_0^2\mathbf{M}_{IS}^{(i)} & 0 \\ \mathbf{S}_{SI}^{(i)} - k_0^2\mathbf{M}_{SI}^{(i)} & \mathbf{S}_{SS}^{(i)} - k_0^2\mathbf{M}_{SS}^{(i)} + \mathbf{B}^{(i)} & \mathbf{D}^{(i)} \\ 0 & \mathbf{R}^{(i)} & \mathbf{T}^{(i)} \end{bmatrix} \tag{2.4.13}$$

$$\mathbf{F}^{(i)} = [\mathbf{E}_I^{(i)}, \mathbf{E}_S^{(i)}, \overline{\mathbf{H}}_S^{(i)}]^T \tag{2.4.14}$$

$$\mathbf{J}^{(i)} = [\mathbf{J}_I^{(i)}, \mathbf{J}_S^{(i)}, 0]^T \tag{2.4.15}$$

$$\mathbf{Q}^{(i,j)} = \begin{bmatrix} 0 & 0 & 0 \\ 0 & \mathbf{B}^{(i,j)} & \mathbf{D}^{(i,j)} \\ 0 & \mathbf{R}^{(i,j)} & \mathbf{T}^{(i,j)} \end{bmatrix} \tag{2.4.16}$$

$$\mathbf{Q}^{(i,SIM)} = \begin{bmatrix} 0 & 0 \\ \mathbf{B}^{(i,SIM)} & \mathbf{D}^{(i,SIM)} \\ \mathbf{R}^{(i,SIM)} & \mathbf{T}^{(i,SIM)} \end{bmatrix} \tag{2.4.17}$$

$$\mathbf{F}^{(SIM)} = [\mathbf{E}^{(SIM)}, \overline{\mathbf{H}}^{(SIM)}]^T \tag{2.4.18}$$

The subscript I and S refer to the basis function inside the SEM subdomain and on the surface of the SEM subdomain. For example, the matrix elements of $\mathbf{S}_{IS}^{(i)}$ is $(\mathbf{S}^{(i)})_{mn}$ with the index m going through the basis functions inside the SEM subdomain, and the index n going through the basis functions on the surface of the SEM subdomain. $\mathbf{S}^{(i)}$ and $\mathbf{M}^{(i)}$ are the stiffness and mass matrix of the SEM subdomain (i). From the equation (2.4.5), the matrix element of $\mathbf{B}^{(i)}$, $\mathbf{D}^{(i)}$, $\mathbf{B}^{(i,j)}$, and $\mathbf{D}^{(i,j)}$ are

$$\left(\mathbf{B}^{(i)}\right)_{mn} = -jk_0 \int_{\partial\Omega} dS \frac{\mathbf{\Phi}_m}{Z^{(i)} + Z^{(j)}} \cdot (\hat{n} \times \hat{n} \times \mathbf{\Phi}_n) Z_0 \tag{2.4.19}$$

$$\left(\mathbf{D}^{(i)}\right)_{mn} = -jk_0 \int_{\partial\Omega} dS \frac{Z^{(i)}\mathbf{\Phi}_m}{Z^{(i)} + Z^{(j)}} \cdot (\hat{n} \times \mathbf{\Phi}_n) Z_0 \tag{2.4.20}$$

$$\left(\mathbf{B}^{(i,j)}\right)_{mn} = -jk_0 \int_{\partial\Omega} dS \frac{\mathbf{\Phi}_m{}^{(i)}}{Z^{(i)} + Z^{(j)}} \cdot (\hat{n} \times \hat{n} \times \mathbf{\Phi}_n{}^{(j)}) Z_0 \tag{2.4.21}$$

$$\left(\mathbf{D}^{(i,j)}\right)_{mn} = jk_0 \int_{\partial\Omega} dS \frac{Z^{(i)}\mathbf{\Phi}_m{}^{(i)}}{Z^{(i)} + Z^{(j)}} \cdot (\hat{n} \times \mathbf{\Phi}_n{}^{(j)}) Z_0 \tag{2.4.22}$$

In equation (2.4.19) and (2.4.20), both test functions and basis functions are from the subdomain (i); in equation (2.4.21) and (2.4.22), the test functions are from the subdomain (i), and the basis function are from the subdomain (j). Similarly, from equation (2.4.8), the matrix element of $\mathbf{R}^{(i)}$, $\mathbf{T}^{(i)}$, $\mathbf{R}^{(i,j)}$, and $\mathbf{T}^{(i,j)}$ are,

$$\left(\mathbf{R}^{(i)}\right)_{mn} = -jk_0 \int_{\partial\Omega} dS \frac{Y^{(j)}\mathbf{\Phi}_m}{Y^{(i)} + Y^{(j)}} \cdot (\hat{n} \times \mathbf{\Phi}_n) \tag{2.4.23}$$

$$\left(\mathbf{T}^{(i)}\right)_{mn} = jk_0 \int_{\partial\Omega} dS \frac{\mathbf{\Phi}_m}{Y^{(i)} + Y^{(j)}} \cdot (\hat{n} \times \hat{n} \times \mathbf{\Phi}_n) \tag{2.4.24}$$

$$\left(\mathbf{R}^{(i,j)}\right)_{mn} = jk_0 \int_{\partial\Omega} dS \frac{Y^{(j)}\mathbf{\Phi}_m{}^{(i)}}{Y^{(i)} + Y^{(j)}} \cdot (\hat{n} \times \mathbf{\Phi}_n{}^{(j)}) \tag{2.4.25}$$

$$\left(\mathbf{T}^{(i,j)}\right)_{mn} = -jk_0 \int_{\partial\Omega} dS \frac{\mathbf{\Phi}_m{}^{(i)}}{Y^{(i)} + Y^{(j)}} \cdot (\hat{n} \times \hat{n} \times \mathbf{\Phi}_n{}^{(j)}) \tag{2.4.26}$$

In order to keep the system matrix $\mathbf{P}^{(i)}$ symmetric, a factor of $-jk_0$ is multiplied to equation (2.4.8). The matrix element of the matrixes in $\mathbf{Q}^{(i,SIM)}$ is similar to the matrix

element of the matrixes in $\mathbf{Q}^{(i,j)}$, except that the subdomain (j) basis functions are replaced by the SIM subdomain basis functions. For the SIM subdomain, the matrix equation is

$$\mathbf{P}^{(SIM)}\mathbf{F}^{(SIM)} = \mathbf{F}^{(Inc)} + \sum_{j \in neighbor(SIM)} \mathbf{Q}^{(SIM,j)}\mathbf{F}_S^{(j)} \tag{2.4.27}$$

where

$$\mathbf{P}^{(SIM)} = \begin{bmatrix} Z_a^{(SIM)} & Z_b^{(SIM)} \\ \mathbf{B}^{(SIM)} & \mathbf{D}^{(SIM)} \end{bmatrix} \tag{2.4.28}$$

$$\mathbf{F}^{(SIM)} = [\mathbf{E}^{(SIM)} \quad \overline{\mathbf{H}}^{(SIM)}]^T \tag{2.4.29}$$

$$\mathbf{F}^{(Inc)} = [\mathbf{E}^{(Inc)} \quad 0]^T \tag{2.4.30}$$

$$\mathbf{Q}^{(SIM,j)} = \begin{bmatrix} 0 & 0 \\ \mathbf{B}^{(SIM,j)} & \mathbf{D}^{(SIM,j)} \end{bmatrix} \tag{2.4.31}$$

$$\mathbf{F}_s^{(j)} = [\mathbf{E}_S^{(i)}, \overline{\mathbf{H}}_S^{(i)}]^T \tag{2.4.32}$$

The matrixes $Z_a^{(SIM)}$, $Z_b^{(SIM)}$ and the source vector $\mathbf{E}^{(Inc)}$ are given by the electric field integral equation (EFIE); the matrixes $\mathbf{B}^{(SIM)}$, $\mathbf{D}^{(SIM)}$, $\mathbf{B}^{(SIM,j)}$ and $\mathbf{D}^{(SIM,j)}$ are given by the electric field Riemann solver (2.4.11).

The equations (2.4.12) and (2.4.27) form a complete set of equation to describe the whole finite periodic system. Because the system is periodic, each subdomain has the same stiffness and mass matrixes. In the simulation, only one of these repeating stiffness and mass matrixes are stored, which could save a lot of computer memory. Equation

(2.4.12) is for the N SEM subdomains, so that there are totally $(N^{(D)}+1)$ matrix equations. These $(N^{(D)}+1)$ equations are solved iteratively. We first have an initial guess of the solution. Denote the solution at the i-th iteration as $\mathbf{E}(\hat{i})$. Inserting the solution $\mathbf{E}(\hat{i})$ into the right hand side of these (N+1) equations and solving them, we obtain a new solution $\mathbf{E}(\hat{i}+1/2)$. When solving each matrix equation, the fields from the adjacent subdomains are assumed to be known. The solution for the next iterative step is determined by the SOR, which gives $\mathbf{E}(\hat{i}+1)=(1-\alpha)\mathbf{E}(\hat{i}+1/2)+\alpha\mathbf{E}(\hat{i})$. The iterative error is defined as

$$e_{DDM}(\hat{i})=\frac{\max\left|\mathbf{E}(\hat{i}+1/2)-\mathbf{E}(\hat{i})\right|}{\max\left|\mathbf{E}(\hat{i}+1/2)\right|} \tag{2.4.33}$$

The iteration continues until the iterative error is smaller than a certain criteria, e.g. 1%.

2.3.1 Finite Periodic Photonic Crystal Slab

The domain decomposition method of the finite periodic system is implemented and applied to solve some problems in photonic systems. The first numerical example is the radiation of dipole source in a photonic crystal waveguide, as shown in Figure 30. The refractive index of the dielectric slab is 3.4. The thickness is 210 nm, and the radius of the air holes is 116 nm. The lattice constant of the triangular lattice is 420 nm. An

incomplete band gap exists in the triangular lattice photonic crystal slab with air holes. The line defect supports a waveguide mode, which is trapped by the band gap in the in-plane vertical direction, and by the total internal reflection in the out-of-plane vertical direction. In order to fit this system into the domain decomposition algorithm, the subdomain is defined as a rectangular volume. The top view of the mesh of one subdomain is shown in Figure 31. The area of one domain equates to twice of the primer unit cell. The simulated field pattern under a y polarization dipole source is plotted in Figure 32. The confinement of the field is observed in parallel and vertical direction. At the end of the waveguide, the reflection from the waveguide-vacuum interface produces a standing wave inside of the waveguide.

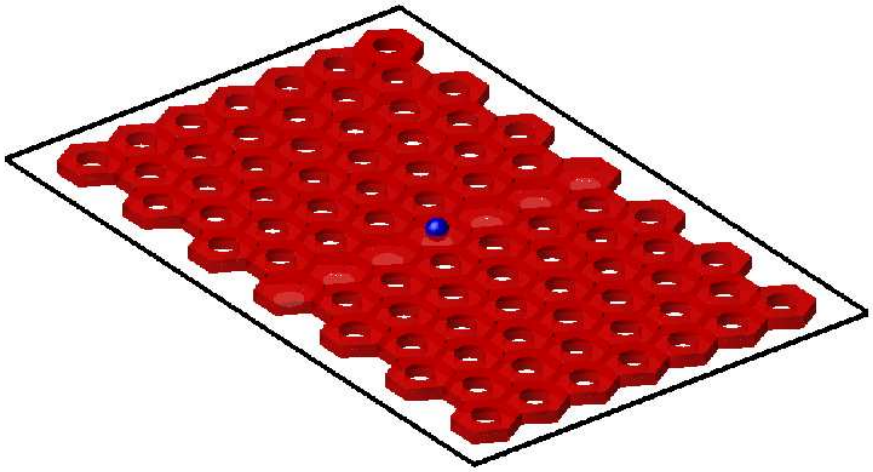

Figure 30. A waveguide constructed by line defect of missing holes in the two-dimensional photonic crystal slab with triangular air holes. A dipole source, plotted as blue sphere, locates in the middle of the waveguide.

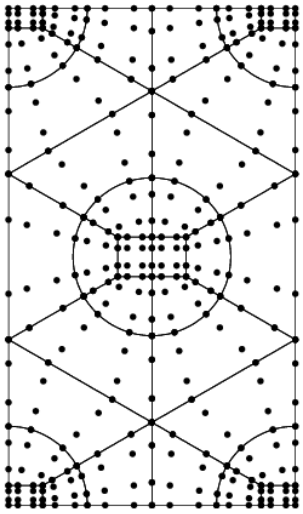

Figure 31. The top view of the mesh and nodal points of one domain for the triangular lattice photonic crystal slab. The domain is a super unit cell that is twice as the size of the primer unit cell of the triangular lattice.

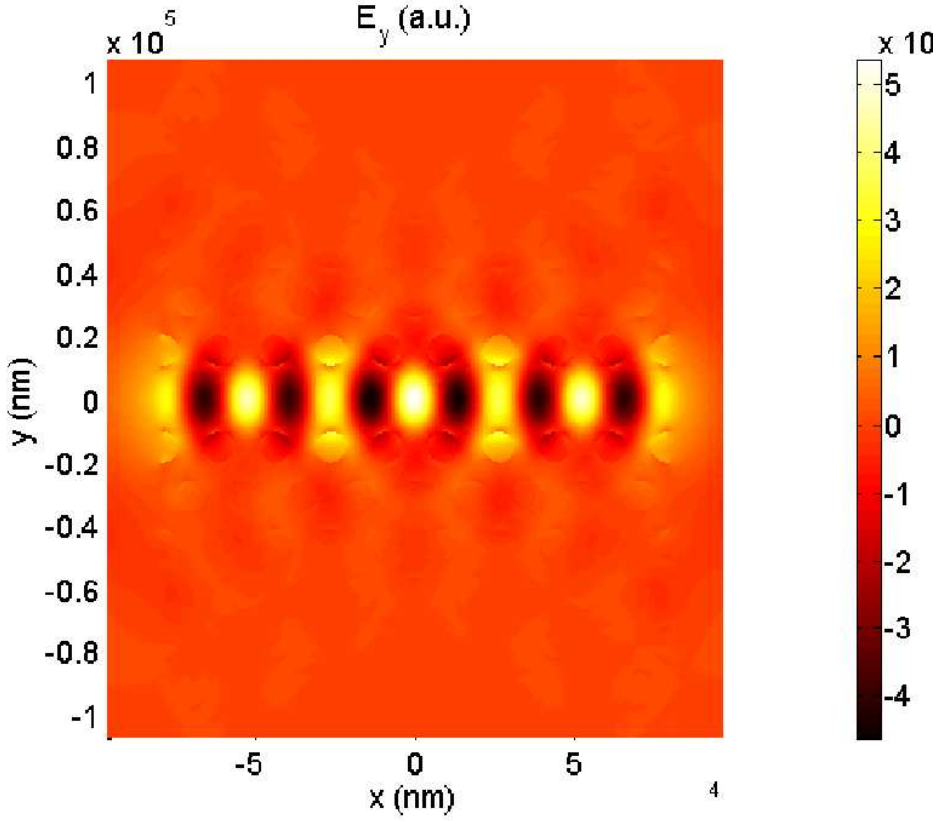

Figure 32. The field pattern of y component electric field under the excitation of the y polarization dipole source with frequency in the middle of the band gap. The field pattern is observed on the middle plane of the photonic crystal slab that is framed in Figure 30.

2.3.2 Finite Size Metamaterial Consisting of Metal Split Ring Resonator

The second numerical example is the finite size metamaterial. The structure of the metamaterial is shown in Figure 33, which is an arrangement of split ring resonators. The dimension of the split ring resonators is given in the caption of the figure. This structure was shown to have negative effective permittivity and permeability[68-70]. We have simulate a $7\times7\times7$ periods of the metamaterial bulk shown in Figure 34. A normal

incidence plane wave from the top is scattered by the metamaterial bulk. The electric field pattern is plotted in Figure 35. This simulation is helpful for the investigation of the edge effect of finite size metamaterials.

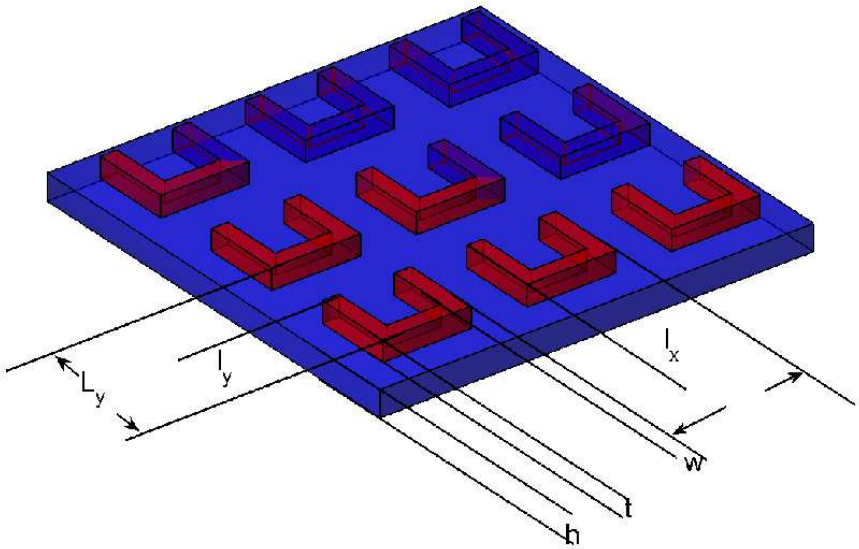

Figure 33. The configuration of the 3×3 periods of metamaterial slab. The dimension of the structure is: periods in parallel direction $L_x = L_x = 300$ nm, length of the arm of the split ring resonator $l_x = l_x = 200$ nm, width of the arm w=60 nm, height of the arm t=30 nm and thickness of the dielectric slab 40 nm. The split ring resonator consist of silver, and the dielectric slab consist of glass.

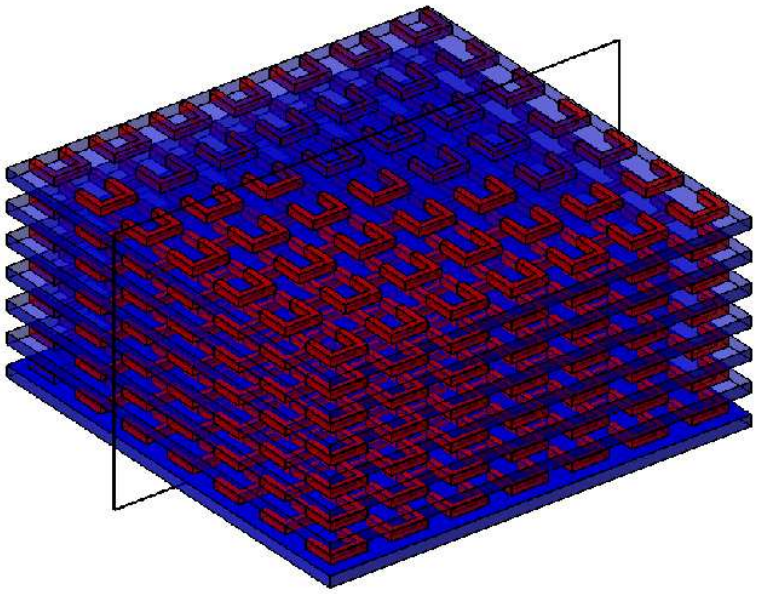

Figure 34. The configuration of the $7\times7\times7$ periods of metamaterial bulk. The dimension of the split ring resonator is shown in Figure 33. The period at vertical direction is 110 nm.

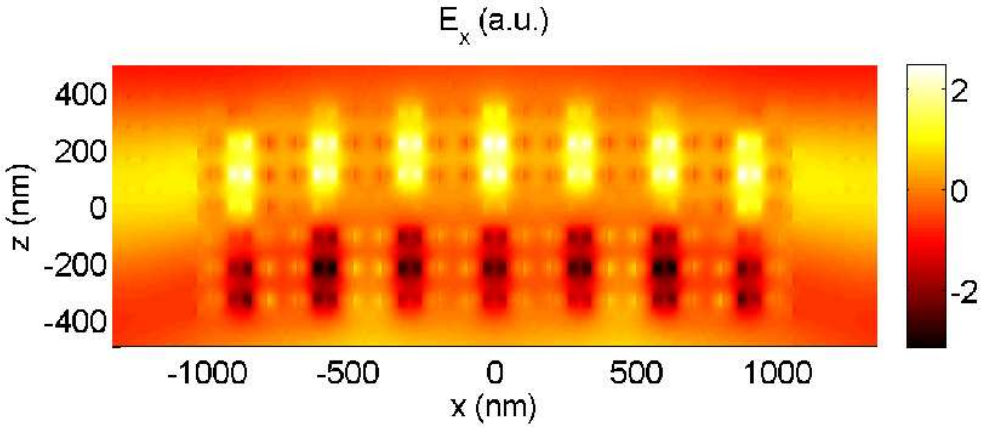

Figure 35. The field pattern of the x component electric field on the observation plan defined by the frame in Figure 34.

Chapter Three. Frequency Domain Spectral Element Method for Nonlinear and Quantum Optics

Nonlinear and quantum optical effects provide many interesting topic for numerical simulation. The nonlinear optics usually makes many approximations to the modeling of the system. Some of these approximations are not appropriate when the size of the system goes down to nano-scale. For example, in harmonic generation optics, it is assumed that the incident wave and the generated field are plane wave, with slow changing amplitude. The electric field is written as separated function of the optical mode and the amplitude of the mode, $A(\mathbf{r},t)\mathbf{E}_0(\mathbf{r},t)$ with $\mathbf{E}_0(\mathbf{r},t)$ being the optical mode and $A(\mathbf{r},t)$ being the amplitude. Thus, the second order electric field wave equation is then replaced by a first order wave equation of the amplitude. When the system is in nano-scale, the generated field is not plane wave. In addition, the optical mode and the amplitude of the mode might not be written as a separated function, because they interfere with each other. In this case, the full wave simulation based on the Maxwell's equations or the wave equation of the electric field is necessary. In this section, the effort is focused on using the spectral element method frequency solver to solve some of the nonlinear optical problems. One of the most important and widely investigated nonlinear optical effects is harmonic generation. The effort focuses on the enhancement of second harmonic generation by air bridge photonic crystal slab.

The theory of the dynamic of quantum dot gives a Maxwell-Bloch equation, which also include nonlinear optics effect. The spectral element method will be

developed to solve the nonlinear Maxwell-Bloch equation in frequency domain too. When the pumping parameter is added to the Maxwell-Bloch equations, this set of equations can describe the dynamic of laser consisting of quantum dot or quantum well. In the other hand, when the pumping parameter is not included, the Maxwell-Bloch equations describe the excitation of excitonic field in the quantum dot or quantum well.

For the excitation of exciton-polariton in quantum well, a semi-classical theory model the system by a nonlocal permittivity. This theory assumes that the exciton excitation is week, and the population inversion is always -1. Thus, Bloch equation is not needed, and the excitonic effect is modeled as a nonlocal permittivity. The model gives a linear vector Helmholtz equation of the electric field with the corresponding nonlocal permittivity. The spectral element method is used to numerically solve this equation.

Because the frequency domain simulation gives the harmonic wave solution, which have the form of $\mathbf{E}(\mathbf{r})e^{j\omega t}$, the simulated system is a continuous wave excitation system. The continuous wave system usually has low energy density comparing to the pulse wave system. Thus, the nonlinear effect is weak. Part of the motivation of this research is to investigation the enhancement of the nonlinear effect by photonic crystal structure. In section 3.1, the enhancement of the second harmonic generation by the air-bridge multiple (single) layer photonic crystal slab is described. In section 3.2, the steady state dynamic of the quantum dot in multiple layer photonic crystal slab is investigated.

In section 3.3, the spectral element method solution of the vector Helmholtz equation with nonlocal permittivity will be described.

3.1 Second Harmonic Generation

Second harmonic generation is one of the most important and widely investigated nonlinear optics effects. Because the second order susceptibility is small, the nonlinear effect is weak. The generated second harmonic optical field has low intensity. In addition, for bulk material, the phase matching condition is required to efficiently generate second harmonic field. Because most of the optical material for second harmonic generation has dispersive permittivity, the phase matching condition is usually not satisfied when the fundamental frequency field and the second harmonic field is collinear. The phase mismatch can be compensated by using sophisticated design with anisotropic material[71]. Many schemes were introduced to enhance the efficiency of the second harmonic generation in bulk medium[72], thin film medium[73,74], slow light system[75], waveguide[76,77] and resonant cavity[78]. In this subsection, the enhancement of the second harmonic generation by the resonance with the band structure of the photonic crystal slab is discussed[79].

In a second harmonic generation process, the interaction of the two incident beams with the same frequency and the nonlinear medium generate the third beam with double frequency. The nonlinear interaction is described by the second order susceptibility $\chi^{(2)}$, which is the third-order tensor. The generated second harmonic

polarization field is $\mathbf{P}^{SHG}(2k_0) = \varepsilon_0 \chi^{(2)} : \mathbf{E}(k_0)\mathbf{E}(k_0)$, which is the source of the second harmonic electric field. In this subsection, the effort is focused on the second harmonic generation of an infinite periodic two dimensional photonic crystal slab with square lattice air holes. The dielectric slab consists of Gallium phosphide (GaP). The spatial structure is the same as that in Figure 36. The thickness of the slab is 196 nm; the periodic of the square lattice is 452 nm at x and y direction; the diameter of the air hole is 190 nm. The photonic crystal slab stands in the vacuum, which is called air bridge photonic crystal slab. GaP is isotropic semiconductor with large second order susceptibility. Within the wavelength range 650 nm to 2300 nm, the permittivity is dispersive with zero imaginary part, because the frequency is far away from the resonance. The dispersive permittivity is given in reference [80]. In this frequency range, the only non-zero component of the second order susceptibility is $d_{36} = d_{25} = d_{14}$. The second order susceptibility strongly depends on the frequency. In the simulation, these coefficients are interpolated from the measured data at three frequencies, which is given in reference [81]. In our simulated system, the optical axis is the same as the coordinate axis. The surface of the dielectric slab is parallel to the (001) face of the atomic lattice of the GaP. Because there are only three non-zero component of the second order susceptibility, only the coexisting of the FF electric field at two orthogonal directions generate the SH polarization field at the third orthogonal direction. For example, if the normal incident FF field has x and y component electric field, and the system is a

homogeneous slab, only z component SH polarization field is generated. Because of the transversity of the electromagnetic field, this SH polarization field does not radiate energy outside of the slab. If the oblique incident FF field has x and z component electric field, the y component SH polarization field is generated, which can radiate energy outside of the slab. When the periodic air holes present, the scattering of the FF field generates all three components electric field. Thus, the SH polarization field can always radiate energy outside of the slab. When the SH frequency is resonant to the band structure of the photonic crystal slab, the SH radiation could be enhanced. The condition of this enhancement is discussed later.

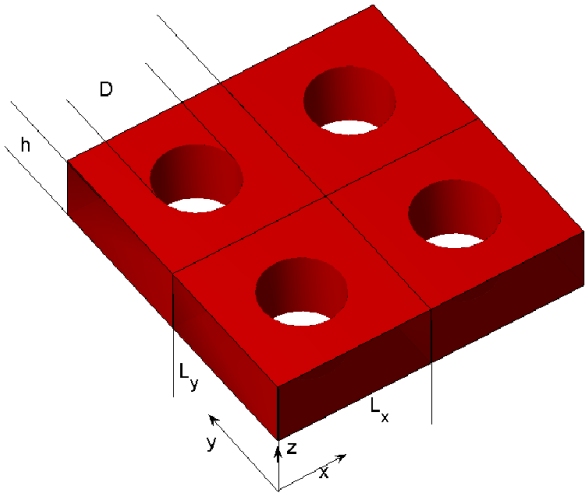

Figure 36. The spatial structure of two-by-two periods of the air bridge photonic crystal slab with square lattice air holes.

3.1.1 Simulation Formulation for the Second Harmonic Generation

In the simulation, both fundamental frequency (FF) field and second harmonic (SH) field are calculated by the SEM-MOM formula (2.2.16) and (2.2.17). The matrix form of the weak form of the FF field is

$$\begin{bmatrix} \mathbf{S}_{II} - k_0^2\mathbf{M}_{II} & \mathbf{S}_{IS} - k_0^2\mathbf{M}_{IS} & 0 \\ \mathbf{S}_{SI} - k_0^2\mathbf{M}_{SI} & \mathbf{S}_{SS} - k_0^2\mathbf{M}_{SS} + U^M(k_0) & V^M(k_0) \\ 0 & V^E(k_0) & U^E(k_0) \end{bmatrix} \begin{bmatrix} \mathbf{E}_I(k_0) \\ \mathbf{E}_S(k_0) \\ \overline{\mathbf{H}}_S(k_0) \end{bmatrix} = \begin{bmatrix} \mathbf{P}^{SHG}(k_0) \\ \mathbf{E}^{inc} \\ \overline{\mathbf{H}}^{inc} \end{bmatrix} \tag{3.1.1}$$

where $k_0 = \omega_0 / c$ is the wave number of the FF field in vacuum that is a real number, the sub-matrixes inside the matrix equation are defined in equations (2.2.22) to (2.2.27). $\mathbf{P}^{SHG}(k_0) = \varepsilon_0 \chi^{(2)} : \mathbf{E}(2k_0)\mathbf{E}(-k_0)$ is the polarization field generated by the SH field and the FF field. The matrix form of the weak form of the SH field is

$$\begin{bmatrix} \mathbf{S}_{II} - 4k_0^2\mathbf{M}_{II} & \mathbf{S}_{IS} - 4k_0^2\mathbf{M}_{IS} & 0 \\ \mathbf{S}_{SI} - 4k_0^2\mathbf{M}_{SI} & \mathbf{S}_{SS} - 4k_0^2\mathbf{M}_{SS} + U^M(2k_0) & V^M(2k_0) \\ 0 & V^E(2k_0) & U^E(2k_0) \end{bmatrix} \begin{bmatrix} \mathbf{E}_I(2k_0) \\ \mathbf{E}_S(2k_0) \\ \overline{\mathbf{H}}_S(2k_0) \end{bmatrix} = \begin{bmatrix} \mathbf{P}^{SHG}(2k_0) \\ 0 \\ 0 \end{bmatrix} \tag{3.1.2}$$

The FF field generate the SH polarization field $\mathbf{P}^{SHG}(2k_0)$, which is the source term of the SH field. In the weak form, the source terms, $\mathbf{P}^{SHG}(2k_0)$ and $\mathbf{P}^{SHG}(k_0)$, are tested by the basis functions, in the same way as testing a current source in the volume. The two equations, (3.1.1) and (3.1.2), couple to each other through the source terms given by the second harmonic polarization fields. These two equations are iteratively solved until the solutions are consistence with each other. After solving these equations, the solution is

characterized by two parameters. The first parameter is the forward and backward exiting power rate

$$R_{Forward,Backward}^{SHG} = \frac{\oint_{Bottom,Top} (\mp\hat{z}) \cdot \mathrm{Re}\left[\frac{1}{2}\mathbf{E}(2k_0) \times \mathbf{H}^*(2k_0)\right] dS}{\oint_{Top} (-\hat{z}) \cdot \mathrm{Re}\left\{\frac{1}{2}[\mathbf{E}^{inc}(k_0)] \times [\mathbf{H}^{inc}(k_0)]^*\right\} dS} \tag{3.1.3}$$

which is the ratio of the exiting power of the SH field to the incident power of the FF field. The second parameter is the stored energy

$$W_e^{SHG} = \int_{\Omega} \frac{1}{2}\mathbf{E}^*(2k_0) \cdot \mathrm{Re}[\varepsilon_r] \cdot \mathbf{E}(2k_0) dV \tag{3.1.4}$$

For convenience, the equation (2.2.21) for calculating the band structure of the air bridge photonic crystal slab is duplicated here

$$\begin{bmatrix} \mathbf{S}_{II} & \mathbf{S}_{IS} \\ \mathbf{S}_{SI} & \mathbf{S}_{SS} + U^M(\mathrm{Re}[2k_0]) - V^M(\mathrm{Re}[2k_0])[U^E(\mathrm{Re}[2k_0])]^{-1} V^E(\mathrm{Re}[2k_0]) \end{bmatrix} \begin{bmatrix} \mathbf{E}_I \\ \mathbf{E}_S \end{bmatrix} = 4k_0^2 \begin{bmatrix} \mathbf{M}_{II} & \mathbf{M}_{IS} \\ \mathbf{M}_{SI} & \mathbf{M}_{SS} \end{bmatrix} \begin{bmatrix} \mathbf{E}_I \\ \mathbf{E}_S \end{bmatrix} \tag{3.1.5}$$

Because the resonance between the SH field and the band structure will be investigated, the equation (3.1.5) uses the wave number $2k_0$, instead of k_0. The major difference between the equation (3.1.2) and the equation (3.1.5) is that the wave number $2k_0$ in (3.1.2) is always real number, and the wave number in (3.1.5) is a complex number. The form of the matrix equation is the same. When the wave number of the SH field is resonant with the band structure, there is an eigenvalue of equation (3.1.5) with the same

real part and a small imaginary part. This coincidence makes the determinant of the matrix in the left hand side of the equation (3.1.2) small, or makes the condition of this matrix poor. Thus, a small source term in the right hand side could generate large amplitude solution in the left hand side. The physical explanation is that the generated SH polarization field could excite the eigenstate in the corresponding band, when the frequency of the SH field is resonant with the band structure. When the eigenstate is excited, a large SHG effect can be observed.

3.1.2 Numerical Result of Second Harmonic Generation Enhancement

The band structure of the photonic crystal slab is calculated and plotted in Figure 37. Because the nonlinear optical effect is much weaker than the linear optical effect, the nonlinear optical coefficients are considered to be zero in the calculation of the band structure. In the figure, the light cone is plotted as dot line. The light line of normal incident is the vertical axis; the light line of 10 and 45 degrees oblique incident is the solid and dash line. Because the phase matching condition require the parallel wave vector of the FF field equal to half of the parallel wave vector of the SH field, the FF and SH field lie in the same light line corresponding to the incident angle of the FF field. The crossing point between the light line and the band structure gives the resonant frequency of the SH field. In Figure 37, each band is given an index, and is plotted by different shape of dot line. The bands with solid points are even mode (TE-like), and the bands with empty points are odd mode (TM-like). At the Γ point, the bands with red

diamond points have a finite decay time, and the bands with blue circle points have an infinite decay time. The symmetric of the field pattern on the middle plane of the slab is list in the Table 2, as well as the prominence in SHG peak under normal and oblique incidence.

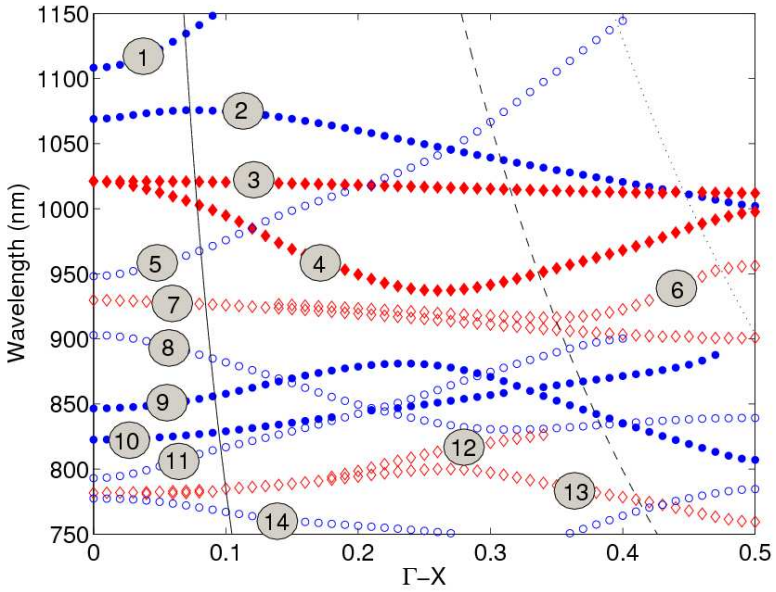

Figure 37. The band structure of the air bridge photonic crystal slab.

Table 2. Symmetry properties and prominence in SHG peaks of each band in Figure 37. [a]The prominence in SHG peaks for normal incidence refers to either exiting power rate or stored energy. [b] $E_y(y)$ and $E_z(y)$ are electric field pattern at the middle plane of the slab. [c]the prominence in SHG peaks for 45 degrees incidence refers to both two parameters.

	Decay time at Γ point	Prominence in SHG peaks under normal incidence[a]	Symmetry	$E_y(y)$ [b]	$E_z(y)$ [b]	Prominence in SHG peaks under 45 degrees oblique incidence[c]
1	Infinite	Stored energy	Even (TE-like)	Even	0	High
2	Infinite	Stored energy	Even (TE-like)	Even	0	High
3	Finite	Exiting power rate	Even (TE-like)	Odd	0	-
4	Finite	Exiting power rate	Even (TE-like)	Even	0	High

5	Infinite	Stored energy	Odd (TM-like)	0	Even	-
6	Finite	Exiting power rate	Odd (TM-like)	0	Odd	High
7	Finite	Exiting power rate	Odd (TM-like)	0	Even	-
8	Infinite	Stored energy	Odd (TM-like)	0	Even	-
9	Infinite	Stored energy	Even (TE-like)	Even	0	High
10	Infinite	Stored energy	Even (TE-like)	Odd	0	-
11	Infinite	Stored energy	Odd (TM-like)	0	Odd	High
12	Finite	Exiting power rate	Odd (TM-like)	0	Odd	High
13	Finite	Exiting power rate	Odd (TM-like)	0	Even	-
14	Infinite	Stored energy	Odd (TM-like)	0	Odd	High

The SHG exiting power rate and the stored energy are calculated and plotted in Figure 38 and Figure 39. Under normal incident, the polarization of the FF incident field is $(\hat{x}+\hat{y})/\sqrt{2}$, so that the z component SH polarization field is efficiently generated. The SHG exiting power rate and the stored energy are plotted in Figure 38. At each resonant frequency, the band structure enhances either the exiting power rate or the stored energy. If the decay time of the eigenstate is infinite, the excited eigenstate in the band stores the energy instead of radiating the energy outside of the slab. Thus, the stored energy is enhanced. The eigenstates in the other bands have finite decay time. After they are excited, they radiate the energy outside of the slab instead of storing the energy. Thus, the exiting power rate is enhanced for the resonance of these bands.

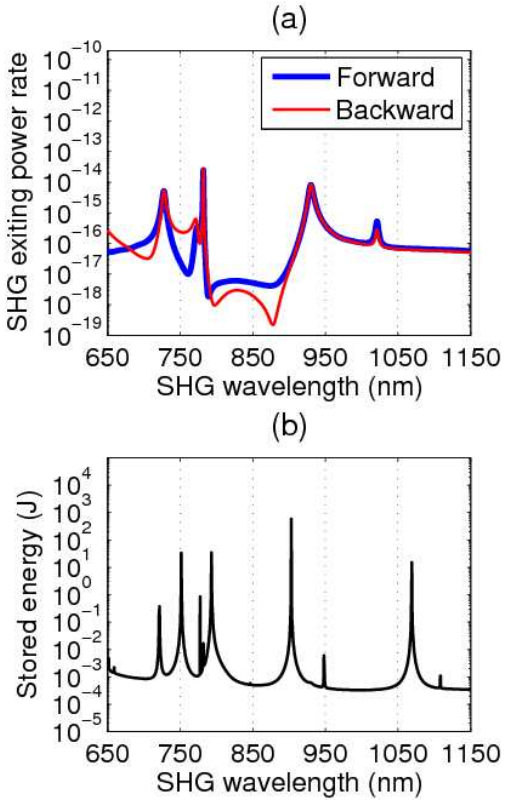

Figure 38. The SHG exiting power rate (a) and the stored energy (b) versus the SH wavelength. The FF field is normal incidence. The resonant points of the light line and the band structure with finite (infinite) decay time at the Γ point give the SHG frequencies with an enhanced exiting power rate (stored energy).

Under oblique incidence, the polarization of the incident FF electric field is in the x-z plane, which is the incident plane. Thus, the y component SH polarization field is efficiently generated. The SHG exiting power rate and stored energy are plotted in Figure 39. We first discuss large angle oblique incidence, such as 45 degrees oblique incidence, and inspect the selection rule of the resonant bands that could be excited by the SHG effect. From Figure 39 (b) and (d), we observe that the peaks of exiting power rate and stored energy have the same frequency. Once the resonant eigenstate of the

band is excited, it radiates as well as stores the energy. Some of the bands that are resonant to the light line are not excited. The excitation of the band require the symmetric matching of the field pattern between the generated SH polarization field and the eigenstate of the band that resonant with the SH frequency. As listed in the Table 2, the even mode (TE-like) will be excited, if the field pattern $E_y(y)$ in the middle plane of the slab is an even function of y coordinate. Similar, the odd mode (TM-like) will be excited, if the field pattern $E_z(y)$ is an odd function of y coordinate. Secondly, we observe the SHG effect under smaller angle incidence, such as 10 degrees incidence. From Figure 39 (a) and (c), it is still truth that the exiting power rate and stored energy have the same peak frequency. For most of the resonant frequences, the prominences of the SHG peak satisfy the same selection rule as the large angle incidence cases. In some resonant frequencies, the SHG peak is too weak to be observed even though they satisfy all of the selection rules. Thus, the SHG effects under small angle incidence satisfy the same selection rules as those given by the large angle incidence; some of the resonant peaks are weaken because they will disappear in the normal incidence limit.

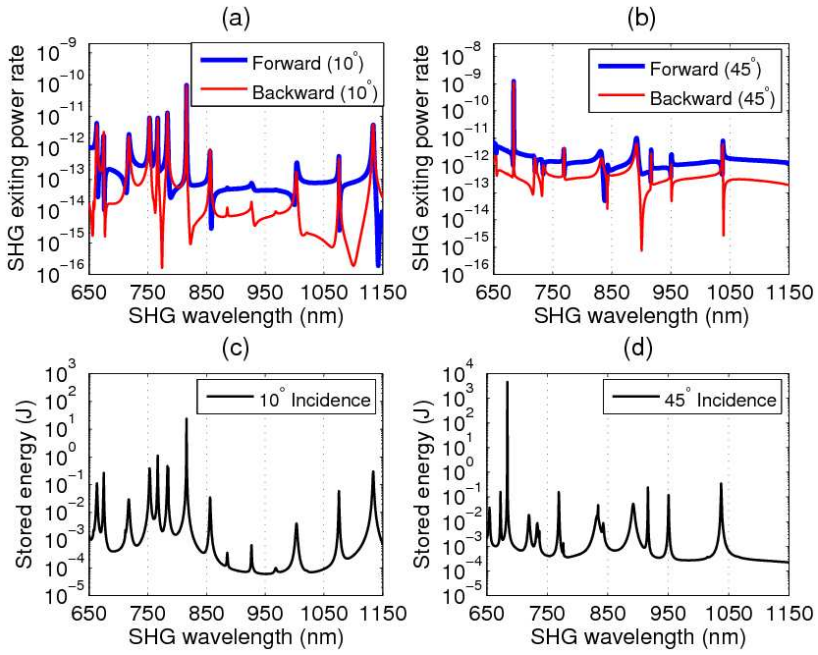

Figure 39. The SHG exiting power rate and stored energy versus SHG wavelength. The forward and backward SH exiting power rate when the incidence angle of the FF field is 10 degrees in (a) and 45 degrees in (b). The stored SH energy for (c) 10 degrees and (b) 45 degrees incidence angle. The resonant points of the light line and the band structure give the SHG frequencies with an enhanced SHG effect.

Furthermore, the SHG effects of the air bridge photonic crystal slab and the homogeneous slab are compare to get the idea about how much enhancement does the band structure resonance obtain. For normal incident, the exiting power of the SH field from the homogeneous slab is zero, so that the enhancement is not comparable. Thus, we focus on comparing the SHG effects under 45 degrees oblique incidence. The numerical result is plotted in Figure 40. From Figure 40 (a), when the SH frequency is not resonant with the band structure, the SHG exiting power rate of the air bridge photonic crystal is close to the homogeneous slab. At resonant frequency, the SHG exiting power rate is either enhanced for at least 100 times or suppressed. When

wavelength of the SH field equal to 684 nm, the exiting power rate is enhanced up to four order of magnitude. Figure 40 (b) plots the ratio between the forward and backward exiting power rate for air bridge photonic crystal slab and homogeneous slab. At the resonant frequency, the air bridge photonic crystal slab enhances or suppresses this ratio. This property gives a single directional SHG, which could be useful for some engineering application.

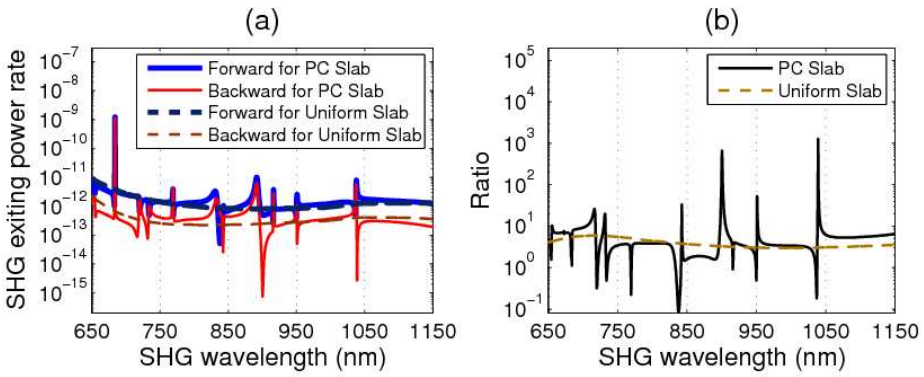

Figure 40. Comparison of SHG exiting power rate for forward and backward directions in the air bridge photonic crystal and the homogeneous slab when the incidence angle of the FF field is 45 degrees. (a) The SHG exiting power rate for the forward and backward SH wave from the air bridge photonic crystal slab and from the homogeneous slab. (b) The ratio between the forward and backward SHG exiting power of the air bridge photonic crystal slab and the homogeneous slab.

Although there is large enhancement, the SHG effect from a single layer photonic crystal slab is still too small for most of the engineering application. As a result, we have designed and calculated the SHG effect from a multiple layers photonic crystal slab to obtain large SHG effect. This structure consists of GaAs and AlAs. Both of these two semiconductors have large second order nonlinear optical coefficients. In order to obtain large SHG effect for normal incident electromagnetic field, the optical axis is rotated 45

degrees around a horizontal axis. The spatial structure of the system is plotted in Figure 41. The basic structure is a 32 layer DBR consisting of alternating layers of quarter wavelength thick GaAs and AlAs. A periodic AlAs cylinder with square lattice is inserted into the basic structure, so that the system is a multiple layer photonic crystal slab. We use the block-Thomas algorithm to solve this large system, and obtain the SHG exiting power rate. The numerical result is plotted in Figure 42. As comparison, we have calculated the SHG effect of 32 layers DBR without the periodic cylinder, and plotted the result in the same figure. The result shows that the SHG exiting power rate at most wavelength is at the same magnitude for the two systems. At some resonant wavelength, the multiple layer photonic crystal slab have large enhancement of the SHG effect comparing to the uniform DBR system. The maximum enhancement factor at the resonant wavelengths reaches up to 10^{10}. At the SHG wavelength of 665 nm, the SHG exiting power rate is 3×10^{-3}, which is large enough for practice application. Another feature of the SHG effect is that the resonant peak is very sharp. The band width of the SHG effect is narrow. If the incident fundamental field is a light source with larger band width, only a narrow band of the light is selected to be transferred into second harmonic light. As a result, the second harmonic light is highly monochromatic.

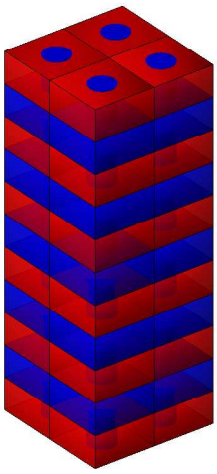

Figure 41. Spatial structure of multiple layer photonic crystal slab consisting of GaAs/AlAs DBR with periodic AlAs cylinder. The thickness of each layer is quarter wavelength at 1559 nm. The periodic is 420 nm, and the diameter of the cylinder is 190 nm. The calculated system has 32 layers.

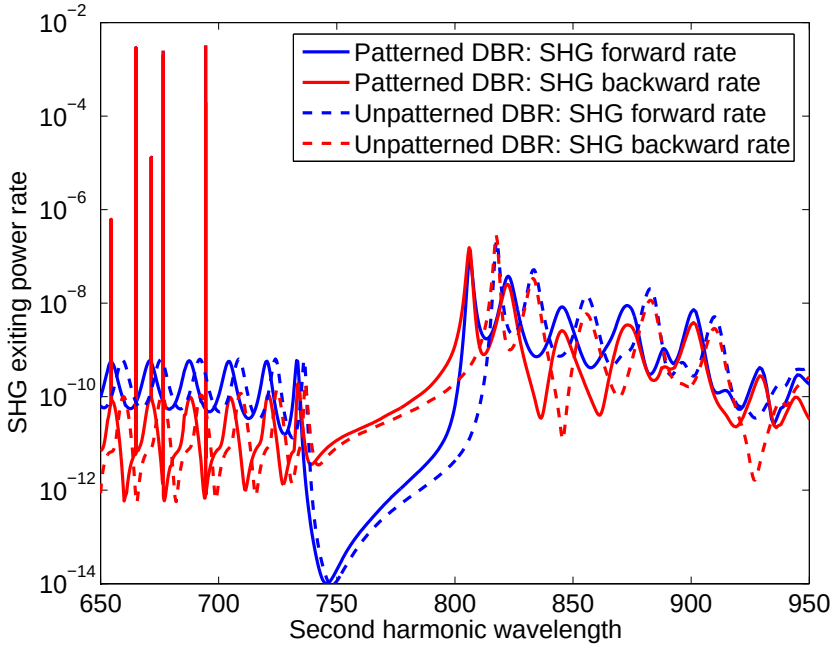

Figure 42. The SHG exiting power rate of 32 layers photonic crystal slab is plotted. As comparison, the result from a basic DBR structure with 32 layers is also plotted.

3.1.3 Sensitivity Analysis of Second Harmonic Generation Enhancement

In the previous simulation, the dimensions of the photonic crystal are exact. For example, the thickness of each layer is exactly equal to the quarter wavelength at 1550 nm, and the thickness of each layer is exactly the same. In actual fabrication, the thickness of a photonic crystal slab is not precise. In this sub-section, we discuss the sensitivity of the transmission/reflection rate and SHG effect to the thickness of each layer. We start with the sensitivity of the electric field to the thickness of the l-th layer, $\partial \mathbf{E}(k_0)/\partial d^l$. The field of the sensitivity can be expanded by the same basis functions in the same way as the electric field in Eq. (2.1.8). Thus, we firstly calculate the sensitivity of the expansion coefficients of the weak form, $\partial E(k_0)/\partial d^l$; and then insert the coefficients into Eq. (2.1.8) to obtain the sensitivity of the electric field. At first, we rewrite the equation (3.1.1) and (3.1.2) in a compact form as

$$\mathbf{K}(k_0)E(k_0) = P^{SHG}(k_0) + E^{inc} \tag{3.1.6}$$

$$\mathbf{K}(2k_0)E(2k_0) = P^{SHG}(2k_0) \tag{3.1.7}$$

where $\mathbf{K}(k_0)$ is the combination of the stiffness matrix, mass matrix and the boundary integral matrix. Taking the differential of these two equations to the thickness of the l-th layer, and rearranging the terms, we have the equations to calculate the sensitivity of the electric field as

$$\frac{\partial E(k_0)}{\partial d^l} = \mathbf{K}(k_0)^{-1}\left[-\frac{\partial \mathbf{K}(k_0)}{\partial d^l}E(k_0) + \frac{\partial P^{SHG}(k_0)}{\partial d^l}\right] \tag{3.1.8}$$

$$\frac{\partial E(2k_0)}{\partial d^l} = \mathbf{K}(2k_0)^{-1}\left[-\frac{\partial \mathbf{K}(2k_0)}{\partial d^l}E(2k_0) + \frac{\partial P^{SHG}(2k_0)}{\partial d^l}\right] \tag{3.1.9}$$

After some algebra operation, we found that $\partial \mathbf{K}(k_0)/\partial d^l$ can be calculated by making the replacement $\varepsilon_r \Rightarrow diag\left\{(\varepsilon_r)_{11}/d^l, (\varepsilon_r)_{22}/d^l, -(\varepsilon_r)_{33}/d^l\right\}$ and $\mu_r \Rightarrow diag\left\{-(\mu_r)_{11}/d^l, -(\mu_r)_{22}/d^l, (\mu_r)_{33}/d^l\right\}$ in the l-th layer; in the other layer, the differential of the matrix $\mathbf{K}(k_0)$ to d^l is zero. The differential of the second harmonic polarization field is calculated as following

$$\frac{\partial P_i^{SHG}(k_0)}{\partial d^l} = \int_\Omega dV\left\{-\frac{\delta_{l,l'}}{d^l}\mathbf{\Phi}_i \cdot \mathbf{P}(k_0) + \varepsilon_0 \mathbf{\Phi}_i \cdot \chi^{(2)} : \frac{\partial \mathbf{E}(2k_0)}{\partial d^l}\mathbf{E}(k_0) + \varepsilon_0 \mathbf{\Phi}_i \cdot \chi^{(2)} : \mathbf{E}(2k_0)\frac{\partial \mathbf{E}(k_0)}{\partial d^l}\right\}$$

(3.1.10)

$$\frac{\partial P_i^{SHG}(2k_0)}{\partial d^l} = \int_\Omega dV\left\{-\frac{\delta_{l,l'}}{d^l}\mathbf{\Phi}_i \cdot \mathbf{P}(2k_0) + \varepsilon_0 \mathbf{\Phi}_i \cdot \chi^{(2)} : \frac{\partial \mathbf{E}(k_0)}{\partial d^l}\mathbf{E}(k_0) + \varepsilon_0 \mathbf{\Phi}_i \cdot \chi^{(2)} : \mathbf{E}(k_0)\frac{\partial \mathbf{E}(k_0)}{\partial d^l}\right\}$$

(3.1.11)

The source term in Eq. (3.1.8) and (3.1.9) contain the product of electric field and the sensitivity of the electric field. As a result, Eq. (3.1.8) and (3.1.9) are nonlinear equation of the electric field sensitivity. In the implementation, the sensitivity is iteratively solved in parallel with the solving of the SHG effect itself. In one iterative step, the electric field and sensitivity from the previous iterative step are inserted in the right hand side of Eq. (3.1.8) and (3.1.9) to obtain the sensitivity for the current iterative step. The iteration

stops when both the electric field and the sensitivity convergent. After we obtain the sensitivity of the electric field, we can calculate the sensitivity of the Poynting vector as follow

$$\frac{\partial \mathbf{S}_{Poynting}}{\partial d^l} = \frac{1}{2}\mathrm{Re}\left[\frac{\partial \mathbf{E}}{\partial d^l} \times \mathbf{H}^* + \mathbf{E} \times \frac{\partial \mathbf{H}^*}{\partial d^l}\right] \tag{3.1.12}$$

The sensitivity of the SHG exiting power rate can be calculated by using the sensitivity of the Poynting vector.

We have calculated the sensitivity of the 32 layer GaAs/Alas photonic crystal slab. At first, we neglect the second order nonlinear optical effect and inspect the sensitivity of the linear scattering property. The sensitivity equations become

$$\frac{\partial E(k_0)}{\partial d^l} = -\mathbf{K}(k_0)^{-1} \frac{\partial \mathbf{K}(k_0)}{\partial d^l} E(k_0) \tag{3.1.13}$$

$$\frac{\partial E(2k_0)}{\partial d^l} = -\mathbf{K}(2k_0)^{-1} \frac{\partial \mathbf{K}(2k_0)}{\partial d^l} E(2k_0) \tag{3.1.14}$$

We can calculate the sensitivity of the linear transmission rate and reflection rate from the result of these two equations. The result is plotted in Figure 43. The sensitivity inside of the DBR band gap is small. At the resonant wavelength, the magnitude of the sensitivity is a few times larger, compared to the sensitivity at the non-resonant wavelength. We have zoomed in the plot and showed the result around one of the resonant wavelength, 1330.01 nm, in Figure 44. Notice the resonant peak of transmission rate, the sensitivity is negative at the left side of the peak, and positive at the right side of

the peak. The other peak and valley have the consistent property. This implies that if the thickness of the middle layer increases, the resonant peak will shift to the higher wavelength. Next, we calculate the sensitivity of the SHG exiting power rate. The result is shown in Figure 45. The characteristics are similar to the sensitivity of the linear transmission/reflection rate. At resonant wavelength, the magnitude of the sensitivity is much larger than that at non-resonant wavelength.

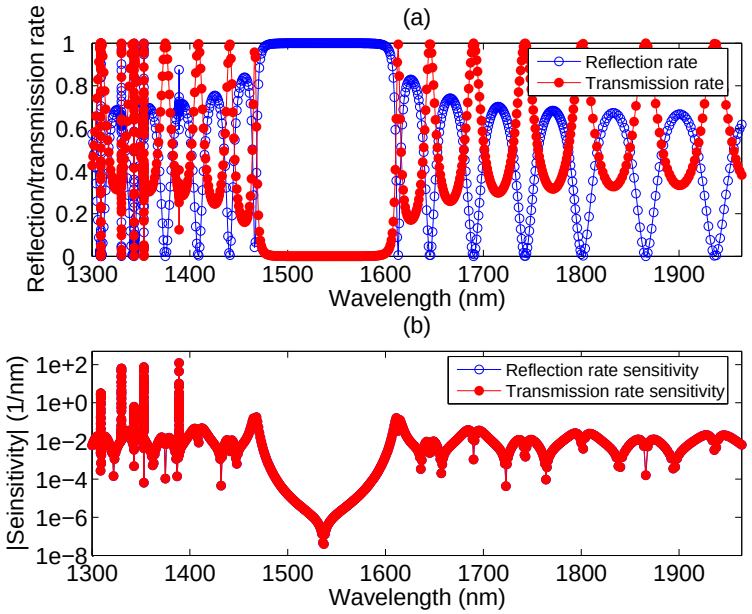

Figure 43. (a) The linear transmission rate and reflection rate of the 32 layer GaAs/AlAs photonic crystal slab. (b) The absolute value of the sensitivity of the transmission/reflection rate to the thickness of the middle layer of the system.

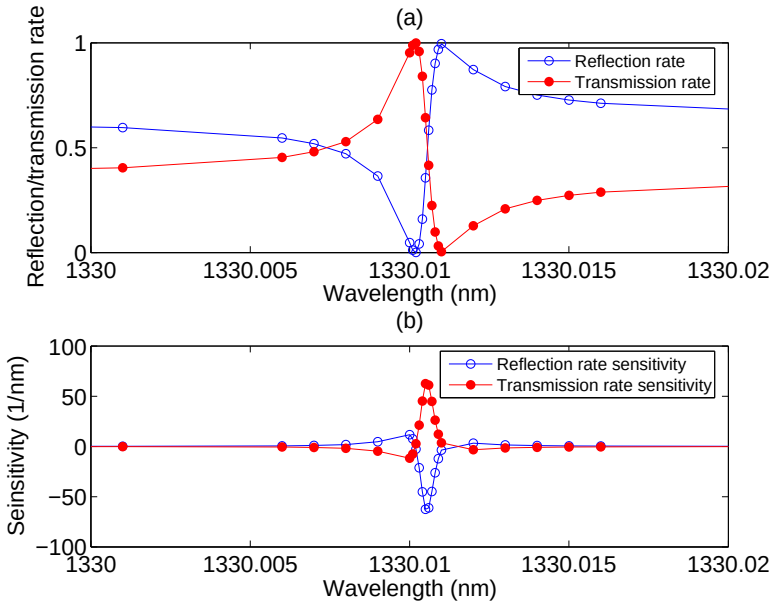

Figure 44. The same as Figure 43, but zoom in around one of the resonant wavelength at 1330.01 nm.

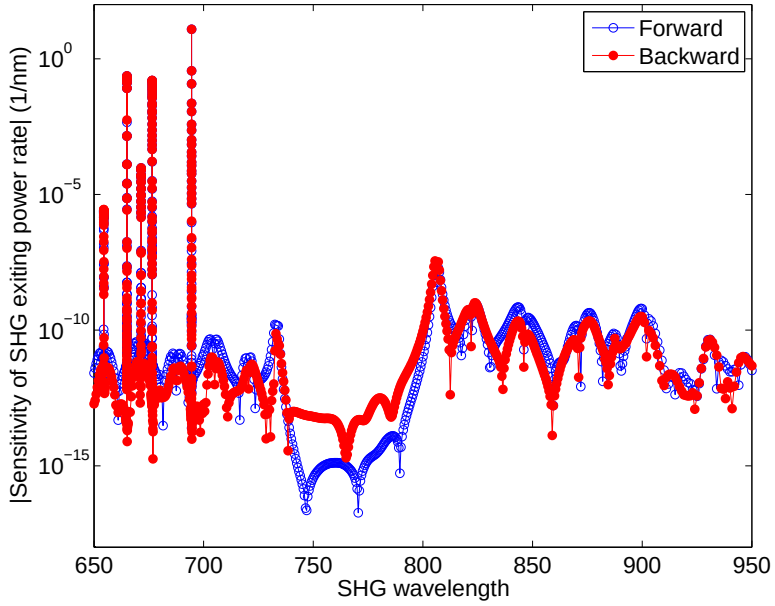

Figure 45. The absolute value of the sensitivity of the SHG exiting power rate to the thickness of the middle layer of the 32 layer GaAs/AlAs photonic crystal slab.

3.2 Quantum Dot Steady State Dynamic in Photonic Crystal Slab

From the result of previous sub-section, a multiple layer photonic crystal slab has resonant modes. At the resonant wavelength, the resonant peak is sharp, which implies that the confinement of the resonant mode is tight to the slab. In this sub-section, the quantum dots are put in some of the layer inside the photonic crystal slab. The second harmonic generation from GaAs and AlAs is neglected. The dynamics of the quantum dot is described by the Bloch equation. The Bloch equation also models the interaction between the electromagnetic field and the quantum dot. The whole system including electromagnetic field and the quantum state in the quantum dot is modeled by Maxwell-Bloch equations. We will investigate the steady state property under continuous wave excitation in this section. The frequency domain Maxwell-Bloch equations will be deduced to model the steady state of the quantum dot system.

3.2.1 Frequency Domain Maxwell-Bloch Equations

A quantum dot can be modeled as an open two levels system. The microscopic theory of a quantum dot with two energy levels gives a set of Maxwell-Bloch equations[42,82,83], as

$$\mu_0 \mu_r \frac{\partial}{\partial t}\mathbf{H} = -\nabla \times \mathbf{E} \tag{3.2.1}$$

$$\varepsilon_0 \varepsilon_r \frac{\partial}{\partial t}\mathbf{E} = \nabla \times \mathbf{H} - \sigma \mathbf{E} - N^{QD}\mathbf{d}_{eh}\frac{\partial p_1}{\partial t} \tag{3.2.2}$$

$$\frac{dp_1}{dt} = -\omega_{eh} p_2 - \frac{p_1}{T_2} \tag{3.2.3}$$

$$\frac{dp_2}{dt} = \omega_{eh} p_1 - \frac{p_2}{T_2} + 2\frac{\mathbf{d}_{eh} \cdot \mathbf{E}}{\hbar}\Delta \tag{3.2.4}$$

$$\frac{d\Delta}{dt} = -\frac{2\mathbf{d}_{eh} \cdot \mathbf{E}}{\hbar} p_2 - \frac{\Delta - \Delta^{pump}}{T_1} \tag{3.2.5}$$

where σ is the conductivity, N^{QD} is the spatial density of quantum dot that is modeled as a two level system, $\mathbf{d}_{eh}$ is the dipole transition matrix element, ω_{eh} is the resonant frequency of the two level system, $\hbar$ is the Planck constant, T_1 and T_2 are the longitudinal relaxation time and the transverse relaxation time of the two level system, $\rho_{12} = p_1 + ip_2$ is the microscopic polarization of the two level system (which is the off-diagonal matrix element of the density matrix between the two levels) with p_1 (p_2) being the real (imaginary) part, Δ is the population inversion, and Δ^{pump} is the steady population inversion under the pumping. When there is no pumping, $\Delta^{pump} = -1$. For continuous wave simulation, Δ^{pump} is time independent. $1/T_1$ is the relaxation rate from the excited state to the ground state; and $1/T_2$ is the rate of the relaxation of the excited state energy to the thermal background. In time domain, all of the solution is real number. For linear optics, only the Maxwell's equations (3.2.1) and (3.2.2) are needed, which are linear wave equations. Because of the linearity of the equations, a complex solution can be constructed by superposition of any two real solutions with the coefficients 1 and i. And then a Fourier transformation gives the wave equations in

frequency domain. After solving the equation in frequency domain, an inverse Fourier transformation gives a complex solution in time domain. The real part of this solution is the physical solution in time domain, because the electric and magnetic field in the physical world are real number. Now because there are nonlinear terms in the set of equation (3.2.1) to (3.2.5), there is not linearity for the solution. The solution of the Maxwell-Bloch equations (3.2.1) to (3.2.5) is a real field. A complex solution cannot be constructed because the superposition of two real solutions is not the solution of the nonlinear wave equations. Thus, the set of equations (3.2.1) to (3.2.5) cannot be directly transferred into frequency domain by Fourier transformation. However, the frequency domain version of the Maxwell-Bloch equations can be obtained after making some approximations.

At first, we can combine equation (3.2.1) and (3.2.2) into a vector Helmholtz equation of electric field. Note that the source term from the time differential includes the physical process of radiation of photon from the quantum dot as well as absorption of photons by the quantum dot. Part of p_1 is proportional to the electric field, which implicitly models the absorption of photon by the quantum dot. If we simply make the replacement of $\partial / \partial t \to -j\omega$ to transfer the source term into frequency, the photonic absorption will be lost. In order to make the modeling of the absorption explicit, we combine the Eq. (3.2.3) and (3.2.4) and insert the time differential of p_1 into the source term of (3.2.2), and we obtain a new curl equation as

$$\varepsilon_0\varepsilon_r\frac{\partial}{\partial t}\mathbf{E}=\nabla\times\mathbf{H}-\sigma\mathbf{E}+\frac{2\omega_{eh}T_2\Delta N^{QD}\left(\mathbf{d}_{eh}\mathbf{d}_{eh}\right)}{\hbar}\cdot\mathbf{E}-N^{QD}\mathbf{d}_{eh}\left(T_2\omega_{eh}\frac{\partial p_2}{\partial t}-\frac{1}{T_2}p_1-T_2{\omega_{eh}}^2p_1\right) \tag{3.2.6}$$

In this equation, the absorption of photon is modeled by the equivalent anisotropic conductivity $\sigma_{QD}=-2\omega_{eh}T_2\Delta N^{QD}\left(\mathbf{d}_{eh}\mathbf{d}_{eh}\right)/\hbar$. Note that when the quantum dot is populated in the ground state, $\Delta<0$, the positive conductivity gives absorption of the material; when the quantum dot is populated in the excited state, $\Delta>0$, the negative conductivity gives the gain coefficient. The vector Helmholtz equation is

$$\varepsilon_0\varepsilon_r\frac{\partial^2}{\partial t^2}\mathbf{E}=-\nabla\times(\mu_0\mu_r)^{-1}\nabla\times\mathbf{E}-(\sigma+\sigma_{QD})\frac{\partial}{\partial t}\mathbf{E}-N^{QD}\mathbf{d}_{eh}\left(T_2\omega_{eh}\frac{\partial^2 p_2}{\partial t^2}-\frac{1}{T_2}\frac{\partial p_1}{\partial t}-T_2{\omega_{eh}}^2\frac{\partial p_1}{\partial t}\right) \tag{3.2.7}$$

Combining equation (3.2.3) and (3.2.4) gives a second order differential equation of p_1. Thus, the set of Bloch equations becomes

$$\frac{d^2}{dt^2}p_1+\frac{2}{T_2}\frac{d}{dt}p_1+({\omega_{eh}}^2+\frac{1}{{T_2}^2})p_1=-2\frac{\mathbf{d}_{eh}\cdot\mathbf{E}}{\hbar}\omega_{eh}\Delta \tag{3.2.8}$$

$$\frac{d\Delta}{dt}=-\frac{2\mathbf{d}_{eh}\cdot\mathbf{E}}{\hbar}p_2-\frac{1}{T_1}\Delta+\frac{\Delta^{pump}}{T_1} \tag{3.2.9}$$

There is a nonlinear term, $\sigma_{QD}\frac{\partial}{\partial t}\mathbf{E}$ in Eq. (3.2.7), $2\frac{\mathbf{d}_{eh}\cdot\mathbf{E}}{\hbar}\omega_{eh}\Delta$ in Eq. (3.2.8) and $\frac{2\mathbf{d}_{eh}\cdot\mathbf{E}}{\hbar}p_2$ in Eq. (3.2.9). Thus, we cannot directly transfer these equations into complex field frequency domain equation by the replacement $\partial/\partial t\rightarrow -j\omega$. As a result, we start the analysis from the real solution in time domain.

Assuming that both electrical field and polarization field are a continuous wave with frequency ω, we can write the complex electrical field and polarization field p_1 as $\tilde{\mathbf{E}}(\mathbf{r})e^{j\omega t}$ and $\tilde{p}_1(\mathbf{r})e^{j\omega t}$. As we mentioned before, the electric field and p_1 are real variable, so they are the real part of the complex field. Thus, the time domain electrical field solution can be written as

$$\mathbf{E}(\mathbf{r},t) = \mathbf{E}_1(\mathbf{r})\cos(\omega t) + \mathbf{E}_2(\mathbf{r})\sin(\omega t) \tag{3.2.10}$$

with $\mathbf{E}_1(\mathbf{r}) = \mathrm{Re}[\tilde{\mathbf{E}}(\mathbf{r})]$ and $\mathbf{E}_2(\mathbf{r}) = -\mathrm{Im}[\tilde{\mathbf{E}}(\mathbf{r})]$; the time domain polarization field solution can be written as

$$p_1(\mathbf{r},t) = A(\mathbf{r})\sin(\omega t) + B(\mathbf{r})\cos(\omega t) \tag{3.2.11}$$

with $A(\mathbf{r}) = -\mathrm{Im}[\tilde{p}_1(\mathbf{r})]$ and $B(\mathbf{r}) = \mathrm{Re}[\tilde{p}_1(\mathbf{r})]$. If we insert the solution of $\mathbf{E}(\mathbf{r},t)$ and $p_1(\mathbf{r},t)$ into equation (3.2.9) and apply the product-to-sum trigonometric identities, we can find out that the population inversion have a constant term and a second harmonic term with double frequency. Thus, the solution of the population inversion can be written as

$$\Delta(\mathbf{r},t) = \Delta_0 + C(\mathbf{r})\sin(2\omega t) + D(\mathbf{r})\cos(2\omega t) \tag{3.2.12}$$

Inserting Eq. (3.2.10), (3.2.11) and (3.2.12) into Eq. (3.2.8) and (3.2.9), and matching the coefficients of the differential sine functions, we have a set of five equations that relate the coefficients together. For the nonlinear terms in Eq. (3.2.8) and (3.2.9), we use the product-to-sum trigonometric identity to obtain the steady state and harmonic oscillation terms.

From the nonlinear term in Eq. (3.2.8), the product-to-sum trigonometric identity gives a fundamental harmonic oscillation term as well as a third harmonic oscillation term with frequency being 3ω. Here, we argue that the third harmonic term can be neglected as an approximation. The frequency of the electromagnetic field and the polarization field is near resonant to the resonant frequency of the quantum dot, $\omega \approx \omega_{eh}$, so that the fundamental frequency driven force in the right hand side of equation (3.2.8) can produce large amplitude of $p_1(\mathbf{r},t)$. The line width of the two levels system (quantum dot) is small, compare to the frequency of the driven force. For a typical InAs/GaAs quantum dot, the parameters are $\omega_{eh} = 14.33\times10^{14}\,Hz$ and $1/T_2 = 1.25\times10^{13}\,Hz$. Thus, the third harmonic driven force is far off resonance. As a result, the third harmonic driven force can be neglected, because it generates small amplitude solution in equation (3.2.8).

We can write this set of equation in a matrix form, and the solution of this equation as:

$$\begin{bmatrix} A \\ B \\ C \\ D \\ \Delta_0 \end{bmatrix} = \begin{bmatrix} -\omega^2 + \omega_{eh}{}^2 + \frac{1}{T_2{}^2} & -\frac{2\omega}{T_2} & \hat{E}_1\omega_{eh} & -\hat{E}_2\omega_{eh} & 2\hat{E}_2\omega_{eh} \\ \frac{2\omega}{T_2} & -\omega^2 + \omega_{eh}{}^2 + \frac{1}{T_2{}^2} & \hat{E}_2\omega_{eh} & \hat{E}_1\omega_{eh} & 2\hat{E}_1\omega_{eh} \\ \hat{E}_1\frac{1}{T_2\omega_{eh}} + \hat{E}_2\frac{\omega}{\omega_{eh}} & -\hat{E}_1\frac{\omega}{\omega_{eh}} + \hat{E}_2\frac{1}{T_2\omega_{eh}} & -\frac{1}{T_1} & 2\omega & 0 \\ \hat{E}_1\frac{\omega}{\omega_{eh}} - \hat{E}_2\frac{1}{T_2\omega_{eh}} & \hat{E}_1\frac{1}{T_2\omega_{eh}} + \hat{E}_2\frac{\omega}{\omega_{eh}} & -2\omega & -\frac{1}{T_1} & 0 \\ \hat{E}_1\frac{\omega}{\omega_{eh}} + \hat{E}_2\frac{1}{T_2\omega_{eh}} & \hat{E}_1\frac{1}{T_2\omega_{eh}} - \hat{E}_2\frac{\omega}{\omega_{eh}} & 0 & 0 & -\frac{1}{T_1} \end{bmatrix}^{-1} \begin{bmatrix} 0 \\ 0 \\ 0 \\ 0 \\ -\frac{\Delta^{pump}}{T_1} \end{bmatrix}$$

(3.2.13)

where $\hat{E}_1 = \mathbf{d}_{eh} \cdot \mathbf{E}_1 / \hbar$ and $\hat{E}_2 = \mathbf{d}_{eh} \cdot \mathbf{E}_2 / \hbar$. The notation of the spatial dependence $(\mathbf{r})$ is not written into the equation (3.2.12), because equations (3.2.8) and (3.2.9) are ordinary, not partial differential equations. The solution of one spatial point does not depend on the surrounding point, but only depend on the source term of the corresponding point, which is the electrical field. Thus, we can solve equation (3.2.13) for each quantum dot separately. Note that the solution of equation (3.2.13) is a nonlinear function of the electrical field.

The numerical result from Eq. (3.2.13) shows that C and D are more than 100 times smaller than Δ_0. Thus, we can neglect the second harmonic oscillation of the population inversion in the frequency domain wave equation of the electric field. As a result, when $\Delta \approx \Delta_0$ is known, $\sigma_{QD}\frac{\partial}{\partial t}\mathbf{E}$ is a linear term in Eq. (3.2.7). Thus, we can transfer equation (3.2.7) into frequency domain as

$$\nabla \times \mu_r^{-1} \nabla \times \tilde{\mathbf{E}} - k_0^2 \tilde{\varepsilon}_r \tilde{\mathbf{E}} = -\mu_0 N^{QD} \mathbf{d}_{eh} \left[\omega^2 + j \left(\omega^3 T_2 - \frac{\omega}{T_2} - \omega_{eh}^2 \omega T_2 \right) \right] \tilde{p}_1 \quad (3.2.14)$$

where $\tilde{\varepsilon}_r = \varepsilon_r + \frac{\sigma + \sigma_{QD}}{j\omega\varepsilon_0}$ is the complex relative permittivity, $\sigma_{QD} = -2\omega_{eh} T_2 \Delta_0 N^{QD} \left(\mathbf{d}_{eh} \mathbf{d}_{eh} \right) / \hbar$ is the equivalent conductivity for the absorption rate of the quantum dot. The relation between the complex field and the real field is given in the caption of equations (3.2.10) and (3.2.11). Equations (3.2.14) and (3.2.13) should be combined and the self-consistent solution can be found by iteratively solving the two equations. We could first solve equation (3.2.14) and find out the electrical field at the quantum dot location. And then, we solve equation (3.2.13) with the solution of the electrical field, and obtain the polarization field and population inversion. Finally, we can insert the solution of the polarization field into the source term of equation (3.2.14), and obtain a new solution of the electrical field. When the new solution is close to the previous solution, the solution is convergent and the iteration terminates.

3.2.2 Numerical Result of Quantum Dot Steady State Dynamics in a Photonic Crystal Slab

We engineer a structure similar to Figure 41 of the multiple layer photonic crystal slab for the purpose of this simulation. Because we want to put the quantum dot layer in the GaAs layer, the AlAs cylinder is replaced by GaAs cylinder. Thus, the GaAs layer is a uniform layer without any hole. We have also engineered the period and diameter of the GaAs cylinder, so that one of the resonant wavelengths is near 1550 nm.

This wavelength is near resonance to the GaAs/InAs quantum dot that we are interested in. The structure is plotted in Figure 46. The period of the cylinder is 505 nm, and the diameter is 230 nm. The quantum dot layer is in the middle of the GaAs layer. The total number of GaAs layers is 5, and each GaAs layer has a quantum dot layer.

In the simulation, we assume that there are 10 quantum dots in each unit cell in each layer, and the thickness of the quantum dot layer is 10 nm, so the spatial density of the quantum dot number is $N^{QD} = 3.9 \times 10^3 \, \mu m^{-3}$. We assume the resonant wavelength of the quantum dot is 1549.1 nm, which is close to the resonant wavelength of the photonic crystal slab. The longitudinal decay time is assumed to be $T_1 = 10$ ps, and the transverse decay time is assumed to be $T_2 = 75$ fs. The spatial structure of the quantum dot is assumed to be a simple cube model. Therefore, the first excited state is a three degenerated energy level. Each quantum state has the dipole transition vector at the three spatial direction: $\mathbf{d}_{eh} = (1,0,0)$, $\mathbf{d}_{eh} = (0,1,0)$, and $\mathbf{d}_{eh} = (0,0,1)$. Each of the three degenerate states combines with the ground state to form a two level system with the corresponding dipole transition vector. They can be modeled as three independent two level systems. As a result, we will have three population inversion fields that correspond to the three dipole transition vectors. Because the incident plane wave have x direction polarization, the x direction dipole transition will be the most excited. We focus the effort to the quantum dot dynamic without external pumping, so $\Delta^{pump} = -1$.

We sweep the wavelength of the incident wave near to the resonant wavelength and calculate the steady state population inversion. The polarization of the incident plane wave electric field is along the x direction, and the amplitude of the incident electric field is $5\times10^{5}V/m$. The result is plotted in Figure 47. When the incident wavelength is off resonance, the excitation effect is weak. The electric field in the photonic crystal is mainly in the x direction, so that only the x direction dipole transition is excited with the population inversion close to -1. When the incident wavelength is near the resonant wavelength, the resonant scattering of the photonic crystal slab generates and electric field with the z and y components. As a result, all three dipole transitions are excited. In addition, the population inversion is closer to zero, which implies that there are more quantum dots on the excited state on average.

Next, we make the same simulation with a larger amplitude of the incident field. Because the main excitation is the x polarization transition of the quantum dot, we only plot out the result of the population inversion of the x polarization transition. The results in Figure 48 correspond to the amplitude of the electric field being $5\times10^{4}V/m$, $5\times10^{5}V/m$, $5\times10^{6}V/m$ and $3\times10^{7}V/m$, respectively. When the amplitude of the electric field is larger, the population inversion is further away from being -1. However, at resonant wavelength, the steady state population inversion is always smaller than zero. This implies that the positive population inversion for the two-level system is not

feasible for continuous wave excitation. In chapter five, the pulse excitation will be investigated and engineered to obtain a positive population inversion.

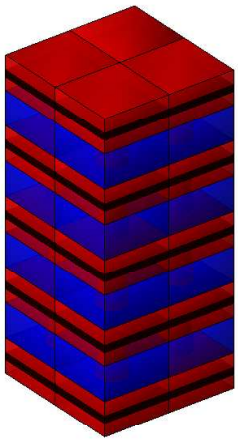

Figure 46. The spatial structure of a 5-layer GaAs/AlAs photonic crystal slab with periodic GaAs cylinders. The black layer in the middle of the GaAs layer is the quantum dot layer.

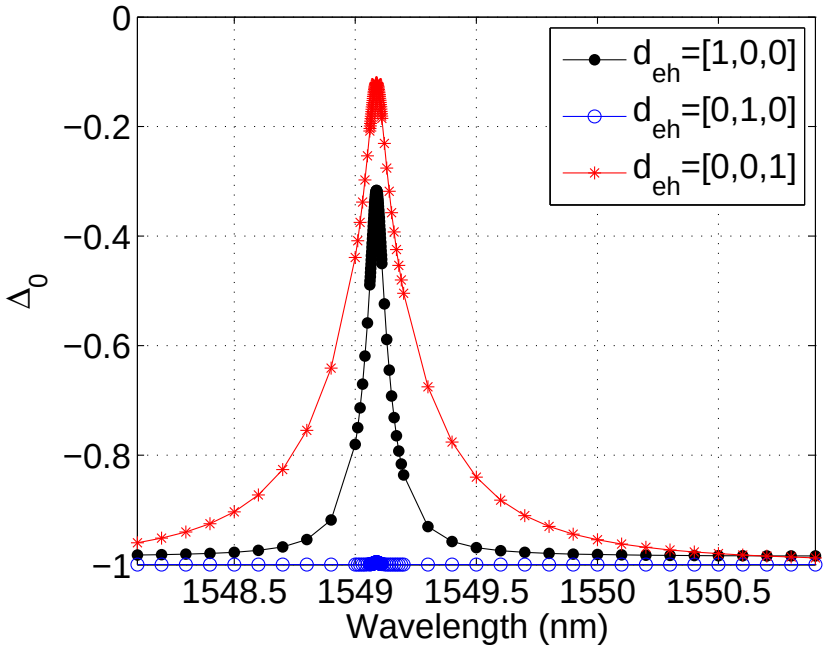

Figure 47. The average population inversion of the three direction dipole transitions of the quantum dots in Figure 46 under normal incident plane wave, versus the wavelength of the incident field.

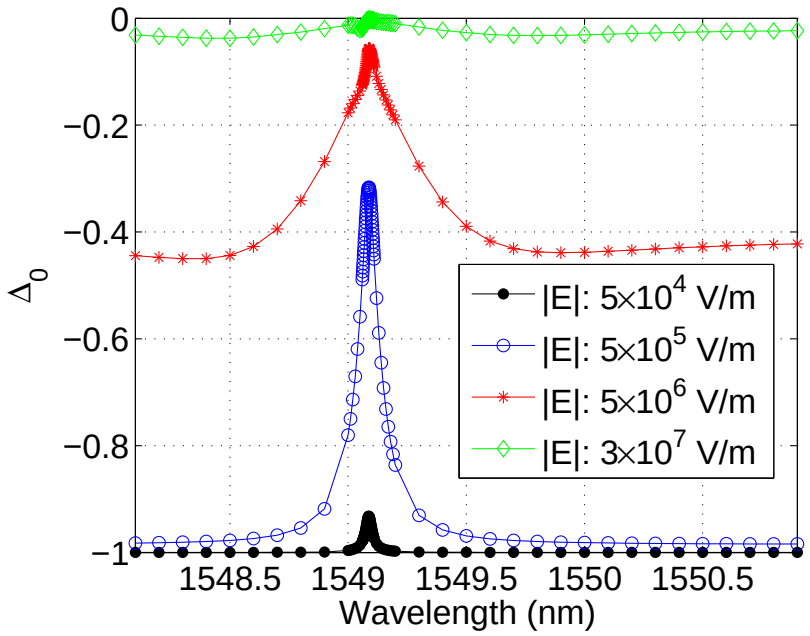

Figure 48. The steady state population inversion versus excitation wavelength at various amplitude of the incident field.

3.3 Excitation of Exciton-Polariton in Quantum Well

Exciton is a pair of electron and hole in semiconductor. Because of the Coulomb interaction between the electron and hole, the two charge particles are bound to each other. Quantum well and quantum dot can spatially trap the exciton. When the exciton is spatially trapped, the mode profile of the exciton is spatially concentrated. Thus, the interaction between the exciton and optical field could be enlarged. Coherent interaction between exciton and optical mode results in exciton polariton, which is a coupling eigenstate of exciton and optical mode. The optical mode could be either a traveling mode or a trapped mode. First principle quantum theory was introduced to calculate the coupling eigenstate of exciton polariton[91,92]. This method quantizes both excitonic field

and the optical mode, and then calculates the coupling eigenstate by diagonalization of the Hamiltonian. Some experiments have confirm the existence of the excitonic polariton[93-95]. A good approximation is semi-classical theory[96-100], which models the excitonic field by a polarization field. The quantum state and wave function of the exciton is firstly calculated. And then the non-local linear polarization is constructed as

$$4\pi\mathbf{P}_{exciton}(\mathbf{r},\omega)=\sum_{p}S_{p}(\omega)\Psi_{p}^{*}(\mathbf{r})\int_{\Omega}dV\Psi_{p}(\mathbf{r}')\mathbf{E}(\mathbf{r}',\omega) \tag{3.3.1}$$

where $\mathbf{P}_{exciton}(\mathbf{r},\omega)$ is the effective polarization field given by the excitonic field at spatial location $\mathbf{r}$ and frequency ω , $S_p(\omega)$ is the effective susceptibility, $\Psi_p(\mathbf{r})$ is the wave function of the center of mess of the exciton, and the summation goes through all of the excitonic eigenstates. $S_p(\omega)$ is defined as

$$S_{p}(\omega)=\frac{S_{0}(\omega)}{\omega_{p}-\omega-i\gamma} \tag{3.3.2}$$

where $S_0(\omega)$ is the interaction constant between the excitonic field and the optical field, ω_p is the eigenvalue of the frequency of the exciton with p being the index of the eigenstates, and γ is the recombination rate of the exciton. The non-locality originates from the quantum nature of the exciton system. The electric field at any location of the system can excite the excitonic field as long as the wave function of this exciton is nonzero. Once the exciton is excited, the whole eigenstate is radiating electromagnetic field. Wherever the wave function of the exciton is nonzero, the polarization field is

nonzero. Thus, the polarization field at one point is induced by electric field from the whole space, wherever the excitonic wave function is nonzero.

With this non-local polarization field, the wave equation of the electric field is modified to be

$$\nabla \times \mu_r^{-1} \nabla \times \mathbf{E} - k_0^2 \varepsilon_r \mathbf{E} - k_0^2 \sum_p S_p(\omega) \Psi_p^*(\mathbf{r}) \int_\Omega dV \Psi_p(\mathbf{r}') \mathbf{E}(\mathbf{r}', \omega) = 0 \tag{3.3.3}$$

The weak form of this wave equation is the same as equations (2.2.16) and (2.2.17), or the matrix form of the weak form (3.1.1), except that the mass matrix is modified. The new mass matrix is defined as

$$M_{m,n} = \int_\Omega d\mathbf{r} \mathbf{\Phi}_m(\mathbf{r}) \cdot \varepsilon_r \cdot \mathbf{\Phi}_n(\mathbf{r}) + \sum_p S_p(\omega) \int_\Omega d\mathbf{r} \mathbf{\Phi}_m(\mathbf{r}) \cdot \Psi_p^*(\mathbf{r}) \int_\Omega d\mathbf{r}' \Psi_p(\mathbf{r}') \mathbf{\Phi}_n(\mathbf{r}') \tag{3.3.4}$$

Defining a column vector for the excitonic field with the vector element being $\left(\mathbf{\Psi}_p\right)_m = \int_\Omega d\mathbf{r} \mathbf{\Phi}_m(\mathbf{r}) \Psi_p^*(\mathbf{r})$, the mass matrix can be written as

$$\mathbf{M} = \mathbf{M}_d + \sum_p S_p(\omega) \mathbf{\Psi}_p \left(\mathbf{\Psi}_p\right)^+ \tag{3.3.5}$$

where $\left(\mathbf{M}_d\right)_{m,n} = \int_\Omega d\mathbf{r} \mathbf{\Phi}_m(\mathbf{r}) \cdot \varepsilon_r \cdot \mathbf{\Phi}_n(\mathbf{r})$ is the dielectric part of the mass matrix, $\left(\mathbf{\Psi}_p\right)^+$ is the Hermitian conjugate (transpose and conjugate) to $\mathbf{\Psi}_p$.

The coupling system between surface plasmon polariton and exciton is interesting because of the strong coupling[101]. The surface plasmon polariton is a highly localized optical state, which enhances the coupling strength with the exciton. One of the surface plasmon-exciton coupling systems is investigated by this semi-classical theory.

The configuration of this system is plotted in Figure 49. The background medium above the system is air. The thicknesses of each layer from the top are 35 nm for the silver film; 33 nm for the $Al_{0.3}Ga_{0.7}As$ as the barrier of the quantum well; 10 nm for the $GaAs$ as the quantum well; 33 nm for the $Al_{0.3}Ga_{0.7}As$ as the other barrier; 33 nm for the second silver film. The substrate is an infinitely thick $GaAs$. The surface plasmon polariton system consists of two silver films. The top film has periodic air holes, which provide additional parallel momentum to the incident plane wave from the air. The period of the square lattice air holes is 210 nm, and the radius of the air holes is 55 nm. The incident plane wave excites the surface plasmon polariton in both metallic thin films. In between the two silver films, a three layer semi-conductor constructs a quantum well. The exciton is trapped inside the quantum well. Because the amplitude of the excitonic wave function is small in the quantum barrier area, the non-local susceptibility is nonzero only in the quantum well area. This quantum well has two confined modes for electron, three confined modes for heavy hole, and two confined modes for light hole. Because of the symmetric matching, only two pairs of electron-hole give exciton that strongly couple to the optical field. The heavy hole exciton is the coupling between ground state electron and ground state heavy hole, with energy level 1.546 eV corresponding to wavelength 802 nm. The light hole exciton is the coupling between ground state electron and ground state light hole, with energy level 1.554 eV corresponding to wavelength 798 nm. In the

numerical simulation, only these two excitons are considered in the summation of equations (3.3.3) through (3.3.5).

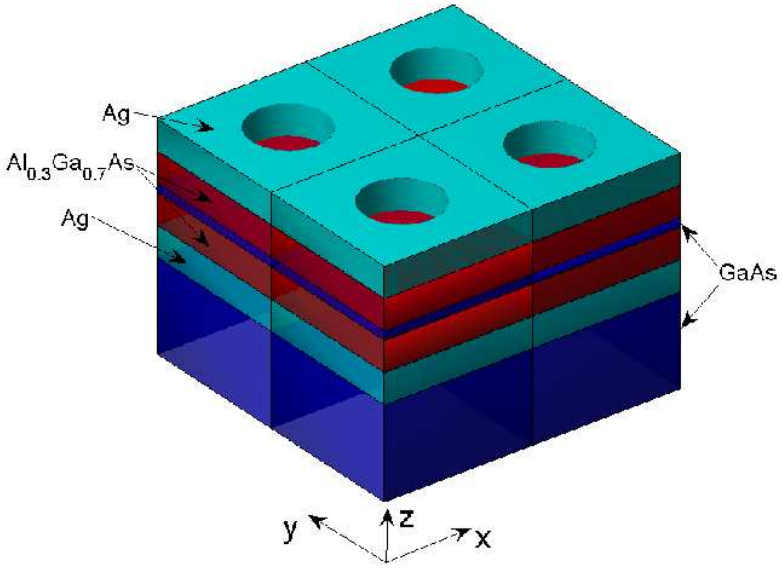

Figure 49. The spatial structure of two-by-two periods of the surface plasmon polariton-exciton coupling system. The background medium above the system is air. The film in cyan is silver; the film in red is $Al_{0.3}Ga_{0.7}As$, which is the barrier of the quantum well; the film in blue is $GaAs$, which is the quantum well and substrate.

The numerical result of the transmission rate is calculated by the SEM. At first, the transmission rate of the system without the quantum well is calculated and plotted in Figure 50. In this simulation, the quantum well area is filled with $Al_{0.3}Ga_{0.7}As$, so that there is no exciton in this area. The incident wave only excites the surface plasmon polariton. A resonant excitation of the surface plasmon polariton is observed with the central wavelength near 800 nm. When the quantum well is present, the calculated transmission rate is plotted in Figure 51. The transmission rate decreases near to the resonant wavelengths of the two excitons. Thus, the excitation of exciton is identified

from the transmission rate. Further investigate will observe the modification of the electromagnetic field under the present of excitons.

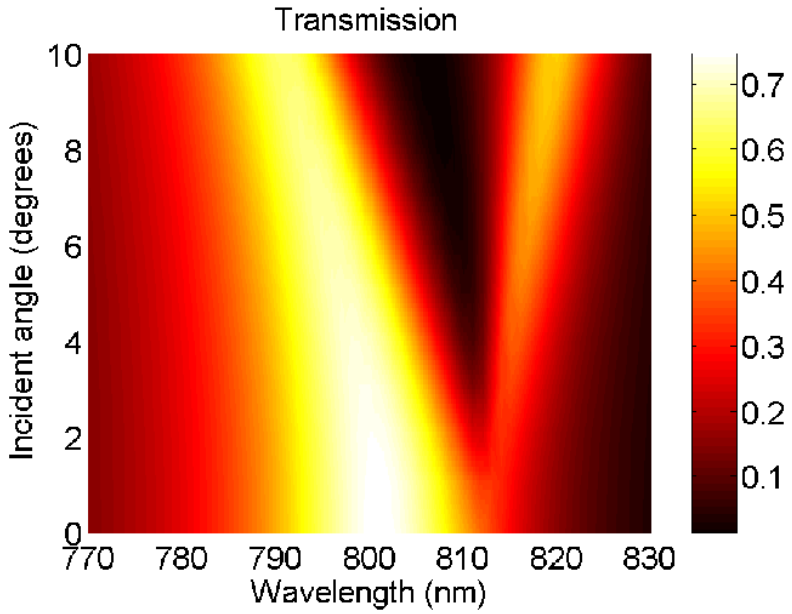

Figure 50. The transmission rate versus the incident angle and wavelength. The simulated system is shown in Figure 49with the quantum well being removed. The quantum well area is filled with $Al_{0.3}Ga_{0.7}As$, so that there is no excitonic effect in this system. The incident direction is on the x-z plane; the polarization is on the x-z plane.

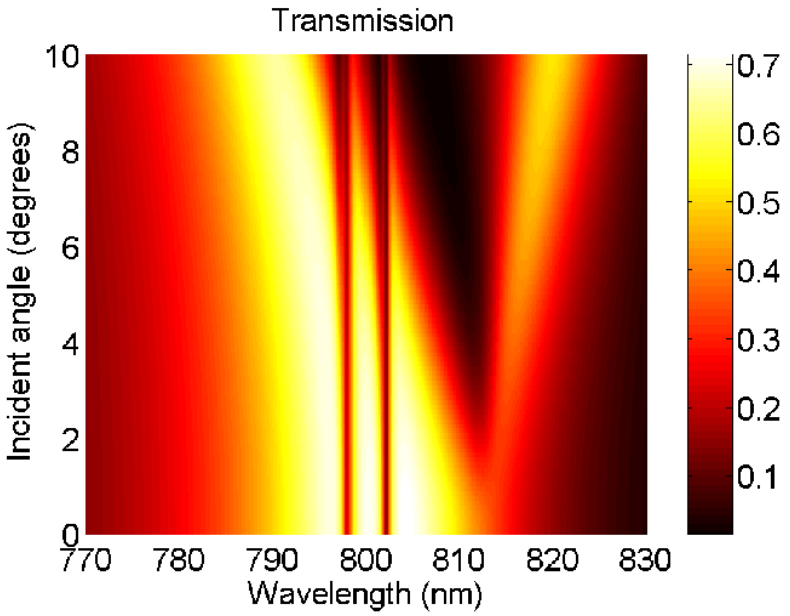

Figure 51. The transmission rate of the system shown in Figure 49. The incident direction is on the x-z plane; the polarization is on the x-z plane. The excitonic effect concentrates at the two resonant wavelength of the quantum well, 802 nm for the heavy hole exciton and 798 nm for the light hole exciton.

Chapter Four. Spectral Element Time Domain Simulation for Linear Optics

Another useful simulation tool for electromagnetic field is in time domain. If the simulated field is an electromagnetic pulse or an optical pulse, the time domain simulation can directly give the solution of the time evolution of the field. One of the most widely used methods is the finite difference time domain (FDTD) method. FDTD is efficient and accurate for simulation of simple structure. However, when the simulated structure becomes more complicated with curve surface, the accuracy of the FDTD method decreases. Thus, the FDTD method is not efficient for complex structures. The finite element method is powerful for the modeling of complex structures, because of the flexibility of the mesh. In addition, the electromagnetic field is interpolated by a piecewise continue function, which theoretically gain more accuracy than finite difference approximation. The finite element time domain (FETD) method of electromagnetic simulation[15] has been investigated for years. Recently, the spectral element method is extended to time domain simulation[24]. The spectral element time domain (SETD) method can obtain high accuracy and efficiency. In this chapter, the SETD is overviewed. An implementation of the SETD in structure mesh is inspected by numerical examples of the woodpile photonic crystal structure.

4.1 Overview of Spectral Element Time Domain

The spectral element time domain method is based on the Maxwell's curl equations and the finite element discretization process. For the convenience of numerical implementation, the Maxwell's curl equations are normalized. We introduce the normalized electric field as $\mathbf{E}^{nor} = \mathbf{E}/\sqrt{\mu_0}$, and the normalized magnetic field as $\mathbf{H}^{nor} = \mathbf{H}/\sqrt{\varepsilon_0}$. In addition, the perfectly match layer (PML) is considered into the Maxwell's equations. The PML is impedance matched with the background medium, so that the scattered field from the simulated object enters the PML region with little reflection. Meanwhile, the PML can be made a highly attenuating medium that efficiently absorbs the field inside the PML region. As a result, the scattered field from the simulated object will enter the PML region and be almost completely absorbed. Effectively, the PML simulates the scattering of the electromagnetic field by an object in an infinitely large background medium. Thus, we have

$$\varepsilon_r \frac{\partial}{\partial t}\tilde{\mathbf{E}} = c_0 \nabla \times \tilde{\mathbf{H}} - \frac{\mathbf{J}}{\varepsilon_0\sqrt{\mu_0}} - \left(\frac{\sigma}{\varepsilon_0} + \varepsilon_r \Lambda_1\right)\tilde{\tilde{\mathbf{E}}} - \left(\frac{\sigma}{\varepsilon_0}\Lambda_1 + \varepsilon_r \Lambda_2\right)\mathbf{E}^{(1)} - \frac{\sigma}{\varepsilon_0}\Lambda_3 \mathbf{E}^{(2)} \tag{4.1}$$

$$\mu_r \frac{\partial}{\partial t}\tilde{\mathbf{H}} = -c_0 \nabla \times \tilde{\tilde{\mathbf{E}}} - \mu_r \Lambda_1 \tilde{\mathbf{H}} - \mu_r \Lambda_2 \mathbf{H}^{(1)} \tag{4.2}$$

where $\tilde{\tilde{\mathbf{E}}} = \mathbf{E}^{nor} + \overline{\omega}\mathbf{E}^{(1)}$, $\tilde{\mathbf{H}} = \mathbf{H}^{nor} + \overline{\omega}\mathbf{H}^{(1)}$, $\overline{\omega} = diag\{\omega_x, \omega_y, \omega_z\}$,

$\Lambda_1 = diag\{\omega_y + \omega_z - \omega_x, \omega_x + \omega_z - \omega_y, \omega_x + \omega_y - \omega_z\}$,

$\Lambda_2 = diag\{(\omega_x - \omega_y)(\omega_x - \omega_z), (\omega_y - \omega_x)(\omega_y - \omega_z), (\omega_z - \omega_x)(\omega_z - \omega_y)\}$,

$\Lambda_3 = diag\{\omega_y\omega_z, \omega_x\omega_z, \omega_x\omega_y\}$, and ω_x, ω_y, ω_z are the PML attenuation coefficients. The mesh of the PML region and the distribution of the PML attenuation coefficients are shown in Figure 52. With this set of the PML coefficients, the scattered field from the physical region enters the PML region with small reflection. The well posed PML scheme gives the equations for the auxiliary field $\mathbf{E}^{(1)}$, $\mathbf{E}^{(2)}$ and $\mathbf{H}^{(1)}$ as,

$$\frac{\partial \mathbf{E}^{(1)}}{\partial t} = \tilde{\mathbf{E}} - \overline{\omega}\mathbf{E}^{(1)} \tag{4.3}$$

$$\frac{\partial \mathbf{E}^{(2)}}{\partial t} = \mathbf{E}^{(1)} \tag{4.4}$$

$$\frac{\partial \mathbf{H}^{(1)}}{\partial t} = \tilde{\mathbf{H}} - \overline{\omega}\mathbf{H}^{(1)} \tag{4.5}$$

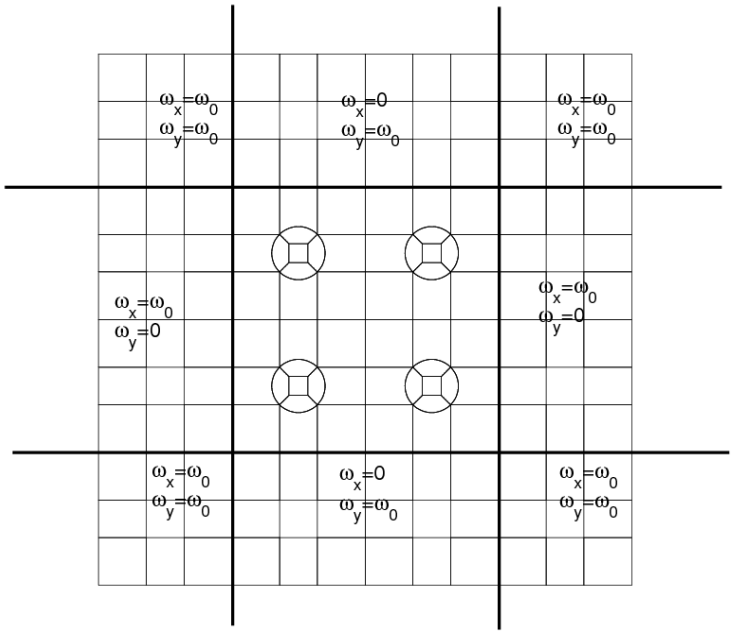

Figure 52. The mesh of the PML region and the distribution of the PML attenuation coefficients. The physical region is in the middle and the PML attenuation coefficients in the physical region are all zero.

In order to discretize equations (4.1) to (4.5), the fields are interpolated by the mixed order basis functions defined in (2.1.6) and (2.1.7). Study shows that mixed order basis functions for each field as well as mixed orders between electric and magnetic field prevent spurious modes. Thus, the electric field is interpolated by the N-th order basis functions, and the magnetic field is interpolated by the (N-1)-th order basis functions. The interpolation can be written as

$$\tilde{\mathbf{E}} = \sum_{n=1}^{N_t^e} E_n \boldsymbol{\Phi}_n \tag{4.6}$$

$$\tilde{\mathbf{H}} = \sum_{n=1}^{N_t^h} H_n \boldsymbol{\Psi}_n \tag{4.7}$$

where $\boldsymbol{\Phi}_n$ and $\boldsymbol{\Psi}_n$ are the N-th and (N-1)-th order basis functions, E_n and H_n are the interpolated electric and magnetic field at the nodal points, N_t^e and N_t^h are the number of basis functions for electric field and magnetic field. The auxiliary field $\mathbf{E}^{(1)}$, $\mathbf{E}^{(2)}$ and $\mathbf{H}^{(1)}$ are interpolated by the same kind of basis functions. By applying the Galerkin's method to test equations (4.1) and (4.2), we have the weak form of these two equations as

$$\begin{aligned}\frac{\partial}{\partial t}\int_\Omega \boldsymbol{\Phi}_m \cdot \varepsilon_r \cdot \tilde{\mathbf{E}} dV &= c_0 \int_\Omega (\nabla \times \boldsymbol{\Phi}_m) \cdot \tilde{\mathbf{H}} dV + c_0 \int_{\partial\Omega} \boldsymbol{\Phi}_m \cdot (\hat{n} \times \tilde{\mathbf{H}}) dS - \frac{1}{\varepsilon_0 \sqrt{\mu_0}} \int_\Omega \boldsymbol{\Phi}_m \cdot \mathbf{J} dV \\ &- \int_\Omega \boldsymbol{\Phi}_m \cdot \left(\frac{\sigma}{\varepsilon_0} + \varepsilon_r \Lambda_1 \right) \tilde{\mathbf{E}} dV - \int_\Omega \boldsymbol{\Phi}_m \cdot \left(\frac{\sigma}{\varepsilon_0} \Lambda_1 + \varepsilon_r \Lambda_2 \right) \mathbf{E}^{(1)} dV - \int_\Omega \boldsymbol{\Phi}_m \cdot \frac{\sigma}{\varepsilon_0} \Lambda_3 \mathbf{E}^{(2)} dV\end{aligned} \tag{4.8}$$

$$\frac{\partial}{\partial t}\int_{\Omega}\boldsymbol{\Psi}_m\cdot\mu_r\cdot\tilde{\mathbf{H}}dV=-c_0\int_{\Omega}(\nabla\times\boldsymbol{\Psi}_m)\cdot\tilde{\mathbf{E}}dV-c_0\int_{\partial\Omega}\boldsymbol{\Psi}_m\cdot(\hat{n}\times\tilde{\mathbf{E}})dS$$
$$-\int_{\Omega}\boldsymbol{\Psi}_m\cdot\mu_r\Lambda_1\tilde{\mathbf{H}}dV-\int_{\Omega}\boldsymbol{\Psi}_m\cdot\mu_r\Lambda_2\mathbf{H}^{(1)}dV \tag{4.9}$$

The boundary outside of the PML region is both perfect electric and magnetic conductor (PEC and PMC), so that the surface integral is zero. Inserting the interpolation of the electric and magnetic fields into the weak form (4.8) and (4.9), we obtain two matrix equations that couple to each other by the stiffness matrixes

$$\frac{d\mathbf{e}}{dt}=\mathbf{M}_{ee}^{-1}[\mathbf{S}_{eh}\mathbf{h}+\mathbf{K}\mathbf{e}+\mathbf{q}-\mathbf{M}_{e0}\mathbf{e}-\mathbf{M}_{e1}\mathbf{e}^{(1)}-\mathbf{M}_{e2}\mathbf{e}^{(2)}] \tag{4.10}$$

$$\frac{d\mathbf{h}}{dt}=\mathbf{M}_{hh}^{-1}[\mathbf{S}_{he}\mathbf{e}-\mathbf{M}_{h0}\mathbf{h}-\mathbf{M}_{h1}\mathbf{h}^{(1)}] \tag{4.11}$$

where the mass matrixes are

$$(\mathbf{M}_{ee})_{mn}=\int_{\Omega}\boldsymbol{\Phi}_m\cdot\varepsilon_r\cdot\boldsymbol{\Phi}_n dV \tag{4.12}$$

$$(\mathbf{M}_{hh})_{mn}=\int_{\Omega}\boldsymbol{\Psi}_m\cdot\mu_r\cdot\boldsymbol{\Psi}_n dV \tag{4.13}$$

and the stiffness matrixes are

$$(\mathbf{S}_{eh})_{mn}=c_0\int_{\Omega}(\nabla\times\boldsymbol{\Phi}_m)\cdot\boldsymbol{\Psi}_n dV \tag{4.14}$$

$$(\mathbf{S}_{eh})_{mn}=-c_0\int_{\Omega}(\nabla\times\boldsymbol{\Psi}_m)\cdot\boldsymbol{\Phi}_n dV \tag{4.15}$$

and the conductivity matrix is

$$(\mathbf{K})_{mn}=-\int_{\Omega}\boldsymbol{\Phi}_m\cdot\frac{\sigma}{\varepsilon_0}\cdot\boldsymbol{\Phi}_n dV \tag{4.16}$$

$\mathbf{e}$ and $\mathbf{h}$ are the unknowns vector of the electric field and the magnetic field, and $\mathbf{e}^{(1)}$, $\mathbf{e}^{(2)}$, $\mathbf{h}^{(1)}$ are the unknowns vector of the auxiliary fields. $\mathbf{q}$ is the source vector. The mass matrixes associated to the PML is similarly defined as (4.12) and (4.13), with different coefficients, as

$$\left(\mathbf{M}_{e0}\right)_{mn} = \int_{\Omega} \mathbf{\Phi}_m \cdot \Lambda_1 \cdot \mathbf{\Phi}_n dV \tag{4.17}$$

$$\left(\mathbf{M}_{e1}\right)_{mn} = \int_{\Omega} \mathbf{\Phi}_m \cdot (\frac{\sigma}{\varepsilon}\Lambda_1 + \Lambda_2) \cdot \mathbf{\Phi}_n dV \tag{4.18}$$

$$\left(\mathbf{M}_{e2}\right)_{mn} = \int_{\Omega} \mathbf{\Phi}_m \cdot \left(\frac{\sigma}{\varepsilon}\Lambda_3\right) \cdot \mathbf{\Phi}_n dV \tag{4.19}$$

$$\left(\mathbf{M}_{h0}\right)_{mn} = \int_{\Omega} \mathbf{\Psi}_m \cdot \Lambda_1 \cdot \mathbf{\Psi}_n dV \tag{4.20}$$

$$\left(\mathbf{M}_{h1}\right)_{mn} = \int_{\Omega} \mathbf{\Psi}_m \cdot \Lambda_2 \cdot \mathbf{\Psi}_n dV \tag{4.20}$$

Making use of the covariant mapping formulas from equations (2.1.6) and (2.1.7), the integrals (4.12) to (4.15) can be calculated in the reference domain. Thus, the integrals are written as

$$\left(\mathbf{M}_{ee}\right)_{mn} = \int_{\Omega} \left(\mathbf{J}^{-1}\tilde{\mathbf{\Phi}}_m\right) \cdot \varepsilon_r \cdot \left(\mathbf{J}^{-1}\tilde{\mathbf{\Phi}}_n\right) |\mathbf{J}| d\xi d\eta d\zeta \tag{4.21}$$

$$\left(\mathbf{M}_{hh}\right)_{mn} = \int_{\Omega} \left(\mathbf{J}^{-1}\tilde{\mathbf{\Psi}}_m\right) \cdot \varepsilon_r \cdot \left(\mathbf{J}^{-1}\tilde{\mathbf{\Psi}}_n\right) |\mathbf{J}| d\xi d\eta d\zeta \tag{4.22}$$

$$\left(\mathbf{S}_{eh}\right)_{mn} = c_0 \int_{\Omega} \frac{1}{|\mathbf{J}|} \left[\mathbf{J}^T (\nabla \times \tilde{\mathbf{\Phi}}_m)\right] \cdot \left(\mathbf{J}^{-1}\tilde{\mathbf{\Psi}}_n\right) |\mathbf{J}| d\xi d\eta d\zeta = c_0 \int_{\Omega} (\nabla \times \tilde{\mathbf{\Phi}}_m) \cdot \left(\tilde{\mathbf{\Psi}}_n\right) d\xi d\eta d\zeta \tag{4.23}$$

$$\left(\mathbf{S}_{eh}\right)_{mn} = -c_0 \int_{\Omega} (\nabla \times \tilde{\boldsymbol{\Psi}}_m) \cdot \tilde{\boldsymbol{\Phi}}_n d\xi d\eta d\zeta \tag{4.24}$$

The stiffness matrixes are independent of the Jacobian matrix, which means that the stiffness matrixes are independent of the shape of the element. Thus, only the elemental stiffness matrixes are stored, and the matrix-vector multiplication between the stiffness matrixes and the field vectors can be calculated element by element. The stiffness matrixes of the whole system are not stored, and then the implementation of the method can save this part of the memory cost. With the same procedure, the weak form of the equation (4.3), (4.4) and (4.5) can be written as matrix equations as

$$\frac{\partial \mathbf{e}^{(1)}}{\partial t} = \tilde{\mathbf{e}} - \overline{\omega}\mathbf{e}^{(1)} \tag{4.25}$$

$$\frac{\partial \mathbf{e}^{(2)}}{\partial t} = \mathbf{e}^{(1)} \tag{4.26}$$

$$\frac{\partial \mathbf{h}^{(1)}}{\partial t} = \tilde{\mathbf{h}} - \overline{\omega}\mathbf{h}^{(1)} \tag{4.27}$$

Because the mesh in the PML region is always orthogonal, the mass matrixes of the physical field and the auxiliary field are identical. Thus, the mass matrixes at the left and right hand sides of the equations cancel each other, and then the matrix equation only contains the diagonal terms. The matrix equations (4.10) and (4.11), together with the matrix equations (4.25), (4.26), (4.27) can be solved by the fourth order Runge-Kutta method. In order to reduce the CPU time of the time integral, the decomposition of the

mass matrixes $\mathbf{M}_{ee}$ and $\mathbf{M}_{hh}$ are pre-calculated and stored. At each time step, the linear problem in equation (4.10) and (4.11) are solved by using the decomposition.

If there are only orthogonal elements throughout the whole system, the mass matrixes $\mathbf{M}_{ee}$ and $\mathbf{M}_{hh}$ became diagonal by using the GLL approximation in the evaluation of the integrals (4.21) and (4.22). The integrals in the reference domain are evaluated by the GLL integral, which is a Gaussian integral with sampling point given by the nodal point of the GLL polynomials. An N-th order GLL integral gives exact value of the integral of any $(2N-1)$-th order polynomials. For example, the integral in equation (4.16) consists of three one dimensional integrals given that the element is orthogonal. If the test and basis functions have different directions, the integrand is zero. When the direction of the test and basis functions is the same, for the N-th order basis function, the integrand in each dimension is (2N-2)-th or 2N-th order polynomials. If the (N+1)-th order GLL integral is used for the 2N-th order polynomials, and N-th order GLL integral is used for the (2N-2)-th order polynomials, the integral is exact. This integral gives nonzero non-diagonal terms in the mass matrix. As an approximation, if the N-th order GLL integral is used for the 2N-th order polynomials, and (N-1)-th order GLL integral is used for the (2N-2)-th order polynomials, the integral is not exact. In this case, the sampling points of the GLL integral are the same as the nodal points, so that the integral is nonzero only when the nodal point of the test and basis functions overlaps, or when the test and basis functions are the same. Thus, the mass matrix is

diagonal. Numerical result shows that this approximation keeps the accuracy of the method. Meanwhile, this approximation greatly improves the efficiency. Because the mass matrixes are diagonal, the inverse of the mass matrixes is simply the inverse of each diagonal element. As a result, the time integration costs much less CPU time.

If the size of the simulated system is much larger than the wavelength, and there are non-orthogonal elements in the physical domain, the number of unknowns become large, and the decomposition of the large mass matrixes become unavailable for limited computational resource. Similar to the solution for the frequency domain solver, a domain decomposition method (DDM)[84,85] is introduced for the time domain solver. The foundation of the DDM is also the Riemann solver (2.4.3) and (2.4.4). At first, the whole system is split into $N^{(D)}$ subdomains, as shown in Figure 53. On the interface between two subdomains, e.g. subdomain (i) and subdomain (j), the Riemann solver is used to model the transmission of the electromagnetic field from one subdomain to the other. The weak form (4.8) and (4.9) apply to each subdomain, and the surface integrals are on the interface. Inserting the magnetic field Riemann solver (2.4.4) into the surface integral of the weak form (4.8), and the electric field Riemann solver (2.4.3) into the surface integral of the weak form (4.9), we obtain the weak form of each subdomain. The matrix equations for the subdomain (i) is obtained as

$$\frac{d\mathbf{e}^{(i)}}{dt} = \mathbf{M}_{ee}{}^{-1}[(\mathbf{S}_{eh} + \mathbf{R}_1)\mathbf{h}^{(i)} + (\mathbf{K} + \mathbf{R}_2)\mathbf{e}^{(i)} + \mathbf{T}_1\mathbf{h}^{(j)} + \mathbf{T}_2\mathbf{e}^{(j)} + \mathbf{q} - \mathbf{M}_{e0}\mathbf{e} - \mathbf{M}_{e1}\mathbf{e}^{(1)} - \mathbf{M}_{e2}\mathbf{e}^{(2)}] \tag{4.28}$$

$$\frac{d\mathbf{h}^{(i)}}{dt} = \mathbf{M}_{hh}^{-1}[(\mathbf{S}_{he} + \mathbf{R}_3)\mathbf{e}^{(i)} + \mathbf{R}_4\mathbf{h}^{(i)} + \mathbf{T}_3\mathbf{e}^{(j)} + \mathbf{T}_4\mathbf{h}^{(j)} - \mathbf{M}_{h0}\mathbf{h} - \mathbf{M}_{h1}\mathbf{h}^{(1)}] \tag{4.29}$$

where $\mathbf{e}^{(i)}$ and $\mathbf{h}^{(i)}$ are the electric and magnetic fields' unknown vectors of the subdomain (i), $\mathbf{e}^{(j)}$ and $\mathbf{h}^{(j)}$ are the electric and magnetic fields' unknown vectors of the neighboring subdomain (j), the matrixes $\mathbf{R}_1, \mathbf{R}_2, \mathbf{R}_3, \mathbf{R}_4, \mathbf{T}_1, \mathbf{T}_2, \mathbf{T}_3, \mathbf{T}_4$ are Riemann solver matrixes defined as

$$(\mathbf{R}_1)_{mn} = c_0 \oint_{\partial\Omega} \left(\frac{Z^{(i)}}{Z^{(i)} + Z^{(j)}} \mathbf{\Phi}_m \cdot \hat{n} \times \mathbf{\Psi}_n \right) dS \tag{4.30}$$

$$(\mathbf{R}_2)_{mn} = -c_0 \oint_{\partial\Omega} \left(\frac{Z_0}{Z^{(i)} + Z^{(j)}} \hat{n} \times \mathbf{\Phi}_m \cdot \hat{n} \times \mathbf{\Phi}_n \right) dS \tag{4.31}$$

$$(\mathbf{R}_3)_{mn} = -c_0 \oint_{\partial\Omega} \left(\frac{Y^{(i)}}{Y^{(i)} + Y^{(j)}} \mathbf{\Psi}_m \cdot \hat{n} \times \mathbf{\Phi}_n \right) dS \tag{4.32}$$

$$(\mathbf{R}_4)_{mn} = -c_0 \oint_{\partial\Omega} \left(\frac{Y_0}{Y^{(i)} + Y^{(j)}} \hat{n} \times \mathbf{\Psi}_m \cdot \hat{n} \times \mathbf{\Psi}_n \right) dS \tag{4.33}$$

$$(\mathbf{T}_1)_{mn} = c_0 \oint_{\partial\Omega} \left(\frac{Z^{(i)}}{Z^{(i)} + Z^{(j)}} \mathbf{\Phi}_m^{(i)} \cdot \hat{n} \times \mathbf{\Psi}_n^{(j)} \right) dS \tag{4.34}$$

$$(\mathbf{T}_2)_{mn} = c_0 \oint_{\partial\Omega} \left(\frac{Z_0}{Z^{(i)} + Z^{(j)}} \hat{n} \times \mathbf{\Phi}_m^{(i)} \cdot \hat{n} \times \mathbf{\Phi}_n^{(j)} \right) dS \tag{4.35}$$

$$(\mathbf{T}_3)_{mn} = -c_0 \oint_{\partial\Omega} \left(\frac{Y^{(i)}}{Y^{(i)} + Y^{(j)}} \mathbf{\Psi}_m^{(i)} \cdot \hat{n} \times \mathbf{\Phi}_n^{(j)} \right) dS \tag{4.36}$$

$$(\mathbf{T}_4)_{mn} = c_0 \oint_{\partial\Omega} \left(\frac{Y_0}{Y^{(i)} + Y^{(j)}} \hat{n} \times \mathbf{\Psi}_m^{(i)} \cdot \hat{n} \times \mathbf{\Psi}_n^{(j)} \right) dS \tag{4.37}$$

where the superscript (i) and (j) refer to the subdomain (i) and subdomain (j) with subdomain (j) being the neighbor subdomain of the subdomain (i), $\hat{n}$ is the normal unit vector on the interface pointing from subdomain (i) to subdomain (j). $Z^{(i)}$, $Z^{(j)}$ are the impedance distribution of the subdomain (i) and (j), and $Y^{(i)}$, $Y^{(j)}$ are the admittance distribution of the subdomain (i) and (j). $Y_0 = 1/Z_0$ is the admittance in vacuum. For each subdomain, the electric and magnetic field evolution is described by equations (4.28) and (4.29), and the correction from the neighboring subdomain is described by the $\mathbf{T}$ matrixes in these two equations. The auxiliary fields for the PML layer are local variants that do not transmit to the adjacent domain, so that these fields are not influenced by the electromagnetic field from the neighboring domain. For each subdomain, the number of unknowns is small, so the decompositions of the mass matrixes are available. For a finite periodic structure, many subdomains have the same structure that gives the same mass matrixes, so only one decomposition of these repeating mass matrixes need to be stored. The whole system is modeled by the assembling of the $N^{(D)}$ sets of equation (4.28) and (4.29) for the $N^{(D)}$ domains.

The fourth order Runge-Kutta method can be used to explicitly integrate the time evolution of the electromagnetic field. In order to ensure the stability of the time integral, the time step needs to be small enough. The maximum limit time step is determined by the eigenvalue of the numerical discretization matrix. As an approximation, the maximum limit time step is close to the time period that the

electromagnetic field travels from one nodal point to the adjacent nodal point. As a result, the time step needs to satisfy $\Delta t \le \min\left\{h_{\min}[\xi_2^{(N)} - \xi_1^{(N)}]\sqrt{\varepsilon_r \mu_r}\,/2c\right\}$, where N is the order of the electric field basis function, $\xi_j^{(N)}$ is the j-th nodal point in the reference domain, $h_{\min}$ is the minimum length of the edges of the element. Another method to integrate the matrix equation is implicit Runge-Kutta method. This method is unconditional stable. For electrically small structure, the time step limit of explicit method would be much smaller than the time step limit for the accuracy requirement of time integration; while the implicit method can directly take the time step limit for the accuracy requirement of time integration. Thus, the implicit method is preferred for simulation with electrically small structure. For linear optical problem with electrically large structure, the explicit method is preferred because the time step limit for the stability condition is close to the time step limit for the accuracy requirement of time integration. For nonlinear optical problem, the explicit method is preferred. When nonlinear terms appear in the equation, the implicit solver needs to solve the equation iteratively at each time step. In contrast, the explicit solver can directly integrate the equations.

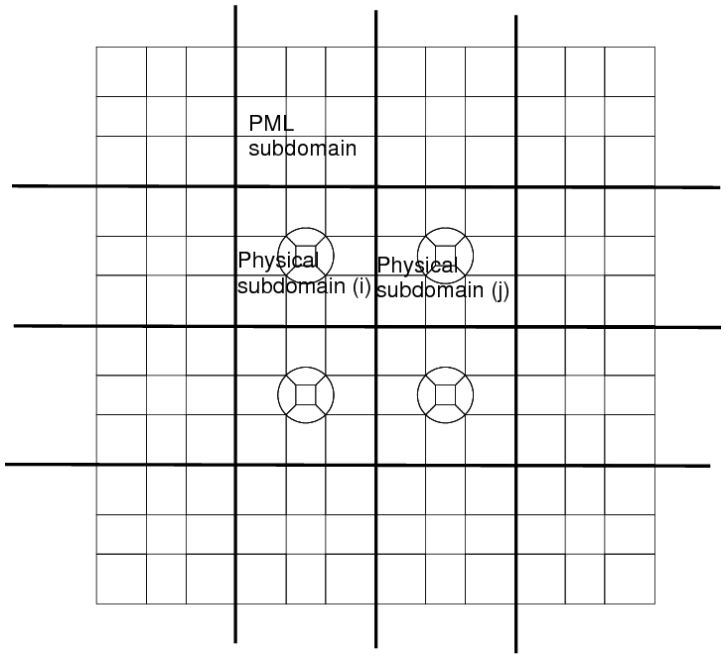

Figure 53. Division of the simulated system into physical and PML subdomain.

4.2 Application to Photonic Crystal Waveguide and Micro-Cavity

The spectral element method was applied to simulate waveguide and micro-cavity consisting of defect in the woodpile photonic crystal. The simulated system is shown in Figure 54. In the woodpile photonic crystal, the width and height of the rod is w=0.3a and h=0.3a, respectively, with 'a' being the periods at the horizontal directions. In Figure 54 (a), the width of the rod in the middle is increased to be 0.7a, which is a line defect. This line defect constructs a waveguide mode. In Figure 54 (b), a point defect is constructed by stretching the middle period of whole dielectric structure along the direction of the waveguide for 1.067 times [34]. This point defect constructs a micro-cavity.

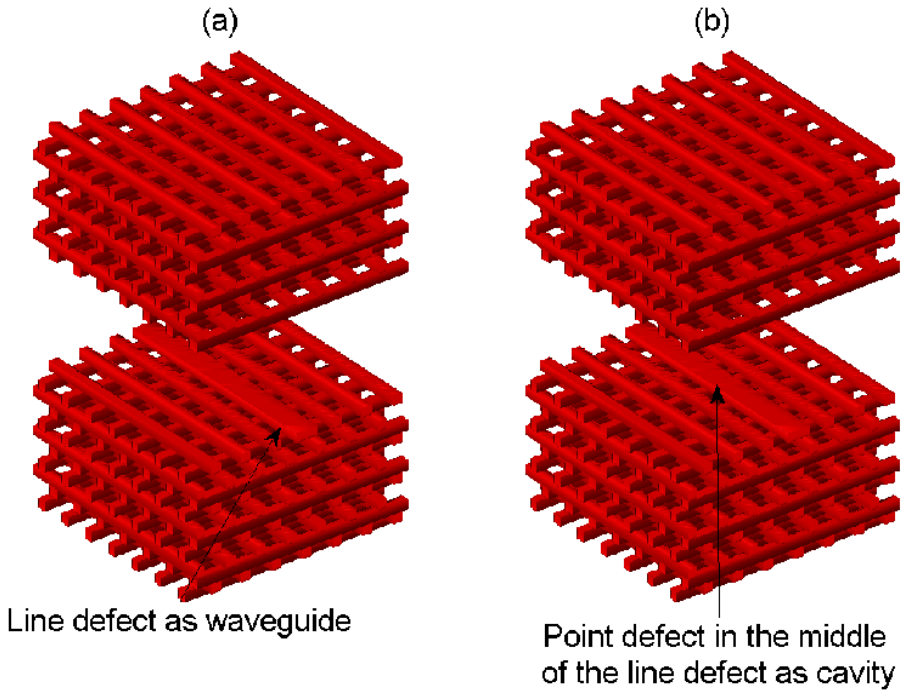

Figure 54. The spatial structure of (a) waveguide and (b) micro-cavity consisting of line and point defect in woodpile photonic crystal.

We first simulate the propagation of a wave packet in the waveguide in Figure 54 (a). The length of the waveguide is seven times the period of the woodpile photonic crystal. At the two directions that are perpendicular to the waveguide, there are two periods of woodpile photonic crystal to trap the waveguide mode. A dipole source is placed in the middle of the waveguide with polarization in the horizontal plane and perpendicular to the waveguide direction. The time evolution of the dipole source is Gaussian wave with center frequency in the middle of the band gap, $f_{center} = 0.3886c/a$, and band width $\Delta f_{center} = 0.25c/a$. The band width is larger than the band gap, so that part of the generated radiation field escape to the background from

the perpendicular direction. The other part of the generated radiation field with frequency inside of the band gap could excite the waveguide mode. The snapshots of the simulation result are plotted in Figure 55. The snapshots show that two strong wave packets are propagating along opposite directions. At the end of the waveguide, the wave packets are partly reflected back into the waveguide. Beside from these two main packets, there is weak waveform in the middle that is growing. This waveform could be due to the excitation of the band edge mode, which has small and (or) negative group velocity.

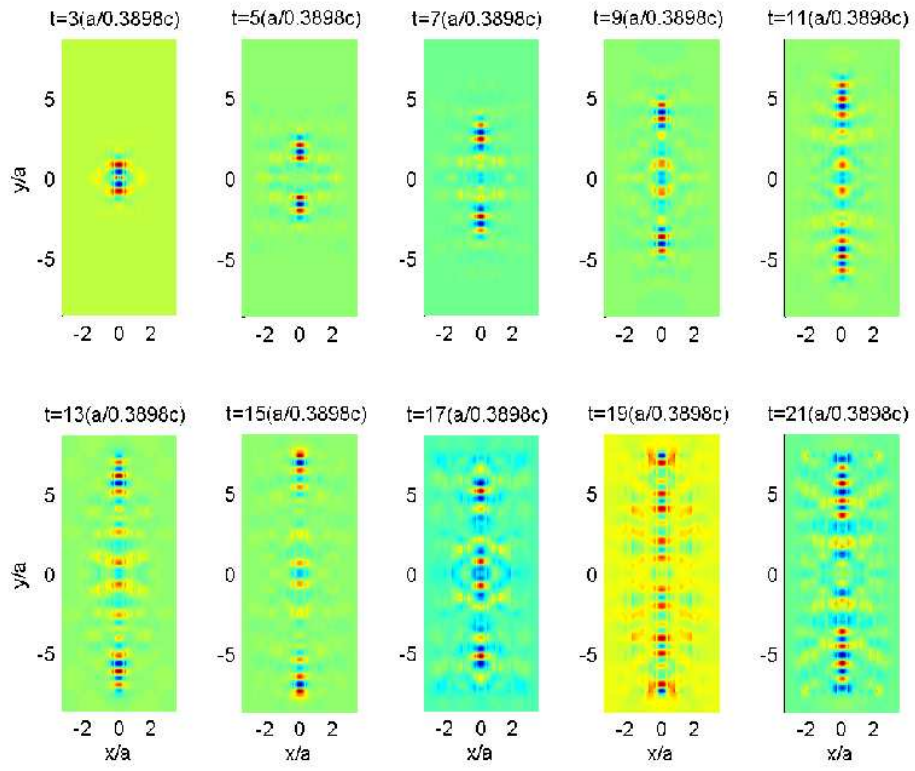

Figure 55. The snapshot of E_x in the waveguide shown in Figure 54 (a).

In addition to the simulation of the waveguide, the micro-cavity in Figure 54 (b) is simulated too. There are seven periods of woodpile photonic crystal block along each direction. The same dipole source is place in the middle of the cavity, and the simulation is run for 80 times the period of the center frequency. A receiver is placed at the same place as the dipole source, and the received signal is analyzed by fast Fourier transformation (FFT). The result is consistent with the reference result with the frequency of the resonant mode being $0.3898c/a$ [34]. The mode pattern is plotted in Figure 56.

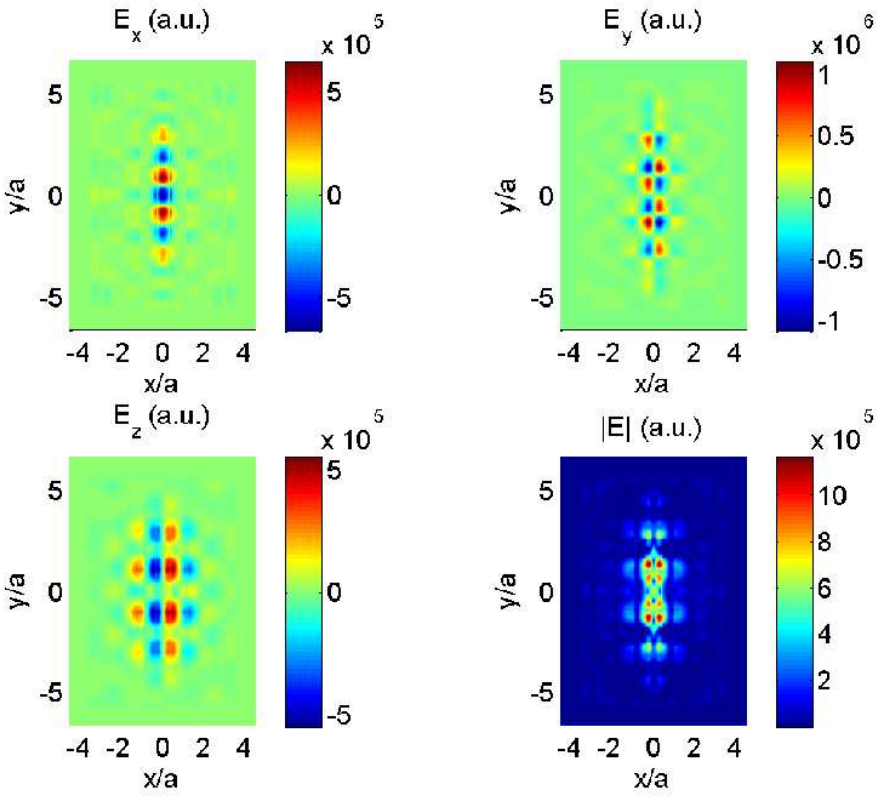

Figure 56. The field pattern of the cavity mode.

In conclusion, the SETD method can correctly and efficiently simulation the electromagnetic field in time domain.

Chapter Five. Spectral Element Time Domain Simulation for Maxwell-Bloch Equations

There are many nonlinear optical phenomena that can be simulated by the spectral element time domain method. Similar to the frequency domain simulation, the traditional method to simulate nonlinear effect is to make the slow varying approximation. The optical modes, which could be a plane wave or waveguide mode, are pre-calculated, and then the time and spatial evolution of the amplitude of the optical mode is simulated by the lower order differential equations. This traditional approximation strongly depends on the choice of the optical modes. For engineering design, the complete numerical simulation tool is more useful. In this section, the effort focuses on the quantum dot time domain dynamics in semiconductor nanostructures. The quantum dot is modeled as a two level system, and described by the Maxwell-Bloch equations.

5.1 Overview of Time Domain Maxwell-Bloch Equations

The Maxwell-Bloch equations include two parts[42,83]. Maxwell equations describe the electromagnetic field, and Bloch equations describe the dynamics of the two-level system in a quantum dot. Both of these two sets of equations include the interaction terms that describe the interaction between the electromagnetic field and the quantum dot.

Bloch equations are deduced from the observation averaging of the Heisenberg equation. The two-level system is modeled by the creation operator of the ground state and excited state, c_1^+ and c_2^+, as well as the corresponding annihilation operators, c_1 and c_2. The physical value that can be observed is the density matrix, which is

$$\begin{bmatrix} \rho_{11} & \rho_{12} \\ \rho_{21} & \rho_{22} \end{bmatrix} = \begin{bmatrix} \langle c_1^+ c_1 \rangle & \langle c_1^+ c_2 \rangle \\ \langle c_2^+ c_1 \rangle & \langle c_2^+ c_2 \rangle \end{bmatrix} \tag{5.1.1}$$

In the density matrix, ρ_{11} and ρ_{22} are the population on the ground state and the excited state; ρ_{12} and ρ_{21} are the microscopic polarizations, which describe the transition rate between the ground state to the excited state. With the present of the electromagnetic field, the Hamilton operator of the two-level system is

$$H = \hbar\omega_1 c_1^+ c_1 + \hbar\omega_2 c_2^+ c_2 - [\mathbf{d}_{1,2} \cdot \mathbf{E}(t)] c_1^+ c_2 - [\mathbf{d}_{2,1} \cdot \mathbf{E}(t)] c_2^+ c_1 + \frac{1}{2} \sum_{i,j,k,l} V_{k,l}^{i,j} c_i^+ c_j^+ c_k c_l \tag{5.1.2}$$

The first two terms describe the ground state and excited state themselves, with $\hbar\omega_1$ and $\hbar\omega_2$ being the energy level of the ground state and the excited state, respectively. The third and fourth terms describe the interaction between the two-level system with the electric field. $\mathbf{d}_{1,2}$ and $\mathbf{d}_{2,1} = \mathbf{d}_{1,2}^*$ are the dipole transition matrix elements between the ground state and the excited state, which is the same as $\mathbf{d}_{e,h}$ in Eq. (3.2.1)-(3.2.5). This value describes the strength of the interaction between the electric field and the two-level system. The last term in the Hamilton operator is the Coulomb interaction among

electrons inside the quantum dot. The dynamics of the creation and annihilation operator is described by the Heisenberg equation

$$\frac{dc_i(t)}{dt} = -\frac{i}{\hbar}\left[c_i(t), H\right] \tag{5.1.3}$$

The time evolution equation of the density matrix can be obtained by using the time evolution of each creation and annihilation operator, which gives the Bloch equations.

The radiation from the quantum dot is modeled by the generated polarization field $\mathbf{P}(t) = -N^{QD}(\mathbf{r})\mathbf{d}_{12}p_1(t)$, where t is time, $N^{QD}(\mathbf{r})$ is the density of quantum dot, $\mathbf{d}_{12}$ is the dipole transition matrix element between the ground state and the excited state, and $p_1(t) = \rho_{12} + \rho_{21}$ is the real component of the microscopic polarization. For a single quantum dot, the density of quantum dot is a delta function, $N^{QD}(\mathbf{r}) = \delta(\mathbf{r} - \mathbf{r}^{QD})$, with $\mathbf{r}^{QD}$ being the position of the quantum dot. The imaginary component of the microscopic polarization is defined as $p_2(t) = i(\rho_{12} - \rho_{21})$.

The Maxwell-Bloch equation in the semiclassical frame work is given as

$$\mu_0\mu_r\frac{\partial}{\partial t}\mathbf{H} = -\nabla\times\mathbf{E} \tag{5.1.4}$$

$$\varepsilon_0\varepsilon_r\frac{\partial}{\partial t}\mathbf{E} = \nabla\times\mathbf{H} - \sigma\mathbf{E} + N^{QD}\mathbf{d}_{12}\omega_{12}p_2 + \frac{N^{QD}\mathbf{d}_{12}p_1}{T_2} \tag{5.1.5}$$

$$\frac{dp_1}{dt} = -\omega_{12}p_2 - \frac{p_1}{T_2} \tag{5.1.6}$$

$$\frac{dp_2}{dt} = \omega_{12}p_1 - \frac{p_2}{T_2} + 2\frac{\mathbf{d}_{12}\cdot\mathbf{E}}{\hbar}\Delta \tag{5.1.7}$$

$$\frac{d\Delta}{dt} = -2\frac{\mathbf{d}_{12}\cdot\mathbf{E}}{\hbar}p_2 - \frac{\Delta-\Delta^{Pump}}{T_1} \tag{5.1.8}$$

where σ is the conductivity, $\omega_{12}=\omega_2-\omega_1$ is the resonant frequency of the two level system, $\hbar$ is the Planck constant, T_1 and T_2 are the longitudinal decay time and the transverse decay time of the two level system, $\rho_{12}=p_1+ip_2$ is the microscopic polarization of the two level system (which is the off-diagonal matrix element of the density matrix between the two levels) with p_1 (p_2) being the real (imaginary) part, $\Delta=\rho_{22}-\rho_{11}$ is the population inversion, and Δ^{pump} is the steady population inversion under the pumping. When there is no pumping, $\Delta^{pump}=-1$.

5.2 Quantum Dot Dynamics in Woodpile Photonic Crystal

In this sub-section, we discuss the implementation and numerical results of the spectral element time domain simulation for the Maxwell-Bloch equations. Maxwell equations are simulated by the spectral element time domain method, with the source term from the quantum dot polarization field. We assume that the quantum dot is uniformly distributed in a volume, so that the density of quantum dot, N^{QD}, is a constant within the elements that have quantum dot. Eq. (5.1.6)-(5.1.8) is an ordinary differential equation of scalar fields. Thus, the basis function and test function can be delta function in the chosen spatial point. In the SETD implementation of Eq (5.1.5), the spatial integral of the source requires the value of p_1 and p_2 at the GLL integration points, so the basis function and test function for p_1, p_2 and Δ are chosen to be the

spatial point at the GLL integration points. The fourth order explicit Runge-Kutta method is used to evaluate the time stepping of the Maxwell-Bloch equations.

5.2.1 Spontaneous Emission from Quantum Dot in Woodpile Photonic Crystal

The spontaneous emissions of a volume of 100 quantum dots in the middle of the woodpile photonic crystal waveguide are investigated. In this simulation, we are interested in the modification of the spontaneous emission by the local density of state of the nano-structure. Thus, we use an idea quantum dot that does not have decay, which means T_1 and T_2 are infinitely large. The resonant wavelength of the quantum dot is 1550 nm. The spatial structure of the system is in Figure 54 (a). Initially, the value of population inversion is at 81. The quantum dots in the excited state will start to radiate electromagnetic field and come down to the ground state. At the same time, the electromagnetic field interacts with the ground state quantum dots and excites them into the excited state. The average spontaneous rate is determined by the balancing of these two processes, and is relative to the structure of the background material. The woodpile photonic crystal waveguide increases the photon density of state at the frequency of waveguide mode, and decreases the photon density of state in the band gap, so that the spontaneous emission rate can be modified. By changing the lattice constant of the woodpile photonic crystal, the frequency range of the band gap and waveguide mode can be tuned. We have calculated the spontaneous emission from two cases, with the resonant frequency of the quantum dots within the waveguide mode and in the band

gap for each case. We have calculated the spontaneous emission of the same volume of 100 quantum dots in vacuum as comparison. The time domain dynamics of the total population inversion is plotted in Figure 57. When the resonant frequency of the quantum dots is in the frequency band of the waveguide mode, the decay rate is larger than that in vacuum, because the photon density of state is larger. On the other hand, when the resonant frequency is in the band gap, the spontaneous emission is suppressed, and the decay rate is smaller.

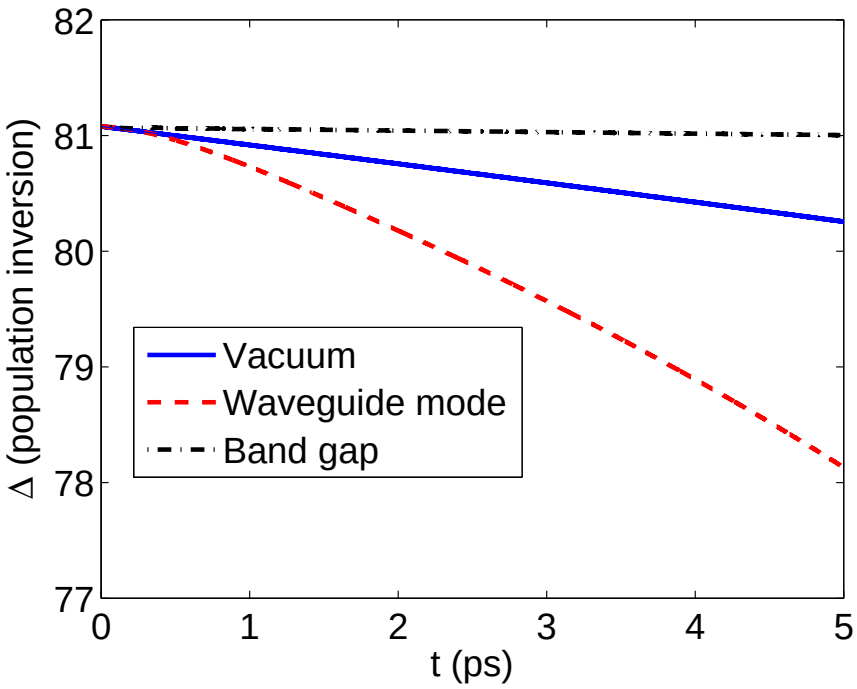

Figure 57. Time decaying of total population inversion. Comparing to the decay rate of the same volume of quantum dots in vacuum, when the resonant frequency of the quantum dots is in the waveguide mode, the decay rate is larger; when the resonant frequency of the quantum dots is in the band gap, the decay rate is smaller.

5.3 Quantum Dot Dynamics in Air-Flow Nano-Sphere

A previous implementation of the finite element/spectral element time domain method uses the domain decomposition method to simulate large systems with complicate structures[84,85]. In this subsection, Bloch equations are implemented in the code package. In this implementation, the quantum dot is modeled as a point dipole source, whose amplitude and time variation are determined by p_1 and p_2. Each two-level system has a corresponding set of Bloch equations. We have simulation the quantum dot dynamics of a single quantum dot in the middle of a dielectric nano-sphere. The sphere is made of GaAs, with radius being 349 nm. The background material is air. This system has a resonant mode at 1536.1 nm. We use a GaAs/InAs quantum dot with resonant wavelength being 1536 nm, and the longitudinal decay time being $T_1 = 10$ ps, the transverse decay time being $T_2 = 75$ fs. Thus, the quantum dot is near resonant with the cavity mode of the nano-sphere.

5.3.1 Population Inversion of Quantum Dots in Nano-Sphere

In this subsection, we are interested in exciting the quantum dots into the excited state, and making them stay in positive population inversion. With a positive population inversion, the quantum dots are more likely to be in the excited state. In this case, the stimulated emission of photon has larger probability, which is important for laser.

In the simulation of this subsection, an external incident electromagnetic field is applied to the nano-sphere. The quantum dot in the nano-sphere is initially in the

ground state. The incident field will excite the quantum dot into the excited state. The Maxwell-Bloch equations will be simulated to observe the oscillation of the population inversion under the driven force from the external electromagnetic field. The purpose of these simulations is to determine the condition to obtain positive population inversion. The simulation starts with the case where the incident wave is a continuous wave with frequency resonant to the quantum dot resonant frequency. In order to avoid the high frequency wave, the amplitude of the continuous wave is gradually turned on with the amplitude being proportional to $(1-e^{-t/\tau})$. τ is the relaxation time of the incident wave, which is chosen to be five times of the period of the incident wave. The threshold of the strength of the electric field in the nano-sphere to obtain positive population inversion is investigated. Because the break-down electric field of the GaAs is 4×10^7 V/m, we need to make sure that the maximum amplitude of the electric field in the nano-sphere is smaller than the break-down electric field. The result of one simulation is shown in Figure 58. In this simulation, the maximum electric field amplitude is 2.6×10^7 V/m. From Figure 58 (a), after 0.5 ns, the population inversion becomes stable near zero. In this case, the stable population inversion is still negative. The Fourier transformation of the population inversion is plotted in Figure 58 (b). The Fourier spectrum shows that the dominant part of the time evolution is the stable and low frequency oscillation. However, there is a small peak at 390.6 THz, which is double of the resonant frequency at 195.3 THz. This phenomenon matches the conclusion from the frequency domain

analysis. The nonlinear term $2\mathbf{d}_{12} \cdot \mathbf{E} p_2 / \hbar$ in Eq. (5.1.8) is the source of the second harmonic oscillation. When both electric field and p_2 is harmonic oscillation, the product-to-sum trigonometric identity gives a second harmonic oscillation term. From the simulation result in Figure 58 (b), the amplitude of the second harmonic oscillation is 100 times smaller than the lower frequency oscillation and stable population inversion. As a result, it is reasonable to neglect the second harmonic oscillation in the frequency domain simulation.

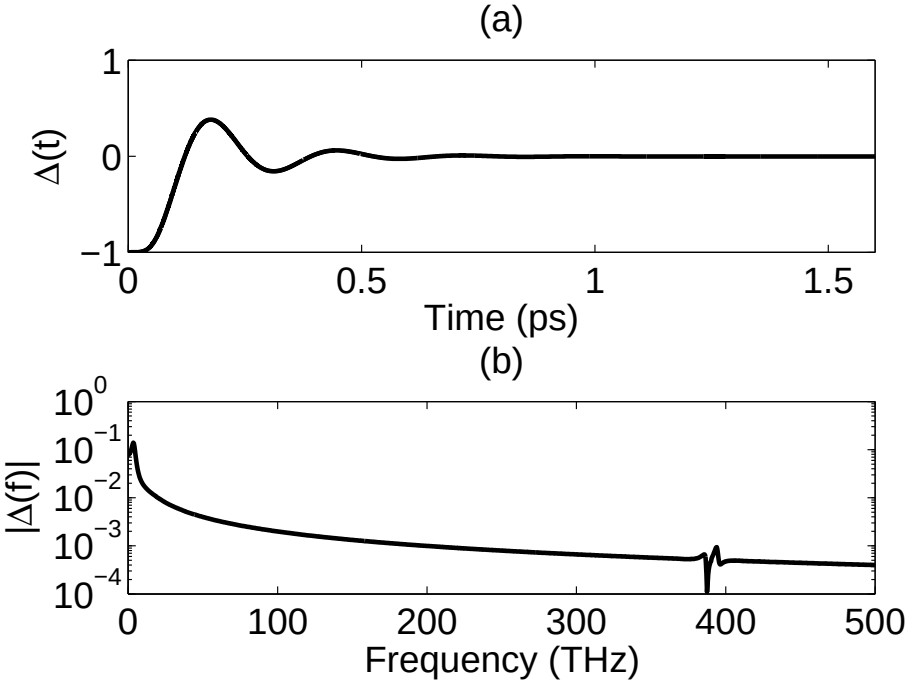

Figure 58. (a) Time evolution of population inversion under an external incident continuous wave with frequency being 195.3 THz. (b) The Fourier spectrum of the population inversion. A peak appears at the second harmonic frequency, 390.6 THz.

From Figure 58 (a), the population inversion does turn positive at an early time, but the oscillation makes the population inversion get back to negative in latter time. The reason that the population inversion starts to drop down after reaching the peak is that the external incident electromagnetic field starts the stimulated emission of the quantum dot. Thus, the population in the excited state decreases. In order to keep the positive population inversion in early time, we can use a short pulse instead of a continuous wave excitation. If the external driven force from the incident field stops when the population inversion is positive, the oscillation of the population inversion also stops. Thus, the population inversion can stay positive. The population inversion with excitation of a pulse with pulse width being 0.17 ps is plotted in Figure 59. For this pulse width, the external incident electromagnetic field is turned off when the population inversion is at the peak. As a result, there is not external electrical field to excite the stimulated emission and the population inversion can stay positive. The figure shows that the population inversion stays positive after the excitation pulse end, and decays at the rate of the corresponding spontaneous emission rate.

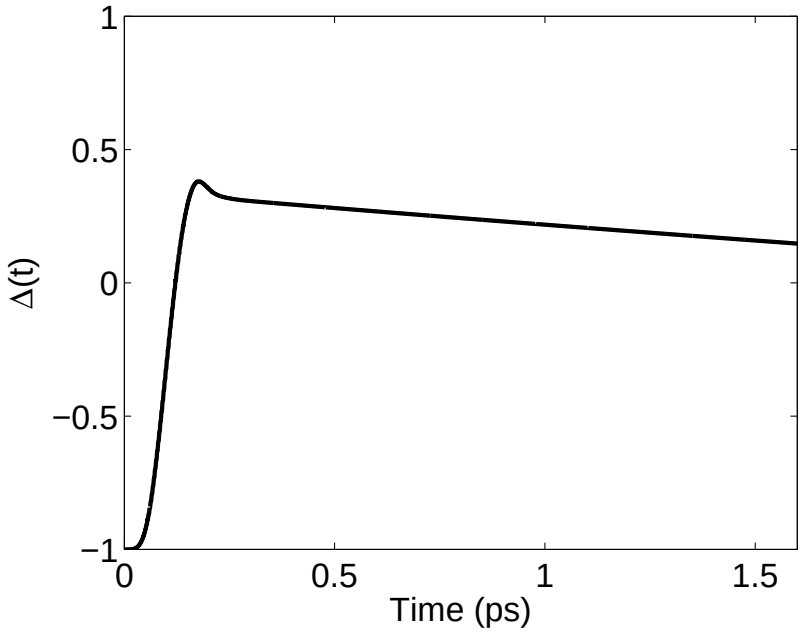

Figure 59. Time evolution of population inversion under an external incident pulse wave with frequency being 195.3 THz and pulse width being 0.17 ps.

The numerical results in this chapter show that the Maxwell-Bloch equations can model the quantum dot dynamics. The spontaneous emission rate of the quantum dot will be modified by the local density of state of the photon. This local density of state is determined by the spatial structure of the dielectric environment. In the simulation of the Maxwell-Bloch equations, the modification of the spontaneous emission rate is naturally included. The future developments of this project include the electrical pump effect and investigation of the laser dynamics of nano-structures.

Chapter Six. Conclusion and Future Prospects

6.1 Conclusion

We have developed efficient simulation tools for linear optics and electromagnetic fields with the spectral element method. Two types of solvers are implemented: a frequency domain solver that simulates eigenstate oscillations and continuous wave scattering, and a time domain solver that simulates the time evolution of electromagnetic field.

For the frequency domain solver, the three-dimensional as well as two dimensional solvers calculate the band structures of photonic crystals with high accuracy and efficiency. The optical scattering of thin films can be modeled by the combination of spectral element method and method of moments. The solver was used to investigate the linear excitation of surface plasmon polariton in thin film systems. A block-Thomas algorithm was implemented to increase the efficiency of the scattering simulation of multiple layers of photonic crystal slab. A domain decomposition method was implemented to simulate finite size large scale periodic thin film structures.

As to the time domain solver, the spectral element time domain method was implemented. The solver was used to simulate time domain excitation of resonant modes in a micro-cavity consisting of photonic crystal. These solvers are shown to be more efficient than the widely used method, such as plane wave expansion, finite difference frequency domain and time domain methods, and finite element method.

We have extended the frequency domain solver to simulate the second harmonic generation of a photonic crystal slab. The scattering problems of both fundamental and second harmonic frequency fields are simulated in parallel. The nonlinear effect is modeled by the classical nonlinear optical theory. The nonlinear polarization fields are calculated from the numerical electrical field, and enter the vector Helmholtz equation of the electric field as a source term. The only approximation in the solver is the spatial discretization of the spectral element method. We further deduce the formula to calculate the sensitivity of the electromagnetic field to the thickness of each layer of the photonic crystal slab. A design of multiple-layer photonic crystal slab is found to have ten order of magnitude enhancement of the second harmonic generation effect at resonant wavelengths compare to a uniform multiple layer structure.

We have also extended the frequency domain and time domain solvers to simulate the quantum dot dynamics. The time domain Maxwell-Bloch equations are transformed into frequency domain. The nonlinear terms in this set of equations result in the high harmonic oscillations of the population inversion of the quantum dot. The numerical results show that the population inversion will not become positive under the continuous wave excitation.

The time domain solver for the Maxwell-Bloch equations directly calculate the time evolution of the Bloch equations, and model the radiation from the quantum dot as a dipole source in Maxwell equations. So far as we know, this is the first implementation

of the Maxwell-Bloch equations in a three-dimensional system. The time domain implementation was used to calculate the spontaneous emission from quantum dots in a woodpile photonic crystal nano-structure. The numerical results confirm that the local density of state of the dielectric nano-structure modifies the spontaneous emission rate. The time domain Maxwell-Bloch equations are also used to simulate the population inversion dynamic under the continuous wave and pulsed wave excitations. Under continuous wave excitation, the population inversion has low frequency oscillations between positive and negative, and stays negative after a long time. From the intelligent information of the continuous wave simulation, we chose the correct pulse width for the pulse wave excitation and obtained positive population inversion.

6.2 Future Prospects

For the frequency domain linear electromagnetic field solver, one of the most important features is the analysis of the sensitivity. Engineering design usually require optimization of the structure. The numerical result of the frequency domain simulation can give the electromagnetic field under certain environments. The figure of merit can be calculated from the solution of the electromagnetic field. In order to optimize the figure of merit, we need to know how the figure of merit changes as the structure changes. The sensitivity gives the analytical derivative of the electromagnetic field to the shape of the structure. This information is very helpful for the optimization algorithm, because it tells the algorithm which part of the structure has the most impact to the

figure of merit. In this thesis, the sensitivity analysis is restricted to the thickness of the multiple layers photonic crystal slab. In general, engineers are also interested in the sensitivity to the radius of the periodic hole, or the arbitrary change of the shape of any part of the photonic crystal slab. The sensitivity analysis is interesting for other research areas, such as the design of antenna or aircraft. As a result, one of the most important future prospects is to implement the sensitivity calculation of arbitrary change of the elements.

For the time domain solver, the Maxwell-Bloch equations solver needs to be upgraded to simulate the physics of nano-laser. The two-level system is a good model for quantum dot. However, the real quantum dot has more energy levels. In addition to the two primal energy levels, the other energy levels, named as auxiliary energy levels, are important to the pumping process for the laser. A set of Bloch equations of four-level system will be needed to simulate the real quantum dot. In addition to the simulation of the quantum dot, the wetting layer under the quantum dot is critical to the electrical pumping of the nano-laser[83]. The current injection from external current source into the wetting layer needs to be simulated by Bloch equation also.

For the time domain solver of linear electromagnetic field, an implementation of bloch-Thomas algorithm for a multiple layer system will have a lot of potential applications. In addition, the combination of the domain decomposition method and block-Thomas algorithm can increase the efficiency of the simulation of larger system.

References

1. B. Ellis, M. A. Mayer, G. Shambat, T. Sarmiento, J. Harris, E. E. Haller and J. Vuckovic, "Ultralow-threshold electrically pumped quantum-dot photonic-crystal nanocavity lase", Nature Photonics, 5, 297-300 (2011).

2. K. Aoki, D. Guimard, M. Nishioka, M. Nomura, S. Iwamoto and Y. Arakawa, "Coupling of quantum-dot light emission with a three-dimensional photonic-crystal nanocavity", Nature Photonics, 2, 688-692 (2008).

3. S. Matsuo, A. Shinya, T. Kakitsuka, K. Nozaki, T. Segawa, T. Sato, Y. kawaguchi and M. Notomi, "High-speed ultracompact buried heterostructure photonic-crystal laser with 13 fJ of energy consumed per bit transmitted", Nature Photonics, 4, 648-654 (2010).

4. M. Loncar, T. Yoshie, A. Scherer, P. Gogna and Y. Qiu, "Low-threshold photonic crystal laser", Appl. Phys. Lett. 81, 2680-2682 (2002).

5. J. Vuckovic and Y. Yamamoto, "Photonic crystal microcavities for cavity quantum electrodynamics with a single quantum dot", Appl. Phys. Lett, 82, 2374-2376 (2003).

6. S. Strauf, K. Hennessy, M. T. Rakher, Y. –S. Choi, A. Badolato, L. C. Andreani, E. L. Hu, P. M. Petroff and D. Bouwmeester, "Self-tuned quantum dot gain in photonic crystal lasers", Phys. Rev. Lett. 96, 127404 (2006).

7. T. Yoshie, A. Scherer, J. Hendrickson, G. Khitrova, H. M. Gibbs, G. Rupper, C. Ell, O. B. Shchekin and D. G. Deppe, "Vacuum Rabi splitting with a single quantum dot in a photonic crystal nanocavity", Nature, 432, 200-203 (2004).

8. R. F. Oulton, V. J. Sorger, T. Aentgraf, R. M. Ma, C. Gladden, L. Dai, G. Bartal and X. Zhang, "Plasmon laser at deep subwavelength scale", Nature, 461, 629-632, (2009).

9. C. Manolatou and F. Rana, "Subwavelength nanopatch cavities for semiconductor plasmon lasers", IEEE Journal of Quantum Electronics, 44, 435-447 (2008).

10. S. D. Gedney, "An anisotropic perfectly matched layer-absorbing medium for the truncation of FDTD lattices", IEEE Transactions on Antennas and Propagation, 44, 1630-1639 (1996).

11. C.-P. Yu and H.-C. Chang, "Compact finite-difference frequency-domain method for the analysis of two-dimensional photonic crystals", Opt. Express 12, 1397-1408 (2004).

12. S. Johnson and J. Joannopoulos, "Block-iterative frequency-domain methods for Maxwell's equations in a planewave basis,", Opt. Express 8, 173-190 (2001)

13. K. M. Ho, C. T. Chan and C. M. Soukoulis, "Existence of a photonic gap in periodic dielectric structures", Phys. Rev. Lett. 65, 3152-3155 (1990).

14. M. G. Moharam and T. K. Gaylord, "Rigorous coupled-wave analysis of metallic surface-relief gratings", J. Opt. Soc. Am. A, Vol 3, 1780-1787 (1986).

15. S. Wang, R. Lee and F. L. Teixeira, "Anisotropic-medium PML for vector FETD with modified basis functions", IEEE Transaction on Antennas and Propagation, 54, 20-27 (2006).

16. B. G. Ward, "Finite element analysis of photonic crystal rods with inhomogeneous anisotropic refractive index tensor", IEEE Journal of Quantum Electronics, 44, 150-156 (2008).

17. P. Sotirelis and J. D. Albrecht, "Numerical simulation of photonic crystal defect modes using unstructured grids and Wannier functions", Phys. Rev. B, 76, 075123 (2007).

18. J. S. Savage and A. F. Peterson, "Higher-Order vector finite elements for tetrahedral cells", IEEE transactions on Microwave Theory and Techniques, 44, 874-879 (1996).

19. G. C. Cohen, "Higher-order numerical methods for transient wave equations", Springer, (2001).

20. J.-H. Lee and Q. H. Liu, "An efficient 3-D spectral-element method for Schrödinger equation in nanodevice simulation", IEEE transactions on Computer-Aided Design of Integrated Circuits and Systems, 24, 1848-1858 (2005).

21. J. -H. Lee, T. Xiao and Q. H. Liu, "A 3-D spectral-element method using mixed-order curl conforming vector basis functions for electromagnetic fields", IEEE transactions on Microwave Theory and Techniques, 54, 437-444 (2006).

22. A. T. Patera, "A spectral element method for fluid dynamics: Laminar flow in a channel expansion", Journal of Computational Physics, 54, 468-488 (1984).

23. D. Komatitsch and J. Tromp, "Spectral-element simulations of global seismic wave propagation-I. Validation", Geophys. J. Int. 149, 390-412 (2002).

24. J.-H. Lee and Q. H. Liu, "A 3-D spectral element time-domain method for electromagnetic simulation", IEEE Transactions on Microwave Theory and Thchniques, 55, 983-991 (2007).

25. Q. H. Liu, "A pseudospectral frequency-domain (PSFD) method for computational electromagnetics", IEEE Antennas and Vireless Propagation Letters, 1, 131-134 (2002).

26. Q. H. Liu, "The PSTD algorithm: a time-domain method requiring only two cells per wavelength", Microwave and Optical Technology Letters. 15, 158-165 (1997).

27. J. D. Joannopoulos, "Photonic crystals: modeling the flow of light", second edition, Princeton University Press, Princeton (2008).

28. E. Yablonovitch, "Inhigited spontaneous emission in solid-state physics and electronics", Phys. Rev. Lett. 58, 2059-2062 (1987).

29. S. John, "Strong localization of photons in certain disordered dielectric superlattices", Phys. Rev. Lett. 58, 2486-2489 (1987).

30. K. B. Crozier, V. Lousse, O. Kilic, S. Kim, S. Fan and O. Solgaard, "Air-bridge photonic crystal slabs at visible and near-infrared wavelengths", Phys. Rev. B. 73, 115126 (2006).

31. Y. Akahane, T. Asano, B.-S. Song and S. Noda, "High-Q photonic nanocavity in a two-dimensional photonic crystal", Nature, 425, 944-947 (2003).

32. S. Noda, K. Tomoda, N. Yamamoto and A. Chutinan, "Full three-dimensional photonic bandgap crystals at near-infrared wavelengths", Science, 289, 604-606 (2000).

33. B. Gralak, M. de Dood, G. Tayeb, S. Enoch and D. Maystre, "Theoretical study of photonic band gaps in woodpile crystals", Phys. Rev. E, 67, 066601 (2003).

34. L. Tang and T. Yoshie, "Ultra-high-Q three-dimensional photonic crystal nano-resonators", Opt. Express **15**, 17254-17263 (2007).

35. L. Tang and T. Yoshie, "Monopole woodpile photonic crystal modes for light-matter interaction and optical trapping", Opt. Express 17, 1346-1351 (2009).

36. P. Harrison, "Quantum wells, wires and dots: theoretical and computational physics of semiconductor nanostructures", thire edition, Viley Press (2009).

37. C. Pryor, "Eight-band calculations of strained InAs/GaAs quantum dots compared with one-, four-, and six-band approximations", Phys. Rev. B, 57, 7190-7195 (1998).

38. P. A. Franken, A. E. Hill, C. W. Peters and G. Weinreich, "Generation of Optical Harmonics", Phys. Rev. Lett, 7, 118-119 (1961).

39. S. W. Koch, M. Kira, G. Khitrova and H. M. Gibbs, "Semiconductor excitons in new light", nature Materials, 5, 523-531 (2006).

40. F. Jahnke, M. Kira, S. W. Koch, G. Khitrova, E. K. Lindmark, T. R. Nelson, Jr., D. V. Wick, J. D. Berger, O. Lyngnes, H. M. Gibbs and K. Tai, "Excitonic nonlinearities of semiconductor microcavities in the nonperturbative regime", Phys. Rev. Lett, 77, 5257-5260 (1996).

41. A. Auffeves-Garnier, C. Simon, J.-M. Gerard, and J.-P. Poizat, "Giant optical nonlinearity induced by a single two-level system interacting with a cavity in the Purcell regime", Phys. Rev. A, 75, 053823 (2007).

42. H. Takeda and S. John, "Self-consistent Maxwell-Bloch theory of quantum-dot-population switching in photonic crystals", Phys. Rev. A, 83, 053811 (2011).

43. M. Sukharev and A. Nizan, "Numerical studies of the interaction of an atomic sample with the electromagnetic field in two dimensions", Phys. Rev. A, 84, 043802 (2011).

44. S.-H. Chang and A. Taflove, "Finite-difference time-domain model of lasing action in a four-level two-electron atomic system", Opt. Express 12, 3827-3833 (2004).

45. A. Fratalocchi, C. Conti and G. Ruocco, "Three-dimensional *ab initio* investigation of light-matter interaction in Mie lasers", Phys. Rev. A, 78, 013806 (2008).

46. M. Luo, Q. H. Liu and Z. Li, "Spectral element method for band structures of two-dimensional anisotropic photonic crystals", Phys. Rev. E, 79, 026705 (2009).

47. M. Luo and Q. H. Liu, "Accurate determination of band structures of two-dimensional dispersive anisotropic photonic crystals by the spectral element method", J. Opt. Soc. Am. A 26, 1598-1605 (2009).

48. M. Luo and Q. H. Liu, "Spectral element method for band structures of three-dimensional anisotropic photonic crystals", Phys. Rev. E, 80, 056702 (2009).

49. M. Luo and Q. H. Liu, "Three-dimensional dispersive metallic photonic crystals with a bandgap and a high cutoff frequency", J. Opt. Soc. Am. A 27, 1878-1884 (2010).

50. M. Luo and Q. H. Liu, "Extraordinary transmission of a thick film with a periodic structure consisting of strongly dispersive materials", J. Opt. Soc. Am. B 28, 629-636 (2011).

51. M. N. Vouvakis, S.-C. Lee, K. Zhao and J.-F. Lee, "A symmetric FEM-IE formulation with a single-level IE-QR algorithm for solving electromagnetic radiation and scattering problems", IEEE Transactions on Antennas and Propagation, 52, 3060-3070 (2004).

52. M. M. Botha and J.-M. Jin, "On the variational formulation of hybrid finite element-boundary integral techniques for electromagnetic analysis", IEEE Transactions on Antennas and Propagation, 52, 3037-3047 (2004).

53. M. Luo, Q. H. Liu, and J. Guo, "A spectral element method calculation of extraordinary light transmission through periodic subwavelength slits", J. Opt. Soc. Am. B 27, 560-566 (2010).

54. P. B. Johnson and R. W. Christy, "Optical constants of the noble metals", Phys. Rev. B, 6, 4370-4379 (1972).

55. G. Granet and L. Li, "Convincingly converged results for highly conducting periodically perforated thin films with square symmetry", Journal of Optics A: Pure and Applied Optics, 8, 546-549 (2006).

56. L. Lin, R. J. Reeves and R. J. Blaikie, "Surface-plasmon-enhanced light transmission through planar metallic films", Phys. Rev. B, 74, 155407 (2006).

57. J. Chen, B. Zhu, W. Zhong, and Q. H. Liu, "A semianalytical spectral element method for the analysis of 3-D layered structures", IEEE Transactions on Antennas and Propagation, 59, 1-8 (2011).

58. M. Luo, Y. Lin and Q. H. Liu, "Spectral methods and domain decomposition for nanophotonic applications", Proceedings of the IEEE, Vol. 101, 473-483 (2013).

59. K. Zhao, V. Rawat, S.-C. Lee and J.-F. Lee, "A domain decomposition method with nonconformal meshes for finite periodic and semi-periodic structures", IEEE Transactions on Antennas and Propagation, 55, 2559-2570 (2007).

60. K. Zhao, V. Rawat and J.-F. Lee, "A domain decomposition method for electromagnetic radiation and scattering analysis of multi-target problems", IEEE Transactions on Antennas and Propagation, 56, 2211-2221 (2008).

61. M. N. Vouvakis, Z. Cendes and J.-F. Lee, "A FEM domain decomposition method for photonic and electromagnetic band gap structures", IEEE Transactions on Antennas and Propagation, 54, 721-733 (2006).

62. Z.-Q. Lü, X. An and W. Hong, "A fast domain decomposition method for solving three-dimensional large-scale electromagnetic problems", IEEE Transactions on Antennas and Propagation, 56, 2200-2210 (2008).

63. V. Shankar, A. H. Mohammadian and W. F. Hall, "A time-domain finite-volume treatment for the Maxwell equations", Electromagn., 10, 127-145 (1990).

64. A. H. Mohammadian, V. Shankar and W. F. Hall, "Computation of electromagnetic scattering and radiation using a time-domain finite-volume discretization peocedure", Computer Physics Communications, 68, 175-196 (1991).

65. A. V. Koldoba, O. A. Kuznetsov and G. V. Ustyugova, "An approximate Riemann solver for relativistic magnetohydrodynamics", Mon. Not. R. Astron. Soc. 333, 932-942 (2002).

66. Q. H. Liu, Y. Lin, J. Liu, J.-H. Lee and E. Simsek, "A 3-D spectral integral method (SIM) for surface integral equations", IEEE Microwave and Wireless Components Letters, 19, 62-64 (2009).

67. Y. Lin, J.-H. Lee, J. Liu, M. Chai, J. A. Mix and Q. H. Liu, "A hybrid SIM-SEM method for 3-D electromagnetic scattering problems", IEEE Transactions on Antennas and Propagation, 57, 3655-3663 (2009).

68. N. Liu, H. Guo, L. Fu, S. Kaiser, H. Schweizer and H. Girssen, "Three-dimensional photonic metamaterials at optical frequencies", Nature Materials, 7, 31-37 (2008).

69. I. Sersic, M. Frimmer, E. Verhagen and A. F. Koenderink, "Electric and magnetic dipole coupling in near-infrared split-ring metamaterial arrays", Phys. Rev. Lett., 103, 213902 (2009).

70. C. Enkrich, M. Wegener, S. Linden, S. Burger, L. Zschiedrich, F. Schmidt, J. F. Zhou, Th. Koschny and C. M. Soukoulis, "Magnetic metamaterials at telecommunication and visible frequencies", Phys. Rev. Lett., 95, 203901 (2005).

71. R. L. Sutherland, "Handbook of nonlinear optics", Second Edition, Marcel Dekker Inc, New York, (2003).

72. S. E. Harris, Proposed backward wave oscillation in the infrared", Appl. Phys. Lett., 9, 114-116 (1966).

73. J. Torres, D. Coquillat, R. Legros, J. P. Lascaray, F. Teppe, D. Scalbert, D. Peyrade, Y. Chen, O. Briot, M. Le Vassor d'Yerville, E. Centeno, D. Cassagne and J. P. Albert, "Giant second-harmonic generation in a one-dimensional GaN photonic crystal", Phys. Rev. B, 69, 085105 (2004).

74. Y. Dumeige, I. Sagnes, P. Monnier, P. Vidakovic, I. Abram, C. Mériadec and A. Levenson, "Phase-matched frequency doubling at photonic band edges: efficiency scaling as the fifth power of the length", Phys. Rev. Lett. 89, 043901 (2002).

75. R. Iliew, C. Etrich, T. Pertsch, F. Lederer and Y. S. Kivshar, "Huge enhancement of backward second-harmonic generation with slow light in photonic crystals", Phys. Rev. A, 81, 023820 (2010).

76. A. M. Malvezzi, G. Vecchi, M. Patrini, G. Guizzetti, L. C. Andreani, F. Romanato, L. Businaro, E. Di Fabrizio, A. Passaseo and M. De Vittorio, "Resonant second-harmonic generation in a GaAs photonic crystal waveguide", Phys. Rev. B, 68, 161306(R) (2003).

77. Y. Dumeige, F. Raineri, A. Levenson and X. Letartre, "Second-harmonic generation in one-dimensional photonic edge waveguides", Phys. Rev. E, 68, 066617 (2003).

78. J. Bravo-Abad, A. Rodriguez, P. Bermel, S. G. Johnson, J. D. Joannopoulos, and M. Soljacic, "Enhanced nonlinear optics in photonic-crystal microcavities", Opt. Express 15, 16161-16176 (2007).

79. M. Luo and Q. H. Liu, "Enhancement of second harmonic generation in an air-bridge photonic crystal slab: simulation by spectral element method", Accepted by

80. D. E. Aspnes and A. A. Studna, "Dielectric function and optical parameters of Si, Ge, GaP, GaAs, GaSb, InP, InAs, and InSb from 1.5 to 6.0 eV", Phys. Rev. B, 27, 985-1009 (1983).

81. I. Shoji, T. Kondo, A. Kitamoto, M. Shirane and R. Ito, "Absolute scale of second-order nonlinear-optical coefficients", J. Opt. Soc. Am. B, 14, 2268-2294 (1997).

82. A. Gordon, C. Y. Wang, L. Diehl, F. X. Kärtner, A. Belyanin, D. Bour, S. Corzine, G. Höfler, H. C. Liu, H. Schneider, T. Maier, M. Troccoli, J. Faist and F. Capasso, "Multimode regines in quantum cascade lasers: from coherent instabilities to spatial hole burning", Phys. Rev. A, 77, 053804 (2008).

83. J. E. Kim, E. Malic, M. Fichter, A. Wilms and A. Knorr, "Maxwell-Bloch equation approach for describing the microscopic dynamics of quantum-dot surface-emitting structures", IEEE journal of Quantum Electronics, 46, 1115-1126 (2010).

84. J.-H. Lee, J. Chen and Q. H. Liu, "A 3-D discontinuous spectral element time-domain method for Maxwell's equations", IEEE Transactions on Antennas and Propagation, 57, 2666-2674 (2009).

85. J. Chen, Q. H. Liu, M. Chai and J. A. Mix, "A nonspurious 3-D vector discontinuous Galerkin finite-element time-domain method", IEEE Microwave and Wireless Components Letters, 20, 1-3 (2010).

86. H. F. Hofmann and O. Hess, "Quantum Maxwell-Bloch equations for spatially inhomogeneous semiconductor lasers", Phys. Rev. A, 59, 2342-2358 (1999).

87. H. C. Schneider, F. Jahnke, S. W. Koch, J. Tignon, T. Hasche and D. S. Chemla, "Polariton propagation in high quality semiconductors: microscopic theory and experiment versus additional boundary conditions", Phys. Rev. B, 63, 045202 (2001).

88. D. Schiumarimi, N. Tomassini, L. Pilozzi and A. D'Andrea, "Polariton propagation in weak-donfinement quantum wells", Phys. Rev. B, 82, 075303 (2010).

89. S. Bischoff, A. Knorr and S. W. Koch, "Theoretical investigation of the excitonic semiconductor response for varying material thickness: transition from quantum well to bulk", Phys. Rev. B, 55, 7715-7725 (1997).

90. N. C. Nielsen, J. Kuhl, M. Schaarschmidt, J. Förstner, A. Knorr, S. W. Koch, G. Khitrova, H. M. Gibbs and H. Giessen, "Linear and nonlinear pulse propagation in a multiple-quantum-well photonic crystal", Phys. Rev. B, 70, 075306 (2004).

91. D. Gerace and L. C. Andreani, "Quantum theory of exciton-photon coupling in photonic crystal slabs with embedded quantum wells", Phys. Rev. B, 75, 235325 (2007).

92. A. Askitopoulos, L. Mouchliadis, I. Iorsh, G. Christmann, J. J. Baumberg, M. A. Kaliteevski, Z. Hatzopoulos and P. G. Savvidis, "Bragg polaritons: strong coupling and amplification in an unfolded microcavity", Phys. Rev. Lett., 106, 076401 (2011).

93. D. Goldberg, L. I. Deych, A. A. Lisyansky, A. Shi, V. M. Menon, V. Tokranov, M. Yakimov and S. Oktyabrsky, "Exciton-lattice polaritons in multiple-quantum-well-based photonic crystals", Nature Photonics, 3, 662-666 (2009).

94. H. M. Gibbs, G. Khitrova and S. W. Koch, "Exciton-polariton light-semiconductor coupling effects", Nature Photonics, 5, 273-282 (2011).

95. D. Bajoni, D. Gerace, M. Galli, J. Bloch, R. Braive, I. Sagnes, A. Miard, A. Lemaitre, M. Patrini and L. C. Andreani, "Exciton polaritons in two-dimensional photonic crystals", Phys. Rev. B, 80, 201308 (2009).

96. S. Nojima, "Optical response of excitonic polaritons in photonic crystals", Phys. Rev. B, 59, 5662-5677 (1999).

97. N. Tomassini, D. Schiumarini, L. Pilozzi and A. D'Andrea, "Exciton and polariton dispersion curves of $In_xGa_{1-x}As/GaAs(001)$ superlattice quantum wells: model calculation", Phys. Rev. B, 75, 085317 (2007).

98. Y. Zeng, Y. Fu, X. Chen, W. Lu and H. Ågren, "Complete band gaps in three-dimensional quantum dot photonic crystals", Phys. Rev. B, 74, 115325 (2006).

99. M. V. Erementchouk, L. I. Deych and A. A. Lisyansky, "Optical properties of one-dimensional photonic crystals based on multiple-quantum-well structures", Phys. Rev. B, 71, 235335 (2005).

100. M. V. Erementchouk, L. I. Deych and A. A. Lisyansky, "Spectral properties of exciton polaritons in one-dimensional resonant photonic crystals", Phys. Rev. B, 73, 115321 (2006).

101. P. Vasa, R. Pomraenke, S. Schwieger, Y. I. Mazur, Vas. Kunets, P. Srinivasan, E. Johnson, J. E. Kihm, D. S. Kim, E. Runge, G. Salamo and C. Lienau, "Coherent exciton-surface-plasmon-polariton interaction in hybrid metal-semiconductor nanostructures", Phys. Rev. Lett., 101, 116801 (2008).

Biography

Ma Luo was born in Guangzhou, Guangdong, China, on December 8th, 1982. Ma Luo received BS degree in Physics from Sun Yat-Sen University in 2005. Ma Luo received the John T. Chambers scholarship in 2011.

List of Publications:

1. M. Luo and Q. H. Liu, "Enhancement of second harmonic generation in a periodically patterned distributed Bragg reflector", in preparation to submission.

2. M. Luo, Y. Lin and Q. H. Liu, "Spectral methods and domain decomposition for nanophotonic applications", Proceedings of the IEEE, Vol. 101, 473-483 (2013).

3. M. Luo and Q. H. Liu, "Enhancement of second harmonic generation in an air-bridge photonic crystal slab: simulation by spectral element method", J. Opt. Soc. Am. B 28, 2879-2887 (2011).

4. M. Luo and Q. H. Liu, "Extraordinary transmission of a thick film with a periodic structure consisting of strongly dispersive materials", J. Opt. Soc. Am. B 28, 629-636 (2011).

5. M. Luo and Q. H. Liu, "Three-dimensional dispersive metallic photonic crystals with a bandgap and a high cutoff frequency", J. Opt. Soc. Am. A 27, 1878-1884 (2010).

6. M. Luo, Q. H. Liu, and J. Guo, "A spectral element method calculation of extraordinary light transmission through periodic subwavelength slits", J. Opt. Soc. Am. B 27, 560-566 (2010).

7. M. Luo and Q. H. Liu, "Spectral element method for band structures of three-dimensional anisotropic photonic crystals", Phys. Rev. E, 80, 056702 (2009).

8. M. Luo and Q. H. Liu, "Accurate determination of band structures of two-dimensional dispersive anisotropic photonic crystals by the spectral element method", J. Opt. Soc. Am. A 26, 1598-1605 (2009).

9. M. Luo, Q. H. Liu and Z. Li, "Spectral element method for band structures of two-dimensional anisotropic photonic crystals", Phys. Rev. E, 79, 026705 (2009).